

Preface

J. Karger-Kocsis¹, T. Czigány^{2}*

¹Institute for Composite Materials, University of Kaiserslautern, Erwin Schrödinger Str. 58, D-67663 Kaiserslautern, Germany

²Department of Polymer Engineering, Budapest University of Technology and Economics, Műgyetem rkp. 3., H-1111, Budapest, Hungary

Dear Readers,

You are reading the first issue of the second volume of *eXPRESS Polymer Letters*. In the first year more than 400 manuscripts have been submitted to the journal from which only 32% has been accepted for publication. It seems that launching this journal has been a good idea. Our goal to accelerate the publication of submitted articles generated a positive response among the authors. The average publication period from the submission until publishing was 96 days, from which the mean interval of the reviewing process took only 34 days.

This is the right place to express our thanks to all of our authors and reviewers for their contribution and hard work.

In the first year almost 100,000 visitors had a look at the homepage of *eXPRESS Polymer Letters* to collect some information about upcoming conferences, about related journals and their standing or to download articles. Among the articles the most popular ones became the 'Editorial corners', in which the Editors of the journal and the members of the International Advisory Board expressed their opinion on actual research trends, methods and techniques. Regarding the number of downloaded papers the most viewed articles dealt with nano- and biomaterials and with composites. We expect that the popularity of the journal increases further as the num-

ber of submitted manuscripts and the number of visitors grow from month to month. In this way, and with your steady support, we hope to reach our next target, i.e. *eXPRESS Polymer Letters* should receive an impact factor. By the way, the journal is always indexed among others by SCOPUS and Chemical Abstracts.

At present we are involved in the printing of the first volume. We would like to make the *eXPRESS Polymer Letters* available in printed form in the leading libraries of the world. You may read further information to this topic later in our homepage.

We wish you great success with your research work and we hope to welcome you soon among our authors and reviewers.

Sincerely yours,



Prof. Dr.-Ing. Dr.hc. József Karger-Kocsis
Editor-in-chief

Prof. Dr. Tibor Czigány
Editor

*Corresponding author, e-mail: czigany@eik.bme.hu
© BME-PT and GTE

Optimization of process variables on flexural properties of epoxy/organo-montmorillonite nanocomposite by response surface methodology

W. S. Chow*, Y. P. Yap

School of Materials and Mineral Resources Engineering, Engineering Campus, Universiti Sains Malaysia, Nibong Tebal 14300 Pulau Pinang, Malaysia

Received 17 August 2007; accepted in revised form 4 October 2007

Abstract. This study attempted to investigate the preparation and optimization of the flexural properties for epoxy/organo-montmorillonite (OMMT) nanocomposites. In-situ polymerization method was used to prepare epoxy/OMMT nanocomposites. The diglycidyl ether bisphenol A (DGEBA) and curing agent were mixed first, followed by the addition of OMMT. In this study, computer aided statistical methods of experimental design (Response Surface Methodology, RSM) was used to investigate the process variables on the flexural properties of epoxy/4wt% OMMT nanocomposites. Speed of mechanical stirrer, post-curing time and post-curing temperature were chosen as process variables in the experimental design. Results showed that the speed of mechanical stirrer, post-curing time and post-curing temperature were able to influence the flexural modulus and flexural yield stress of epoxy/4 wt% OMMT nanocomposites. The results of optimization showed that the design of experiment (DOE) has six combination of operating variables which have been obtained in order to attain the greatest overall desirability.

Keywords: *polymer composites, nanocomposites, materials testing, response surface methodology, design of experiment*

1. Introduction

Polymer nanocomposites have received considerable attention and great interest in industry and academia. Epoxy resin systems are increasingly used as matrices in composite materials for a widespread application such as automotive, aerospace, structural application, shipbuilding and electronic devices owing to their high strength, low viscosity, low shrinkage during curing, low creep and good adhesion to many substrates [1, 2]. Among the epoxy-inorganic nanocomposites, in particular, the use of layered silicate is due to the fact that clay has high aspect ratio, plate morphology, natural availability and low cost [3]. Modification of montmorillonite surface may reduce the physical or electrostatic bonding force of clay interlayer, which

leads to favor the formation of nanocomposites and to exfoliate the interlayer of the silicate layers. However, the organo-montmorillonite is relatively expensive. Montmorillonite is classified as magnesium aluminum silicate which has sheet morphology, and can be used to make a new class of polymer/clay nanocomposites [4].

In-situ polymerization has been explored to produce thermosets nanocomposites. This method has been extensively used for the production of both intercalated and exfoliated epoxy-based nanocomposites [5]. In this method, the modified layered silicate is swollen by a liquid monomer or a monomer solution. The monomer migrates into galleries of the layered silicate, so that the polymerization can occur within the intercalated sheets. The polymer-

*Corresponding author, e-mail: shyang@eng.usm.my
© BME-PT and GTE

ization reaction can be carried out by heat, radiation or a suitable initiator [6]. The formation and morphology of epoxy-clay nanocomposites is determined by a balance between the intragallery and the extragallery polymerization rate of monomer or prepolymer in the clay layers [7].

Strategy of experimentation is a general method to planning and conducting the experiment. Usually, experiments are performed to generate data from the process and then use the information from the experiment to establish new conjectures which lead to new experiments, and so on [8]. In engineering, experimentation plays an important role in new product design, manufacturing process development, and process improvement. The objective in many cases may be to develop a robust process, that is, a process affected minimally by external sources of variability [8].

Design of experiment (DOE) is a structured, organized method that is used to determine the relationship between the different factors (x_s) affecting a process and the output of the process (y) [9]. Design of experiments includes designing a set of ten or more experiments, in which all relevant factors are varied systematically. DOE uses the smallest possible number of experimental runs to discover and find the optimum settings for the process [9]. DOE provides a cost-effective means for solving problems and developing new processes. The simplest, but most powerful, DOE tool is two-level factorial design, where each input variable is varied at high (+) and low (–) levels and the output observed for resultant changes. Statistics can then help to determine which inputs have the greatest effect on outputs [10]. Another advantage of DOE is that it shows how interconnected factors respond over a wide range of values, without requiring the testing of all possible values directly. DOE fits response data to mathematical equations. Collectively, these equations serve as models to predict what will happen for any given combination of values. With these models, it is possible to optimize critical responses and find the best combination of values [11].

Response surface methodology (RSM) has been widely used in the empirical study of the relationship between one or more measured responses such as yield, on one hand, and a number of input variables such as time, temperature, pressure, and con-

centration on the other hand [12]. RSM is a collection of mathematical and statistical techniques that are useful for the modeling and analysis of problems in which a response of interest is influenced by several variables and the response surface can be explored to determine important characteristics such as optimum operating conditions. In our previous studies, it was found that 4wt% of OMMT could achieve a balance of flexural modulus, strength and strain. In this study, Response Surface Methodology was used to investigate the effects of processing variables on the flexural properties of epoxy/OMMT nanocomposites. The 3 factors include: (i) mechanical stirrer speed, (ii) post-curing time, and (iii) post-curing temperature. Suitable combination of optimization for flexural properties of epoxy/OMMT nanocomposites will be determined.

2. Materials and methods

2.1. Materials

The epoxy resin used as the polymer matrix was DER 331, a bisphenol A diglycidyl ether-based resin (DGEBA) supplied by Dow Chemical. This epoxy resin offered epoxide equivalent weight of 182–192, viscosity of 11 000–14 000 mPa·s, and density of 1.16 g/cm³ at 25°C. The cycloaliphatic amine is a phenol free version and was used as curing agent for the epoxy resin DGEBA system. The cycloaliphatic amine (HY 2964) was supplied by Ciba-Geigy. The viscosity of HY 2964 is 30–70 cP while the density of the resin is 8.3 lb/gal. The organo-montmorillonite (OMMT) (Nanomer 1.28E) is an organosilicate modified by quaternary trimethylstearyl ammonium ions having an approximate aspect ratio of 75–120, was purchased from Nanocor Co., USA.

2.2. Preparation and characterization of epoxy/OMMT nanocomposites

The DGEBA and curing agent were mixed first, followed by the addition of OMMT. The mixing of the DGEBA, curing agent and OMMT was performed using mechanical stirrer. Then, the mixture was poured into a square plastic mould with dimension 13 cm × 13 cm × 8 cm (length × width × height) and degassed using a vacuum oven. Fur-

ther, curing of epoxy/OMMT nanocomposites was carried out at room temperature for 1 hour and followed by post-curing. The flexural properties of the epoxy/OMMT nanocomposites were determined according to the ASTM D790 using an Instron 3366 machine. The dimension of the sample are 110 mm × 12.7 mm × 3mm (length × width × thickness). The span length was set at 50 mm and the testing speed was set at 5 mm/min. The flexural modulus and flexural yield stress were determined.

2.3. Experimental Design- Response Surface Methodology (RSM)

2.3.1. Study on the effects of processing variables

In this study, the effect of three independent variables in the nanocomposites system can be investigated by using rotatable central composite design (CCD), which is one of the designs in response surface methodology design. The three factors in the designs were considered. Factor x_1 is the mechanical stirrer speed, factor x_2 is the post-curing time

and factor x_3 is the post-curing temperature. The measured responses y is the flexural modulus and flexural yield stress of epoxy/OMMT nanocomposites. The experimental design matrix in coded variables employed in the present studies in nanocomposites systems were given in Table 1. The various processing combination are furnished in coded variables in accordance with the usual practice of statistical design of experiments. The relationship between the coded and real variables is given in Table 2. The results were analyzed by using Design Expert Version 6 software. Statistical analysis (regression and ANOVA analysis) of the responses are carried out to estimate the coefficients of the polynomial equation of the response by regression and to check the significance of the regression coefficients of independent variables and interaction variables by ANOVA. ANOVA is a method of testing for the equality of three or more population means by analyzing sample variances. Analysis of variance (ANOVA) table is used to determine the significance of the first degree, second degree, and cross-product terms of the polynomial. However, the ANOVA in this case confirms the adequacy of the quadratic model (the Model Probability $> F$ is less than 0.05).

Table 1. Design matrix for central composite design

Number of runs		X_1	X_2	X_3
1	Design center points	0	0	0
2		0	0	0
3		0	0	0
4		0	0	0
5		0	0	0
6		0	0	0
7	Axial or star point	1.68	0	0
8		0	0	-1.68
9		0	-1.68	0
10		-1.68	0	0
11		0	1.68	0
12		0	0	1.68
13	Fractional factorial design	1	-1	1
14		1	1	1
15		1	1	-1
16		-1	1	-1
17		-1	-1	1
18		-1	1	1
19		-1	-1	-1
20		1	-1	-1

Table 2. Relationship between coded and real values

	Coded levels/real levels				
	-1.68	-1	0	1	1.68
Mechanical stirrer speed [rpm]	528	800	1200	1600	1873
Post-curing time [min]	36	50	70	90	104
Post-curing temperature [°C]	93	100	110	120	127

3. Results and discussion

3.1. Statistically designed experiments

The experiment in the present study was conducted to determine the effect of process variables on the flexural properties of epoxy/OMMT nanocomposites. Approximately operating conditions for preparation of epoxy nanocomposites were required to be established for achieving the following objectives:

1. To minimize the curing time of epoxy nanocomposites.
2. To minimize the curing temperature used in the production of epoxy nanocomposites samples in order to maximize the final properties of the epoxy nanocomposites.

3. To determine the optimum processing condition of epoxy nanocomposites.

The achievements of the above objectives are subjected to the constraints and these constraints are necessary to impose during the optimization stage. Before attempting such optimization with constraint, basic functional relationship between the process variables and the following responses are to be clearly established:

1. Flexural yield stress of epoxy nanocomposites
2. Flexural modulus of epoxy nanocomposites

Since the efficacy of the process depends on the operating variables, the desired optimization cannot be accomplished by classical ‘one variable at a time’ approach, Response Surface Methodology (RSM) was adopted to determine the functional relationships between the process variables and ultimate performance characteristics of epoxy nanocomposites. In the case of the epoxy nanocomposites process, non-linear trends in the response are likely and hence a second order polynomial

model could be considered to fit adequately the experimental results. Efficient classes of experimental designs known as Central Composite Design (CCD) are used to generate data that will be well suited for fitting a quadratic surface, which usually works well for process optimization. The basic central composite design consists of a 2^k factorial design for k variables at two level (-1, +1) superimposed on a star design with $2k$ axial points and several replication at the central values.

Table 3 shows the experimental data for the effects of process variables on the flexural properties of epoxy/4 wt% OMMT nanocomposites, i. e. flexural modulus and flexural yield stress. Process variables studies included speed of mechanical stirrer (X_1), post curing time (X_2) and post curing temperature (X_3). Coded values and real values for each combination of process variables were given in Table 4. The relation between the effects of process variables on flexural properties of epoxy/OMMT nanocomposites are discussed in this section.

Table 3. Effects of process variables on the flexural properties of epoxy/4 wt% OMMT nanocomposites

Std	Combination of process variables						a	b
	Coded value			Real value				
	X_1	X_2	X_3	X_1	X_2	X_3		
1	-1	-1	-1	800	50	100	76	2853
2	1	-1	-1	1600	50	100	70	2795
3	-1	1	-1	800	90	100	79	2994
4	1	1	-1	1600	90	100	67	2581
5	-1	-1	1	800	50	120	75	2900
6	1	-1	1	1600	50	120	71	2803
7	-1	1	1	800	90	120	80	3148
8	1	1	1	1600	90	120	77	2937
9	-1.68	0	0	528	70	110	78	2925
10	1.68	0	0	1873	70	110	73	2987
11	0	-1.68	0	1200	36	110	71	2914
12	0	1.68	0	1200	104	100	79	3259
13	0	0	-1.68	1200	70	93	71	2652
14	0	0	1.68	1200	70	127	88	3417
15	0	0	0	1200	70	110	77	2873
16	0	0	0	1200	70	110	77	2854
17	0	0	0	1200	70	110	76	2928
18	0	0	0	1200	70	110	76	2873
19	0	0	0	1200	70	110	79	2723
20	0	0	0	1200	70	110	78	2843

X_1 : Speed of mechanical stirrer [rpm]; X_2 : Post curing time [minutes]; X_3 : Post curing temperature [°C];
 a: Response flexural yield stress [MPa]; b: Response flexural modulus [MPa]

Table 4. The coded and real values of the 3 factorial levels in preparation process of epoxy/OMMT nanocomposites

Name	Symbol	Unit	Low actual	High actual	Low coded	High coded
Speed of mechanical stirrer	X_1	rpm	528	1873	-1.68	1.68
Post curing time	X_2	min	36	104	-1.68	1.68
Post curing temperature	X_3	°C	93	127	-1.68	1.68

Finally optimization of the overall process was considered taking into consideration of time and performance. The economic feasibility of the process depends on the time and temperature reduction of the epoxy/OMMT preparation process and desired mechanical properties of the end product. The optimization has to be performed by a well developed statistical method known as ‘optimization with constraints’. This is a technique employed to a system wherein there are multiple responses. In this system, since it is not possible to maximize every response simultaneously, a compromise or ‘trade-off’ of some properties becomes necessary. Optimization with constraints is the technique employed for this purpose.

3.2. Flexural properties

3.2.1. Effects of process variables on flexural yield stress

In this section, effects of process variables on the flexural yield stress of the epoxy/4 wt% OMMT nanocomposites are discussed. The flexural yield stress values were measured and are given in Table 3. These results were analyzed by employing Design Expert Version 6 Software (Star-Ease Corporation, 2003) to establish the mathematical functional relations as well as a number of statistics to confirm the variables of the models. The experimental data in Table 3 was analyzed. A linear model was found to fit adequately the experimental data. The adequacy of the model was established by ANOVA, Normal Probability plot and Residual Analysis. Through the estimation of all regression coefficients, the experimental response could be modeled as a polynomial equation that shows the effect of experimental factors on the yield stress. The linear function obtained is given in Equation (1):

$$\text{Flexural yield stress} = +75.88 - 2.40 \cdot X_1 + 1.78 \cdot X_2 + 2.88 \cdot X_3 \quad (1)$$

With the probability value $p < 0.0001$, significant lack of fit ($p = 0.0035$) and reasonable correlation coefficient ($R^2 = 0.6068$).

The response function could be represented graphically by perturbation plots and three dimensional (3D) plots. Perturbation graph shows the effect of

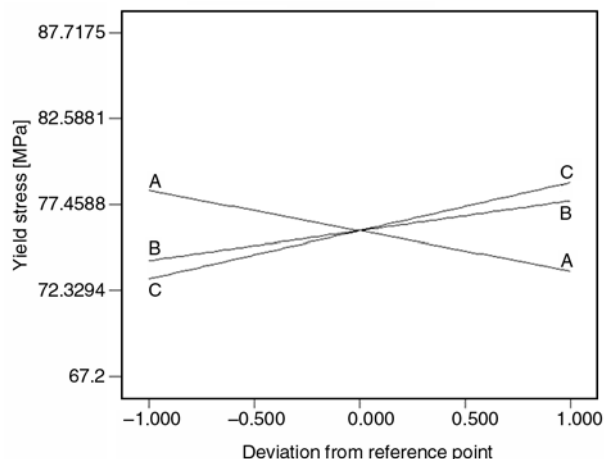


Figure 1. Flexural yield stress of epoxy/4 wt% OMMT nanocomposites as a response of 3 factors in perturbation plots. A – speed of mechanical stirrer; B – post curing time; C – post curing temperature

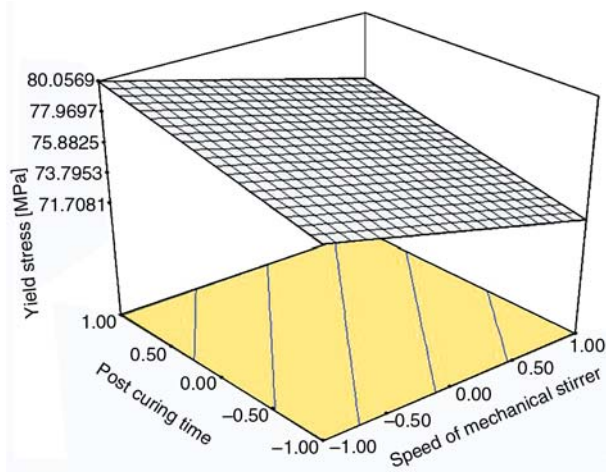


Figure 2. 3D response surface plot of the flexural yield stress as a function of speed of mechanical stirrer and post curing time in coded values

changing one factor while holding the rest as constant. This plot can be useful when trying to decide which axes to use on a contour or 3D plot. Perturbation plot in Figure 1 shows the effect of speed of mechanical stirrer, post curing time and post curing temperature variables on the flexural yield stress of the epoxy/4 wt% OMMT nanocomposites. Flexural yield stress of the epoxy/4 wt% OMMT nanocomposites show an increase as the level of post curing time and post curing temperature increased. A slightly reduction in flexural yield stress is observed as the speed of mechanical stirrer increased. Figure 2 shows the 3D response surface plot of the flexural yield stress as a function of speed of the mechanical stirrer and post curing time in coded

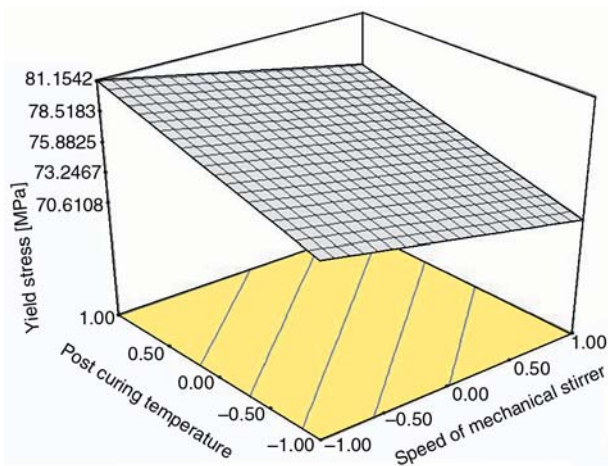


Figure 3. 3D response surface plot of the flexural yield stress as a function of speed of mechanical stirrer and post curing temperature in coded values

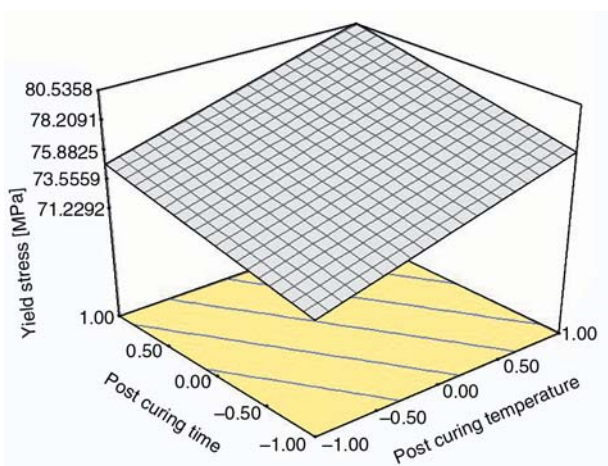


Figure 4. 3D response surface plot of the flexural yield stress as a function of post curing temperature and post curing time in coded values

values. Figure 3 shows that 3D response surface plot of the flexural yield stress as a function of speed of the mechanical stirrer and post curing temperature in coded values. 3D response surface plot of the flexural yield stress as a function of post curing temperature and post curing time in coded values was shown in Figure 4.

Note that all three-dimensional plots show the same trend. From Figure 2, it can be seen that at low level of post curing time, as speed of mechanical stirrer increases, the flexural yield stress decreased. However, at high level of post curing time, the flexural yield stress increased as speed of mechanical stirrer decreased. Table 3 shows that as the level of post curing time increases from 36 to 104 minutes, the flexural yield stress increases

from 71 to 79 MPa. This indicates that the longer the post-curing time, the higher the degree of crosslinking. Similar to what happened in the case of the effect of post curing time towards the flexural yield stress. The effect of post curing temperature showed similar trend as displayed in Figure 3 and Figure 4.

Flexural yield stress of epoxy/OMMT nanocomposites increased as the post curing temperature increase due to the establishment of higher degree of crosslinking. According to Camino *et al.* [13], curing conditions are of paramount importance to the final properties of the epoxy/OMMT nanocomposites. It is important to select a curing condition that could achieve a balance between intragallery and extragallery polymerization rates which allow better clay exfoliation. If the curing time and curing temperature is too low and the rates of epoxy and crosslinker intercalation are slow, then extragallery polymerization is faster than the intragallery polymerization and hence the poor interaction between filler and matrix could result. On the other hand, the higher curing temperature and higher curing time will promote a higher degree of crosslinking. Tolle and Anderson [14] have reported that the curing of thermosetting resins involves the interaction and chemical kinetics; therefore the physical and mechanical properties will be changed.

Figures 2 and 3 show that the flexural yield stress decreased as the speed of mechanical stirrer increased. The two of three-dimensional plots shows the same trends. From Table 3, it is shown that the flexural yield stress decreases from 78 to 73 MPa when the speed of mechanical stirrer increases from 528 to 1873 rpm. This may due to the bubbles that were easily created and trapped inside the sluggish mixture when the speed of mechanical stirrer is relatively high. If the speed of mechanical stirrer too high, the mixing process introduces air into the formulation and the microvoid may exist in the epoxy/OMMT nanocomposites samples. According to Akbari and Begheri [15], the reduction of flexural yield stress was attributed to the formation of micro-void in the nanocomposites system. It was claimed that microvoids act as stress concentrators and facilitate shear yielding in the nanocomposites system and therefore reduce the flexural yield stress.

3.2.2. Effects of process variables on flexural modulus

The values of flexural modulus of epoxy/OMMT nanocomposites prepared in this study are given in Table 3. All the experimental data were collected and analyzed. The results of the CCD experiments on the effect of the process variables in flexural modulus are tabulated in Table 3 and presented in Figures 5–8.

The experimental data in Table 3 were analyzed. From these results, suitable model was selected. The adequacy of the model was established by ANOVA, Normal Probability plot and Residual Analysis. Through the estimation of all regression coefficients, the experimental response can be modeled as a polynomial equation that shows the effect of process variables on the flexural modulus of epoxy/OMMT nanocomposites. The linear function obtained is given in Equation (2):

$$\text{Flexural modulus} = +2912.91 - 49.33 \cdot X_1 - 65.13 \cdot X_2 + 135.47 \cdot X_3 \quad (2)$$

With the probability value $p > 0.0112$, significant lack of fit ($p = 0.0258$) and reasonable correlation coefficient ($R = 0.4902$).

The response function could be represented graphically by perturbation plots and three dimensional plots (3D). The perturbation plot in Figure 5 shows that the post-curing time and post curing temperature were responsible to increase the flexural modulus during the preparation process. However, the

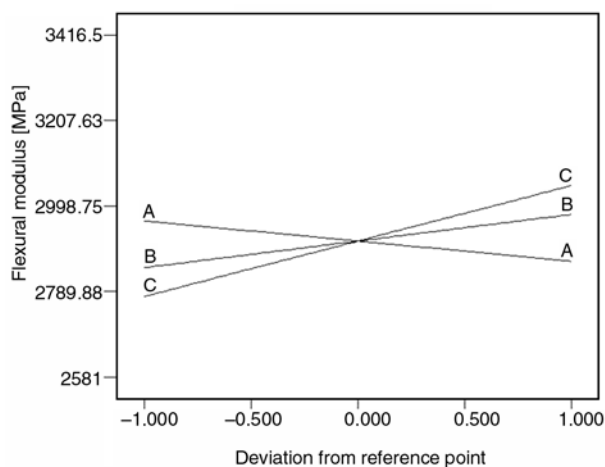


Figure 5. Flexural modulus of epoxy/OMMT nanocomposites as a response of 3 factors in perturbation plots. A – speed of mechanical stirrer; B – post curing time; C – post curing temperature

speed of mechanical stirrer was responsible to decrease the flexural modulus as the speed of mechanical stirrer increased. From Table 3, the highest flexural modulus 3259 MPa can be obtained by employing combination of speed of mechanical stirrer with 1200 rpm, post-curing time 100 minutes and post-curing temperature 100°C for the preparation of epoxy/OMMT nanocomposites. When Figure 1 and 5 are compared, it can be seen that the same trend can be observed. This indicates that an increasing of post curing time and post curing temperature resulted in increasing flexural modulus. However, increasing the speed of mechanical stirrer will decrease the flexural modulus.

The effects of post curing time and speed of mechanical stirrer on flexural modulus of epoxy/

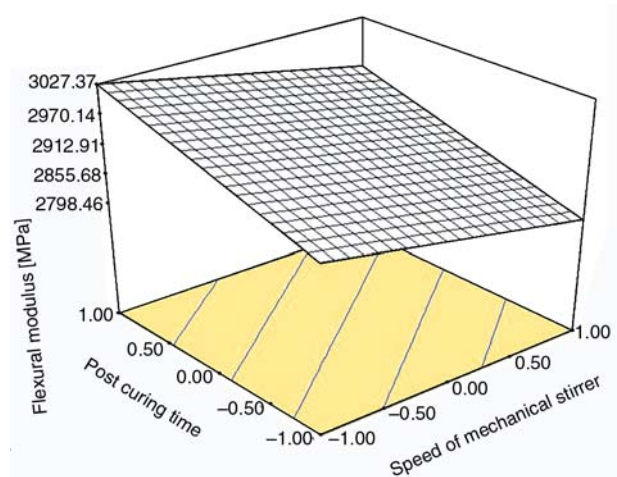


Figure 6. 3D response surface plot of flexural modulus as a function of speed of mechanical stirrer and post curing time in coded values

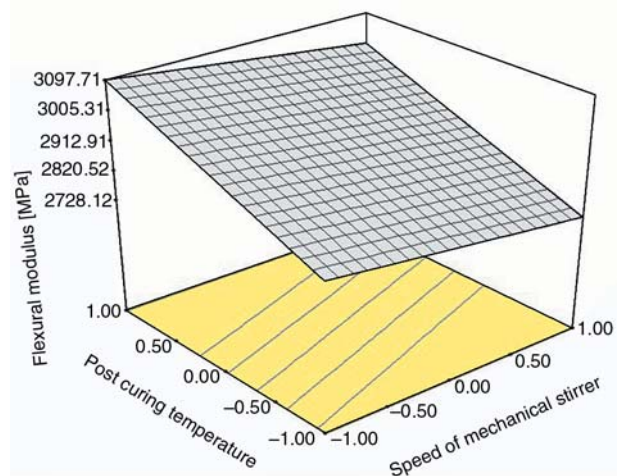


Figure 7. 3D response surface plot of flexural modulus as a function of speed of mechanical stirrer and post curing temperature in coded values

OMMT nanocomposites is shown as 3D curve in Figure 6. Figure 7 shows the 3D response surface plot of flexural modulus as a function of speed of mechanical stirrer and post curing temperature in coded values. It is obvious that the flexural modulus decreased as the speed of mechanical stirrer increased. This may be due to the very high inertial forces in the speed of mechanical stirrer and caused the clay layers to break rather than separate. Once established the inertial forces will cause the heavier sediments to sink to the bottom while keeping the lighter particles at the top. The aim is to use this force to break up the clumps of clay in a polymer solution and separate some of the clay layers as well [16]. According to Saber-Samandari *et al.* [16] the decrease in the modulus comes from the fact that at high speeds, the large inertial force no longer acts to separate clay layers but also break some of the layers as well making them no longer effective as a good reinforcing filler to improve the polymer properties.

It was observed from the 3D plot in Figure 8 that the flexural modulus increased as the post-curing time and post curing temperature increased. This is again attributed to the higher degree of crosslinking formation as the post-curing time and the post-curing temperature increased as explained earlier. According to Dean *et al.* [17], at a higher temperature, the combination of a lower prepolymer viscosity and faster intergallery curing are sufficient to yield more significant expansion of the layers. Therefore, the flexural modulus increased as the post curing time and post curing temperature

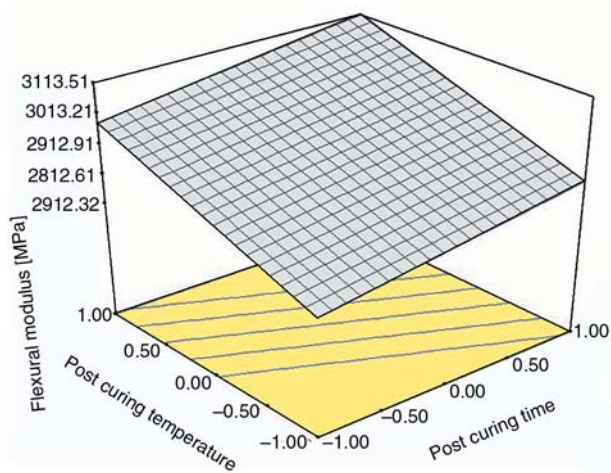


Figure 8. 3D response surface plot of flexural modulus as a function of post curing time and post curing temperature in coded values

increased. Kornmann *et al.* [18] have reported that the highest curing temperature increases the reactivity of the epoxy systems, it also increases the diffusion rate of the epoxy and the curing agent between the layers, favoring the intragallery cure kinetics. This leads to exfoliation of the clay. Due to the reinforcing effects of the clay, strong interaction between the polymer and clay leads to a layer of polymer that is directly adsorbed and bound to the particles. Therefore, it could subsequently improve the flexural modulus. However, if the post curing time is too low and the crosslinker may not have enough time to diffuse into clay galleries, weak interaction between the polymer and clay could result. Consequently, the improvement of flexural modulus may not be achieved.

3.3. Optimization

In a multiple response system, since it is not possible to maximize all the response simultaneously, a compromise or ‘trade off’ of some of the properties is required to be adopted. This type of ‘optimization with constraint’ was adopted in this research. The Design Expert Software has the capability to analyze the results in order to achieve this objective. Numerical optimization was used to optimize any combination of one or more goals. The goals may be apply either factors or responses. In the optimization parameters, the program uses five possibilities for a goal to construct desirability indices, i. e. maximize, minimize, target, within range, none (for responses only). A weight was assigned to the goal to adjust the shape of its particular desirability function. The default value of one creates a linear ramp function between the low value and the goal or the high value and the goal.

Table 5. Criteria for epoxy/4 wt% OMMT nanocomposites system’s responses

Responses	Minimum value	Maximum value
Flexural yield stress	67.2 MPa	87.7 MPa
Flexural modulus	2581 MPa	3416 MPa

Table 6. Constraints applied for optimization

Name	Goal
Speed of mechanical stirrer [rpm]	is the range
Post curing time [minutes]	is the range
Post curing temperature [°C]	is the range
Flexural yield stress [MPa]	in maximum
Flexural modulus [MPa]	in maximum

Table 7. Suitable combination of optimization on flexural properties of epoxy/4 wt% OMMT nanocomposites

Number	Speed of mechanical stirrer	Post curing time	Post curing temperature	Flexural yield stress	Flexural modulus	Desirability
1	800.00	90.00	119.99	82.93	3162.73	0.731
2	804.34	90.00	120.00	82.91	3162.30	0.730
3	812.08	89.98	120.00	82.86	3161.29	0.728
4	800.01	90.00	119.64	82.83	3157.94	0.725
5	800.00	90.00	118.54	82.51	3143.02	0.709
6	800.00	90.00	117.40	82.19	3127.62	0.691

Determinations of final product's criteria are the first step in the optimization process. Determinations of criteria depend on mechanical properties of end product required from the research. Numerical method and graphical method in Design Expert can be used in optimization process. All the criteria for every desirable response are listed in Table 5. Design Expert has been used to determine the combination of variables that give the optimum response based on the desirable criteria. The constraints in this study were chosen as to minimize all the process variables to achieve overall economy of the process. The goals were set to maximize, minimize, target, within range or none as shown in Table 6.

By using Design Expert software in optimization process, all solutions or combinations of optimum responses for process variables of epoxy/4 wt% OMMT nanocomposites is shown in Table 7. Table 7 shows all the predicted values for each of the response and operating variables combinations. First combination was chosen because it has the highest desirability. Desirabilities range from zero to one for any given response. The program combines the individual desirabilities into a single number and then searches for the greatest overall desirability. A value of one represents the ideal case while a zero indicates that one or more response fall outside desirable limits. In the future work, investigation will be performed on this combination of optimization process parameter for the epoxy/OMMT nanocomposites.

4. Conclusions

Statistically designed experiments were conducted and the parameters which influence the flexural properties were established. In term of flexural yield stress, results shows that as the level of post curing time increase from 36 to 104 minutes, the

yield stress was increased from 71 to 79 MPa. This indicates that the longer the post-curing time, the degree of crosslinking will be higher. Besides, flexural yield stress of epoxy/OMMT nanocomposites increased as the effect of post curing temperature increase due to the formation of higher degree of crosslinking. However, the flexural yield stress decrease from 78 to 73 MPa when the speed of mechanical stirrer increase from 528 to 1873 rpm. In term of flexural modulus, the process variables; i. e., post-curing time and post curing temperature were responsible to increase the flexural modulus. However, the speed of mechanical stirrer was responsible to decrease the flexural modulus as the speed of mechanical stirrer increase. Optimization processes have been carried out to determine the suitable combinations of operating variables in order to attain desirable flexural properties.

Acknowledgements

W. S. Chow would like to thank Universiti Sains Malaysia and Ministry of Higher Education Malaysia for the research grant support and Fundamental Research Grant Scheme (FRGS).

References

- [1] Tarleja R., Manson J. E.: *Comprehensive composite materials*, Vol 2: Polymer matrix composites. Elsevier Science, Oxford (2000).
- [2] Isik I., Yilmazer U., Bayram G.: Impact modified epoxy/montmorillonite nanocomposites: Synthesis and characterization. *Polymer*, **44**, 6371–6377 (2003).
- [3] Gu A., Liang G.: Thermal degradation behaviour and kinetic analysis of epoxy/montmorillonite nanocomposites. *Polymer Degradation and Stability*, **80**, 383–391 (2003).
- [4] Ho M-W., Lam C-K., Lau K-T., Ng D. H. L., Hui D.: Mechanical properties of epoxy-based composites using nanoclays. *Composite Structure*, **75**, 415–421 (2006).

- [5] Koo J. H.: Polymer nanocomposites: Processing, characterization, and applications. McGraw-Hill, Columbus (2006).
- [6] Beyer G.: Nanaocomposites: a new class of flame retardants for polymer. *Plastic, Additives and Compounding*, **4**, 22–28 (2002).
- [7] Chen D., He P.: Monitoring the curing process of epoxy resin nanocomposites based on organo-montmorillonite- a new application of resin curemeter. *Composites Science and Technology*, **64**, 2501–2507 (2004).
- [8] Montgomery D. C.: Response surface methodology. in 'Design and analysis of experiments' (eds.: Montgomery D. C.) John Wiley and Sons, New York (2001).
- [9] Yang K., El-Haik B. S.: Design for six sigma: A roadmap for product development. McGraw-Hill, New York (2003).
- [10] Anderson M. J., Kraber S. L.: Eight keys to successful DOE. *Quality Digest Magazine*, <http://www.qualitydigest.com/july99/html/dae.html> (1999).
- [11] Anderson M.: Design of Experiments. *The Industrial Physicist*, **3**, 24–26 (1997).
- [12] Kumar R. N., Woo C. K., Abu Bakar A.: UV radiation curing of surface coatings based on enr cycloaliphatic diepoxide-glycidyl methacrylate system by cationic photoinitiators -Optimization of process variables through response surface methodology. *Journal of Coating Technology*, **71**, 79–88 (1999).
- [13] Camino G., Tartaglione G., Frache A., Manfredi C., Costa G.: Thermal and combustion behaviour of layered silicate-epoxy nanocomposites. *Polymer Degradation and Stability*, **90**, 354–362 (2005).
- [14] Tolle T. B., Anderson D. P.: Morphology development in layered silicate thermoset nanocomposites. *Composites Science and Technology*, **62**, 1033–1041 (2002).
- [15] Akbari B., Bagheri R.: Deformation mechanism of epoxy/clay nanocomposites. *European Polymer Journal*, **43**, 782–788 (2007).
- [16] Saber-Samandari S., Khatibi A. A., Basic D.: An experimental study on clay/epoxy nanocomposites produced in a centrifuge. *Composites, Part B: Engineering*, **38**, 102–107 (2007).
- [17] Dean D., Walker R., Theodore M., Hampton E., Nyairo E.: Chemorheology and properties of epoxy/layered silicate nanocomposites. *Polymer*, **46**, 3014–3021 (2005).
- [18] Kornmann X., Lindberg H., Berglund L. A.: Synthesis of epoxy-clay nanocomposites influence of the nature of the curing agent and structure. *Polymer*, **42**, 4493–4499 (2001).

Grafting of acrylonitrile onto cellulosic material derived from bamboo (*Dendrocalamus strictus*)

R. Khullar¹, V. K. Varshney^{1*}, S. Naithani², P. L. Soni¹

¹Centre for Advanced Studies in Chemistry of Forest Products, Forest Research Institute, P.O. New Forest, Dehra Dun 248 006, India

²Cellulose and Paper Division, Forest Research Institute, P.O. New Forest, Dehra Dun 248 006, India

Received 3 April 2007; accepted in revised form 21 October 2007

Abstract. Bamboo, a lignocellulosic biopolymer material, is of interest as feedstock for production of cellulose derivatives by chemical functionalization. Optimization of grafting of acrylonitrile onto cellulosic material (average Degree of Polymerization 816), isolated from bamboo (*Dendrocalamus strictus*) was performed by varying the process parameters such as duration of soaking of cellulosic material in ceric ammonium nitrate solution, ceric ammonium nitrate concentration, polymerization time, temperature of reaction and acrylonitrile concentration to study their influence on percent grafting and grafting efficiency.

Graft copolymerization of acrylonitrile onto cellulosic material derived from bamboo (*Dendrocalamus strictus*) in heterogeneous medium can be initiated effectively with ceric ammonium nitrate. The optimum reaction conditions obtained for grafting of acrylonitrile onto cellulosic material were: duration of dipping cellulosic material in ceric ammonium nitrate solution 1 hr, ceric ammonium nitrate concentration 0.02 M, acrylonitrile concentration 24.6 mol/anhydroglucose unit, temperature of reaction 40°C and polymerization time 4 hrs. The percent grafting for optimized samples is 210.3% and grafting efficiency is 97%. The characterization of the grafted products by means of FTIR and Scanning Electron Microscopy furnished the evidence of grafting of acrylonitrile onto the cellulosic material.

Keywords: biopolymers, cellulosic material, bamboo, grafting, acrylonitrile

1. Introduction

Biopolymers, being renewable raw materials, are gaining considerable importance because of the limited existing quantities of fossil supplies and the recent environment-conservative regulations [1]. In this regard, cellulose rich biomass acquires enormous significance as chemical feedstock, since it consists of cellulose, hemicellulose and lignin, which are biopolymers containing many functional groups suitable to chemical derivatization [2]. *Eucalyptus* cellulose and *Musanga cecropioides* wood have been modified into carboxymethyl cellulose (CMC) by Spasojevic *et al.* [3] and Akaranta *et al.* [4], respectively. Graft copolymerization of

acrylonitrile and methyl methacrylate onto jute fibers and pineapple leaf fibers has been examined [5–8]. Low quality woods as well as industrial wastes of wood have been utilized to produce a thermoplastic material through cyanoethylation [9]. Recently conducted investigations on reactivity of fibers of *Agave lechuguilla* and *Agave fourcroydes* under chemical modification reactions like carboxymethylation, sulfation, acetylation, tritylation and subsequent carboxymethylation as well as oxidation, and grafting have demonstrated suitability of the agave fibers as a potential feed stock for producing cellulose derivatives for a variety of applications [10–12]. The goal of these modifications is

*Corresponding author, e-mail: varshney2000@yahoo.com
© BME-PT and GTE

to adjust the properties of biopolymer macromolecule for different purposes and to increase their consumption.

Bamboo belonging to the grass family Poaceae is an abundant renewable natural resource capable of production of maximum biomass per unit area and time as compared to counterpart timber species [13]. Since bamboo stem consists almost entirely of cellulose, hemicellulose (xylans, arabans, polyuronides etc.) and lignin [14], the biomass of bamboo can be used as a feedstock for production of a variety of cellulose derivatives for different broader applications by chemical modification.

Graft copolymerization of cellulose is a process in which attempts have been made to combine synthetic polymers with cellulose, to produce material with the best properties of both. This process is known as grafting, usually done by modifying the cellulose molecules through creation of branches of synthetic monomers that confer certain desirable properties on the cellulose without destroying its intrinsic properties [15].

Depending on the chemical structure of the monomer grafted onto cellulose, graft copolymers gain new properties such as hydrophilic and hydrophobic character, improved elasticity, water absorption, ion-exchange capability and heat resistance. These copolymers are finding applications for water treatment for textile industry, for reclaiming ions of precious metals, and for personal care products such as diapers etc. [16].

As a part of our ongoing programme on chemical modification of cellulose isolated from different sources [17–20], we were interested to study the derivatization of bamboo cellulose through substitution and grafting reactions. The present communication describes the optimization of the reaction conditions for grafting of acrylonitrile onto cellulosic material obtained from bamboo (*Dendrocalamus strictus*) using two-phase system by varying the reaction parameters such as the duration of soaking cellulosic material in CAN (ceric ammonium nitrate), concentration of CAN, polymerization time, temperature and concentration of acrylonitrile and studying their effects on %G (percent grafting) and %GE (percent grafting efficiency). Each of these parameters was varied one by one keeping other conditions constant in the reaction.

2. Materials and methods

2.1. Materials

Dendrocalamus strictus, a widely distributed and commonly cultivated bamboo in India was used for isolation of cellulose. Cellulose (yield 35%) with following composition was isolated as per the standard Tappi method (TAPPI T2003 OM-88):

Cellulose 90.1; Hemicellulose 8.9; Lignin 0.4; Ash 0.6%; Average Degree of Polymerization (DP) 816. Ceric ammonium nitrate (Aldrich Chemical Co., U.S.A.), nitric acid (AR grade, Rankem, India), toluene (LR grade, Rankem, India) and dimethyl formamide (AR grade, Rankem, India) were used without any purification. Acrylonitrile (LR grade, Rankem, India) was purified before use by extracting with 7% aqueous sodium hydroxide solution. The liquid monomer was then washed with distilled water several times, dried over anhydrous calcium chloride and distilled.

2.2. Graft copolymerization

The grafting reaction was carried out under nitrogen atmosphere in a three-necked flask equipped with a nitrogen inlet and a reflux condenser immersed in a constant temperature water bath (Remi, India $\pm 1^\circ\text{C}$). Solution of CAN of varied concentrations were prepared by dissolving the required molar concentration of CAN salt in 1% nitric acid. In a typical reaction, 1 g cellulose was immersed in 30 ml solution of CAN (0.01–0.02 M) for a particular time (0.5–2 hrs) followed by addition of a mixture of toluene (20 ml) and acrylonitrile (12.3–30.7 mol/AGU). The reaction mixture was stirred using a magnetic stirrer. A continuous supply of nitrogen was maintained throughout the reaction period. The grafting reaction was carried out for varying periods of time (2–5 hrs) at varied temperatures (20–50°C) under stirring using a magnetic stirrer. After the reaction was over, the reaction mixture was washed with distilled water, subsequently with methanol, filtered and the product was dried in the vacuum oven at 50°C for 4 days. The dried product was extracted with dimethylformamide for 48 hrs to remove the homopolymer (polyacrylonitrile). The grafted cellulose was dried for 4 days to obtain a constant weight. The percent graft yield (%G) and percent grafting efficiency (%GE) were calculated on an oven dry weight of cellulose from the increased weight of cellulose after grafting by using the Equations (1) and (2) [15]:

$$\%G = \frac{\text{Final cellulose weight} - \text{Initial cellulose weight}}{\text{Initial cellulose weight}} \cdot 100 \quad (1)$$

$$\%GE = \frac{\text{Final cellulose weight} - \text{Initial cellulose weight}}{\text{Total polymer weight after reaction} - \text{Initial cellulose weight}} \cdot 100 \quad (2)$$

2.3. IR analysis

IR spectra of ungrafted and grafted cellulose were recorded on a JASCO FTIR-5300 spectrophotometer following the KBr disc technique in the range 4000–650 cm^{-1} .

2.4. Scanning Electron Microscopy (SEM) studies

SEM images at 1000 and 5000 magnification were obtained for parent and grafted cellulosic material using Leo 435 VP scanning electron microscope (Cambridge, England). The fibers were laid down on the aluminium stub using a conductive tape and were sputter coated with gold.

2.5. Water sorbency

The water sorbency of the parent and grafted cellulosic material was determined according to the method described by Das *et al.* [21]. The water sorbency was expressed as the water-retention value (WRV) in grams of water per gram of the oven dry sample weight and was calculated as Equation (3):

$$\text{WRV [g/g]} = (\text{WET} - \text{DRY})/\text{DRY} \quad (3)$$

where WET = Weight of sample after immersing in water for 24 hrs, DRY = Dry weight of the sample.

3. Results and discussion

3.1. Practical viewpoints

Prompted by findings of the advantageous use of non-aqueous medium (toluene) on the grafting of acrylonitrile onto cotton cellulose [22, 23], a two-phase system (aqueous initiator-toluene mixture) was used in this work also, which afforded high graft yields. Use of toluene inhibits diffusion of CAN out of the fiber, thus lessening homopolymer formation in the solution, and increases the availability of acrylonitrile, as reported by Gangnuex *et al.* [22] and Hon [23].

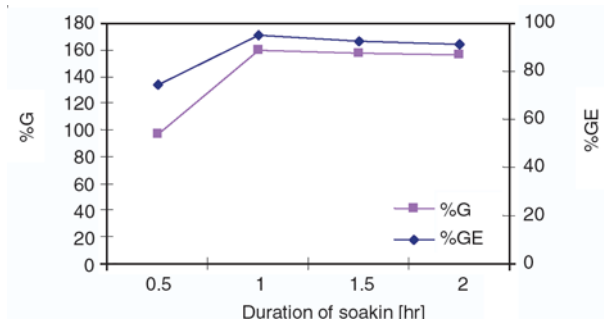


Figure 1. Effect of duration of soaking cellulosic material in CAN solution on %G and %GE

3.2. Effect of duration of soaking cellulosic material in CAN solution

The effect of soaking time on %G and %GE is shown in Figure 1. It can be seen that the %G and %GE increase rapidly with increase in time up to 1 hr after which it levels off. Soaking time allows ceric solution to diffuse into cellulose fibers prior to grafting reaction thereby allowing initiation of free radicals on cellulose sample by oxidation with Ce^{IV} ions. Initial increase in %G and %GE can be attributed to this factor [23]. Leveling off of %G and %GE on prolonging this soaking time beyond 1 hr could be attributed to the decay of free radical activity of Ce^{IV} oxidized cellulose resulting from the free radical termination by charge transfer. Similar trend has been observed by Hon [23] and Kulkarni and Mehta [24].

3.3. Effect of ceric ammonium nitrate concentration

Using standardized 1 hr soaking time of cellulosic material in CAN solution, the effect of variation in CAN concentration was studied and the results are shown in Figure 2. CAN concentration was increased from 0.01–0.02 M. It is evident that both the grafting parameters, %G and %GE increase with an increase in the initiator concentration, but reaches maximum value of 159.7 and 95.1%, respectively, at 0.02 M of CAN. These increasing trends of the grafting parameters indicated that

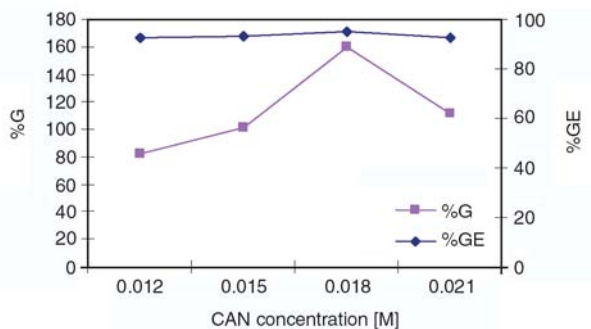


Figure 2. Effect of CAN concentration on %G and %GE

ceric ions exclusively participate in the formation of active sites on the cellulose up to this concentration of ceric ions, and beyond it, no more active sites are formed on the cellulose. Further increase in CAN concentration is accompanied by a decrease in the %G and %GE. The decreasing trend in %G and %GE beyond 0.02 M concentration of ceric ions may be assumed to be due to its participation in the termination reactions with growing homopolymer and propagating chains on the cellulose [25, 26].

3.4. Effect of monomer concentration

Using 1hr soaking time of cellulosic material in CAN solution and 0.02 M CAN concentration as optimized above, the effect of variation of monomer concentration was studied and the results are shown in Figure 3. The results show that as the monomer concentration increases from 12.3 to 30.7 mol/AGU, there is an increase in %G, reaching a maximum value of 168.3% at 24.6 mol/AGU and shows decreasing trend with further increase in monomer concentration. Similarly, at acrylonitrile concentration of 24.6 mol/AGU, %GE reaches a maximum value of 95.8%. Thereafter, there is a decrease in %GE with increase in acrylonitrile concentration.

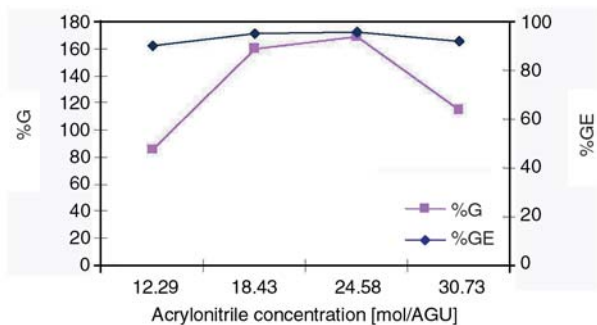


Figure 3. Effect of acrylonitrile concentration on %G and %GE

The enhancement of %G and %GE by increasing monomer concentration to optimum value could be ascribed to the greater availability of monomer to grafting sites. However, the decreasing trend of %G and %GE beyond optimum monomer concentration may be due to the competition between homopolymerization and graft copolymerization, where the former prevails over the latter at higher acrylonitrile concentration [26–28].

3.5. Effect of temperature

The grafting reactions were carried out at different temperatures (20–50°C) keeping the other variables constant. The effect of temperature on %G and %GE is shown in Figure 4. Results show that maximum %G (174.8%) is obtained at 40°C and decreases with further increase in temperature. The dependence of %G on temperature can be ascribed

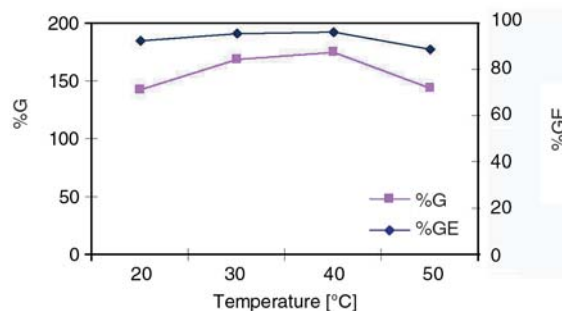


Figure 4. Effect of temperature on %G and %GE

to higher rate of dissociation of initiator as well as the diffusion and mobility of monomer from the aqueous phase to cellulose phase, resulting in considerable improvement in the grafting yield [26, 29]. The %GE reaches a maximum value of 96.3% at 40°C. With further increase of temperature beyond 40°C, the radical termination reaction might be accelerated, leading to decrease of %G as well as %GE. These findings are in agreement to those reported in literature [23, 26, 29].

3.6. Effect of duration of polymerization

Using standardized 1 hr soaking time of cellulosic material in CAN solution of concentration of 0.02 M, acrylonitrile concentration 24.6 mol/AGU and polymerization temperature 40°C, the effect of polymerization time on %G and %GE was studied

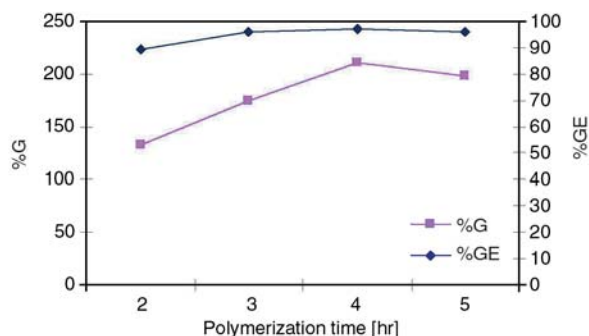


Figure 5. Effect of duration of polymerization on %G and %GE

and the results are shown in Figure 5. It can be seen from the figure that the %G increases rapidly with increase in time up to 4 hrs, reaching a value 210.3%, after which it levels off. The increase in %G is accounted for by the increase in number of grafting sites in the initial stages of reaction due to high rate of ceric ion participation in the formation of reactive sites at the cellulose backbone [25]. Since there is a large excess of acrylonitrile monomer even after the longer reaction times, the leveling off after 4 hrs is presumably due to initiator exhaustion [23]. These observations are in accordance to those observed by Cruz *et al.* [12], Gupta [25] and Hon [23].

It was also observed that %GE reaches a maximum value of 97% at polymerization time of 4 hrs. It does not change appreciably on prolonging the polymerization reaction for more than 4 hrs. This trend is in conformity of those reported for the grafting of vinyl monomers onto *Cassia tora* gum [26] and cellulose [30] with ceric ion as redox initiator. Thus, to obtain the maximum %G, the optimum reaction time is 4 hrs.

3.7. IR characterization

The FTIR spectra of the cellulosic material derived from bamboo and the optimized grafted sample (%G 210.3, %GE 97) were recorded. In the FTIR spectra of the optimized sample of grafted cellulose, besides the typical signals of cellulose backbone (ν_{OH} 3414 cm^{-1} , ν_{CH} 1431 cm^{-1} , ν_{COC} 1059 cm^{-1} , ν_{β} -linkage 890 cm^{-1}), the characteristic absorption bands at 2245 cm^{-1} , for the nitrile group ($-C\equiv N$) introduced and 2926 cm^{-1} (characteristic for $-CH_2$ group) with increased intensity were observed, fur-

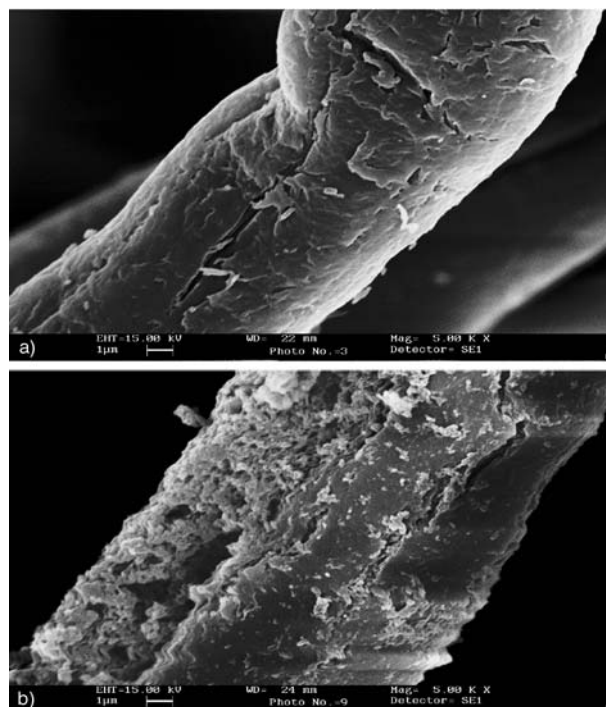


Figure 6. Scanning electron micrographs at 5000 magnification of (a) cellulosic material (b) acrylonitrile grafted cellulosic material

nishing thereby the evidence that grafting of acrylonitrile has occurred.

3.8. Surface morphology

SEM images at magnifications 5000 were obtained for parent and grafted cellulosic fibers. Figure 6 depicts the transformation in surface morphology of bamboo fiber on being subjected to grafting with acrylonitrile. The untreated bamboo fiber exhibits a relatively smooth surface compared with the grafted one. Moreover, growth and deposition of the grafted acrylonitrile on the surface and in the intercellular region of the bamboo fiber is clearly visible. Deposition on the surface of fiber resulting in the unevenness of the surface indicated that acrylonitrile was chemically bonded to the surface of the fiber. These results are in accordance to those reported by Cruz *et al.* [12].

3.9. Water sorbency

The WRV of the parent cellulosic material sample was 12.2 g/g and of grafted sample was 9.1 g/g. The WRV decreases on grafting indicating increased hydrophobic nature of the fibers on grafting. These

findings are in accordance to those reported by Das et al. [21].

4. Conclusions

Graft copolymerization of acrylonitrile onto cellulosic material derived from bamboo (*Dendrocalamus strictus*) (average DP 816) in heterogeneous medium can be initiated effectively with CAN. The optimum reaction conditions obtained for grafting of acrylonitrile onto cellulosic material were: duration of dipping cellulosic material in CAN solution 1 hr, CAN concentration 0.02 M, acrylonitrile concentration 24.6 mol/AGU, temperature of reaction 40°C and polymerization time 4 hrs. The %G for optimized samples is 210.3% and %GE is 97. The characterization of the grafted products by means of FTIR and SEM furnished the evidence of grafting of acrylonitrile onto the cellulosic material.

Acknowledgements

This study is a part of plan project funded by the Indian Council of Forestry Research & Education (ICFRE), Dehra Dun. Authors are thankful to the Director, Forest Research Institute, Dehra Dun for encouragement.

References

- [1] Clasen C., Kulicke W-M.: Determination of viscoelastic and rheo-optical material functions of water-soluble cellulose derivatives. *Progress in Polymer Science*, **26**, 1839–1919 (2001).
- [2] Barkalow D. G., Young R. A.: Cellulose derivatives derived from pulp and paper mill sludge. *Journal of Wood Chemistry and Technology*, **5**, 293–312 (1985).
- [3] Spasojevic L. D., Majdanac L. J., Petrovic S. D., Hrabar J. P., Nesovic V. M., Galovic Z. M., Cvetkovic M. D.: Optimization of carboxymethyl cellulose production. *Cellulose Chemistry and Technology*, **31**, 297–308 (1997).
- [4] Akaranta O., Otaigbe J. O. E., Onu C. O., Odozi T. O.: Carboxymethyl cellulose from *Musanga ceropioides* wood. *Cellulose Chemistry and Technology*, **22**, 315–319 (1988).
- [5] Patra C. M., Singh B. C.: Influence of N-acetylglycine on the kinetics of the ceric ion-initiated graft copolymerization of acrylonitrile and methyl methacrylate onto jute fibers. *Journal of Applied Polymer Science*, **52**, 1557–1568 (1994).
- [6] Patnaik S., Sarangi S., Mohanty A. K., Singh B. C.: Graft copolymerization of acrylonitrile onto jute fibers: Studies on Ce(IV) – hippuric acid redox system. *Journal of Applied Polymer Science*, **37**, 2099–2107 (1989).
- [7] Ghosh P., Ganguly P. K.: Polyacrylonitrile (PAN)-grafted jute fibers: Some physical and chemical properties and morphology. *Journal of Applied Polymer Science*, **52**, 77–84 (1994).
- [8] Samal R. K., Bhuyan B. L.: Chemical modification of lignocellulosic fibers. 1. Functionality changes and graft polymerization of acrylonitrile onto pineapple leaf fibers – their characterization and behavior. *Journal of Applied Polymer Science*, **52**, 1675–1685 (1994).
- [9] Khalil E. M. A., El-Wakil N. A.: Infrared absorption spectra of cyanoethylated cellulose fibres. *Cellulose Chemistry and Technology*, **34**, 473–479 (2000).
- [10] Vieira M. C., Heinze T., Antonio-Cruz R., Mendoza-Martinez A. M.: Cellulose derivatives from cellulosic material isolated from *Agave lechuguilla* and *fourcroydes*. *Cellulose*, **9**, 203–212 (2002).
- [11] Ramos L. A., Frollini E., Heinze T.: Carboxymethylation of cellulose in the new solvent dimethyl sulphoxide/tetrabutyl ammonium fluoride. *Carbohydrate Polymers*, **60**, 259–267 (2005).
- [12] Cruz R. A., Mendoza A. M., Vieira M. C., Heinze T.: Studies on grafting of cellulosic materials isolated from *Agave lechuguilla* and *fourcroydes*. *Die Angewandte Makromolekulare Chemie*, **273**, 86–90 (1999).
- [13] Tewari D. N.: A monograph on bamboo. International Book Distributors, Dehra Dun (1995).
- [14] Ambasta S. P.: The wealth of India: A dictionary of Indian raw materials & industrial products: Raw materials Vol. 2. B. CSIR Publication, New Delhi (1988).
- [15] Hebeish A., Guthrei J. T.: The chemistry and technology of cellulosic copolymers. Springer-Verlag, Berlin (1981).
- [16] Gürdag G., Güclü G., Özgümüş S.: Graft copolymerization of acrylic acid onto cellulose: Effects of pre-treatments and crosslinking agent. *Journal of Applied Polymer Science*, **80**, 2267–2272 (2001).
- [17] Khullar R., Varshney V. K., Heinze T., Vieira-Nagel, Gupta P. K., Naithani, S., Soni P. L.: Carboxymethylation of cellulose isolated from bamboo (*Dendrocalamus strictus*) and its rheology. *Cellulose Chemistry and Technology*, **40**, 545–552 (2007).
- [18] Khullar R., Varshney V. K., Naithani S., Soni P. L.: Study of the influence of reaction conditions for production of cyanoethylcellulose from cellulosic material derived from bamboo (*Dendrocalamus strictus*) *Journal of Natural Fiber*. Accepted for publication (2007).
- [19] Khullar R., Varshney V. K., Naithani S., Heinze T., Soni P. L.: Carboxymethylation of cellulosic material (average degree of polymerization 2600) isolated from cotton (*Gossypium*) linters with respect to degree of substitution and rheological behavior. *Journal of Applied Polymer Science*, **96**, 1477–1482 (2005).
- [20] Varshney V. K., Gupta P. K., Naithani S., Khullar R., Bhatt A., Soni P. L.: Carboxymethylation of α -cellulose isolated from *Lantana camara* with respect to degree of substitution and rheological behaviour. *Carbohydrate Polymers*, **63**, 40–45 (2005).

- [21] Das A., Saikia C. N., Hussain S.: Grafting of methyl methacrylate (MMA) onto *Anteraea assama* silk fiber. Journal of Applied Polymer Science, **81**, 2633–2641 (2001).
- [22] Gangneux A., Watteiz D., Marechal E.: Synthese et etude de celluloses echangeuses d'ions. Leur emploi dans l'epuration des eaux residuaires de l'industrie textile-1: Synthese d'une cellulose greffee par des chaines poly (acide acrylique) et d'une cellulose renfermant des fonctions ammonium quaternaire. European Polymer Journal, **12**, 535–541 (1976).
- [23] Hon D. N. S.: Graft copolymerization of lignocellulosic fibers. ACS Symposium Series, Washington (1982).
- [24] Kulkarni A. Y., Mehta P. C.: Ceric ion-induced redox polymerization of acrylonitrile on cellulose. Journal of Applied Polymer Science, **12**, 1321–1342 (1968).
- [25] Gupta S.: Chemical modification of *Cassia occidentalis* seed gum. Ph.D. Thesis, Forest Research Institute, Dehra Dun, 181–191 (2005).
- [26] Sharma B. R., Kumar V., Soni P. L.: Graft copolymerization of acrylonitrile onto *Cassia tora* gum with ceric ammonium nitrate-nitric acid as redox mixture. Journal of Applied Polymer Science, **90**, 129–136 (2003).
- [27] Athawale V. D., Vidyagauri V. L.: Graft copolymerization onto starch 3: Grafting of acrylamide using ceric-ion initiation and preparation of its hydrogels. Starch-Stärke, **50**, 426–431 (1998).
- [28] Hebeish A., Refie M. H. E., Higazy A., Ramadon M.: Synthesis, characterization and properties of polyacrylamide-starch composites. Starch-Stärke, **48**, 175–179 (1996).
- [29] Heikal S. O., El-Kalyubi S. F.: Graft copolymerization of acrylonitrile onto bagasse and wood pulp. Journal of Applied Polymer Science, **27**, 3027–3041 (1982).
- [30] Gupta K. C., Sahoo S.: Grafting of acrylonitrile and methyl methacrylate from their binary mixtures on cellulose using ceric ions. Journal of Applied Polymer Science, **79**, 767–778 (2001).

Studies on the preparation of multi-monomer grafted PP by one-step extrusion and the blends with PVC

L. L. Hou^{1*}, M. Zhao²

¹Hydrochem (S) PTE LTD, A Hyflux Group Company, 339339, Singapore

²Department of Fire Technology, the Chinese People's Armed Police Academy, Hebei 065000, P.R. China

Received 1 September 2007; accepted in revised form 22 October 2007

Abstract. Firstly, a novel grafted polypropylene (PP) was prepared by one step free-radical melt grafting method in a single-screw extruder. It was shown that the addition of St to the melt-grafting system as a comonomer could significantly enhance the grafting degree of MMA onto PP and reduced the degradation of PP matrix by means of FTIR and MFR tests, respectively. Then, the extruded multi-monomer grafted PP, as a component, was directly blended with poly(vinyl chloride) (PVC), denoted as gPP/PVC. The corresponding improved compatibility was examined. Due to the addition of gPP the tensile strengths of gPP/PVC blends increased significantly in comparison to pure polypropylene/poly(vinyl chloride) blends (PP/PVC), while the impact strengths remained unchanged. The DSC results also suggested that the compatibility of PP/PVC blends were improved largely.

Keywords: *polymer blends and alloys, multi-monomer grafted, polypropylene, poly(vinyl chloride), compatibility*

1. Introduction

Graft copolymers of PP have been widely used as compatibilizers in blends of PP with other plastics such as polyamides and polyesters, which were generally produced by the melt free radical grafting of monomers onto the PP chains. Various monomers have been used for melt grafting reaction. The most commonly employed monomers were maleic anhydride, glycidyl methacrylate and vinyl and acrylic monomers containing reactive functional groups [1–3].

However, the grafting yields of those monomers were usually low; and the PP matrix would undergo β -scission induced PP chain degradation in course of the grafting of polar monomers [4–6]. To obtain high grafting yields and to reduce side reactions, it was essential that the macroradicals react with the grafting monomer before they undergo side reactions. Recently, a so-called ‘comonomer concept’

was developed to improve the grafting yields of glycidyl methacrylate (GMA) onto PP and PE (polyethylene) [6, 8]. The idea of using a comonomer was associated with the commonly accepted fact that a free radical process starts with the formation of macroradicals along the polymer chains by a so-called hydrogen abstraction mechanism. These macroradicals might subsequently follow two competing pathways. They could either initiate the grafting of the monomer or undergo chain scission. The latter depends strongly on the nature of the polymer backbone. In the case of PP, the main side reaction was β -scission associated with PP macroradicals [6], which caused a reduction in the molecular weight of the polymer.

Styrene (St) was found to be a good comonomer to promote the melt free radical grafting and reduce the chain scission of PP matrix. It was believed to relate to the high reactivity towards PP macroradi-

*Corresponding author, e-mail: lianlong_hou@hyflux.com
© BME-PT and GTE

cals and the stability of the resulting product. St reacted rapidly with PP macroradicals and the resulting styryl macroradicals copolymerized readily with grafting monomer [4, 6, 9].

In this work we provide a detailed investigation on melt free radical grafting of methylmethacrylate (MMA) onto PP with St as a comonomer in a single-screw extruder and study its ability to improve the compatibility of otherwise incompatible blends. Specifically, the multi-monomer grafted polymer was synthesized, and then the grafted PP was directly blended with PVC to study the improved compatibility between PP and PVC. The mechanical properties, thermal behavior and morphology of the blends were investigated in detail. Meantime, the pure PP/PVC blend was prepared for comparison.

2. Experimental

2.1. Materials

PP and PVC used in this study were commercial products, the former was supplied by Daqing Petrochemical Factory (T30S, Heilongjiang, China), with a melt flow rate (MFR) of 3.5 g/10 min; the latter was the product of Baoding Electrochemical Plant (SG-6, suspension type, K value = 65–63, Hebei, China). The corresponding processing agents of PVC: tribasic lead sulfate (TLS), dibasic lead phosphate (DLP), stearic acid (SA), paraffin wax (PW) (industrial grade). The grafting monomers were MMA (Xintong Fine Chemical Co., Ltd, Tianjin, China) and St (Fuxing Chemical Factory, Beijing, China). Dicumyl peroxide (DCP) was chosen as an initiator purchased from Shanghai chemical reagent company (Shanghai, China).

2.2. Preparation and purification of the multi-monomer grafted PP

The radical initiator, MMA and St were introduced in a beaker firstly. The resultant mixture was dry-blended with PP pellets before charged into the extruder at room temperature for about 30 minutes so that they could be absorbed by the PP matrix. Then the reactions of melt grafting St and/or MMA onto PP were carried out in a single screw extruder of type XJ-20 (Scientific Research Instrument Factory, Jilin University, China). The screw diameter

(D) was 20 mm and the screw diameter-to-extruder length ratio excluding the die was 20. The extruding temperature was set at the range from 160 to 210°C.

The crude grafted samples were first dissolved in hot toluene and then precipitated in excess acetone at room temperature, the grafted PP and pure PP were precipitated whereas the homo- and co-polymer, such as poly (methylmethacrylate) (PMMA), polystyrene (PSt) and poly(styrene-co-methyl methacrylate) (PSt-co-PMMA) remained soluble. After that, the precipitated samples, denoted as PP-g-(St-co-MMA), were filtered and dried under vacuum at 80°C for 12 h.

2.3. Characterization of modified PP

Fourier Transform Infrared Spectroscopy (FTIR) was carried out with a FTS-40 spectrometer (BIO-RAD, Co., USA) in the range between 4000 and 500 cm^{-1} , with a resolution of 2 cm^{-1} at room temperature, which was used to determine the grafting yields of MMA and/or St onto PP.

MFR measurements of the purified PP samples were carried out using $^{\text{M}}$ PXRZ-400C Melt Indexer (Jilin University Scientific Research Instrument Factory, Jilin, China) at 230°C with a load of 2.16 kg weight according to the ASTM D1238 standard.

2.4. Measurements of mechanical properties of blends

PVC with its processing agents at a fixed weight ratio (PVC:TLS:DLP:SA:PW = 100:2:1:0.5:0.5) were first dry-mixed by high-speed mixer, followed by melt blending in a two roll mixing mill for plastics (XKR-160, Zhanjiang Machine Company, Guangdong, China) to plasticate for 4 min, and the plastication of PP or grafted PP (gPP) had the same procedure as that of PVC. PVC was added to plasticated PP or gPP followed by blending for another 4 min. After that, the blends were compressed into sheets with a hydraulic press at 180°C and 10 MPa for 5 min, which is designated as PP/PVC or gPP/PVC, respectively. The corresponding sheets were directly milled into standard testing specimens according to ASTM D638 and ASTM D 256 standard. Prior to each processing step, all sheets

were dried in a vacuum oven at 80°C for 12 h. Notched Izod impact strength was measured by a XCJ-40 impact tester (Chengde Laboratory Instrument Works, Hebei, China). Tensile testing was performed on an LJ-500N tensile test machine (Chengde Laboratory Instrument Works, Hebei, China) at a speed of 10 mm/min.

2.5. DSC investigation

Differential scanning calorimeter (DSC) measurements were carried out on a DT-40 Modulated DSC (Shimadzu, Kyoto, Japan) calibrated by indium standards. All the measurements were performed from room temperature to 200°C at a heating/cooling rate of 20°C/min under nitrogen atmosphere, and maintained at that temperature for 5 min to eliminate any previous thermal history. The glass transition temperature (T_g) was determined in the second heating scan.

3. Results and discussion

3.1. FTIR analysis of PP-g-(St-co-MMA)

The FTIR spectra of the pure PP, PP-g-MMA and PP-g-(St-co-MMA) are shown in Figure 1. The characteristic absorption peaks at 1730 cm^{-1} corresponded to the absorption of the carbonyl groups of

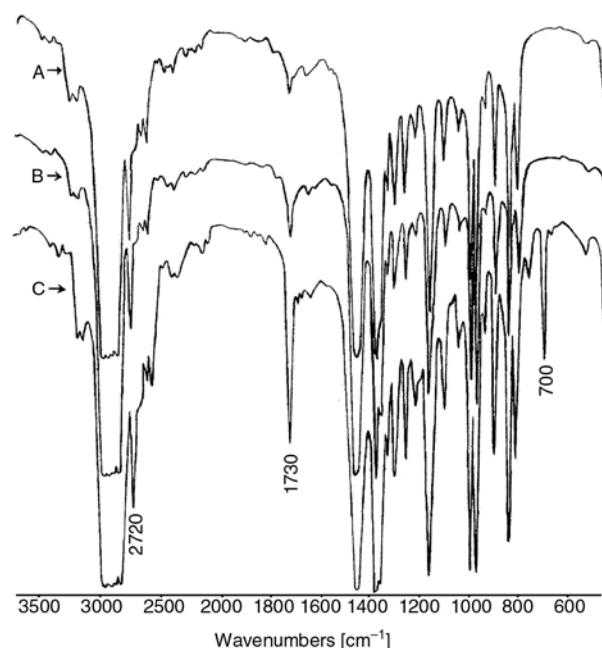


Figure 1. FT-IR Spectra of PP, PP-g-MMA and PP-g-(St-co-MMA). A: pure PP, B: PP-MMA, C: PP-g-(St-co-MMA)

MMA. The peaks at 700 and 2720 cm^{-1} are attributed to the characteristic absorption of the St and PP skeleton, respectively. The above-mentioned results illustrated that both MMA and St were grafted onto PP.

To obtain the quantitative results, the FTIR absorbance ratio technique is applied to determine the grafting yields [4, 12, 13]. The absorption peak at 2720 cm^{-1} was chosen as an internal reference and that at 1730 cm^{-1} were used to determine the grafting degree of MMA. The peak at 700 cm^{-1} corresponding to the stretching of the hydrogen atoms of the mono-substituted aromatic ring of St was chosen for measuring the amount of grafted St. The relative absorbance ratio (RAR) values of the areas of the peaks at 1730 (or 700) and 2720 cm^{-1} showed the relative grafting degree of MMA (or St).

3.2. Preparation and characterization of PP-g-(St-co-MMA)

The important contribution of using St as comonomer to enhance the MMA grafting yields and reduce β -scission induced PP chain degradation is illustrated in Figures 2 and 3 below.

Figures 2 and 3 show the RAR (relative absorbance ratio) and MFR values as a function of the molar ratio of [St]/[MMA] for a given concentration of MMA charged (6.0 phr), respectively. As seen from Figure 2, in the absence of St, the RAR value, which was an indicator of the grafting degree of MMA, was very low due to the low reactivity of MMA. Adding St as comonomer, the RAR values

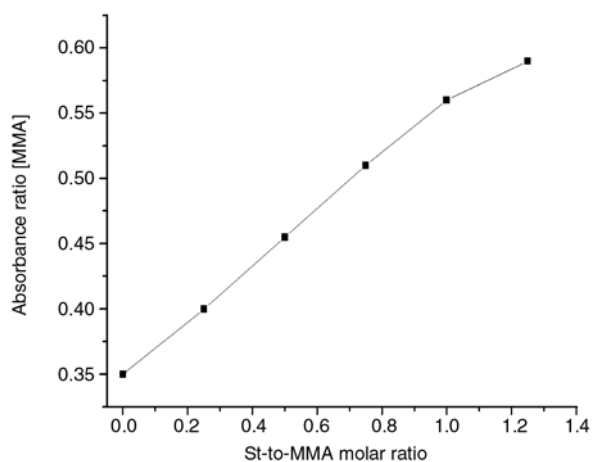


Figure 2. Effect of monomer molar ratios on grafting degree of the grafted PP

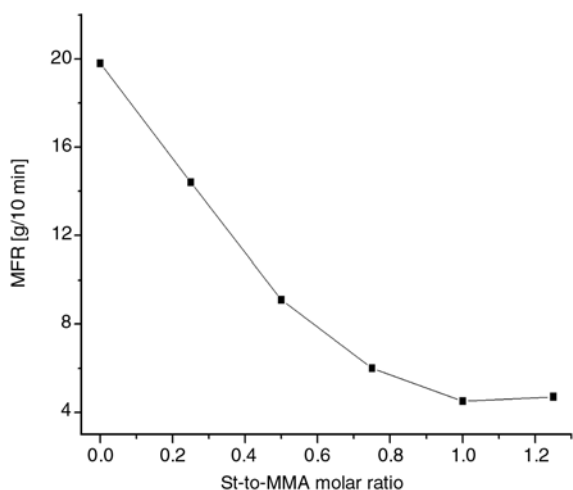


Figure 3. Effect of monomer molar ratios on MFR value of the grafted PP

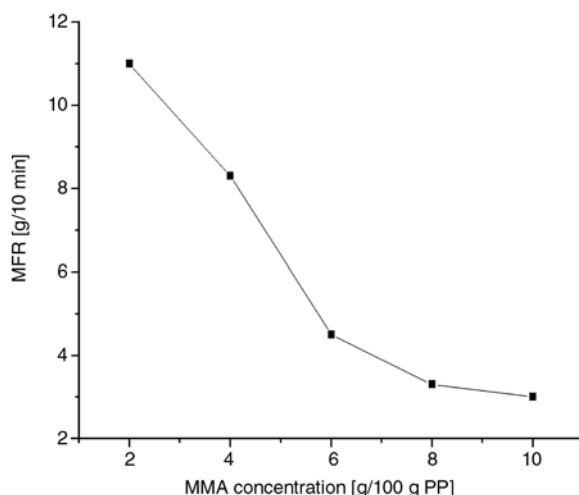


Figure 5. Effect of MMA concentration on MFR value of the grafted PP

ascended linearly with increasing the molar ratio of the two monomers until the ratio reached 1:1; thereafter the change slowed down. This might be caused by the more and more homo- and co-polymer [6], such as PMMA, PSt and PSt-PMMA, all these byproducts were obtained simultaneously with the grafting reaction. When the molar ratio was small, the grafting reaction was dominant; all above side reactions were negligible. With the molar ratio increasing, especially beyond 1:1, these side reactions affected the grafting yields declining to a large degree. The RAR values of MMA, on the other hand, always had larger value than that of St. It was interesting phenomenon to notice for us, because of the higher reactivity of St than that of MMA. In Figure 3, the MFR value decreased drastically from 19.8 to 4.6 as the molar ratio increased 1:1 and then leveled off.

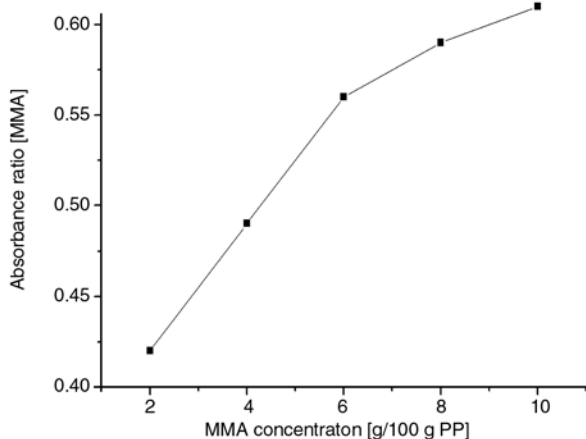


Figure 4. Effect of MMA concentration on grafting degree of the grafted PP

For a given condition, DCP concentration and the molar ratio of [St]/[MMA] were fixed at 0.6 phr and 1:1, respectively. Figure 4 shows that the more the monomers (MMA or St) were added, the higher the RAR values of MMA and St. Figure 5 shows the effect of grafting monomer concentration on MFR values of the grafted PP obtained at the same conditions as Figure 4. The MFR values of the grafted PP decreased with increasing monomer concentration, and some had similar values to that of pure PP, which meant that the addition of St reduced the degradation of PP effectively.

From Figures 3 and 5, it was clear to see that the degradation of PP chain was reduced significantly with the St content adding; otherwise, the ability for St to promote the MMA grafting yields might be obtained from Figure 4. In another word, the comonomer, St, could reduce β -scission of PP to a great extent and provided an additional freedom to control different monomers' grafting yields in some systems.

In order to investigate the influences of DCP on grafting degree and MFR values of the grafted PP, the monomer molar ratio was fixed at 1:1 and the two grafting monomers content were 6 phr based on PP. It could be seen from Figure 6 that the changes of the RAR values were large. In the beginning, because the most DCP was consumed by the grafting reaction, the RAR value increased significantly and reached a peak value at 0.6 phr DCP. However, Figure 7 shows that the MFR values had a little change when the content of DCP was ranged from 0.2 to 0.8 phr. With the content of

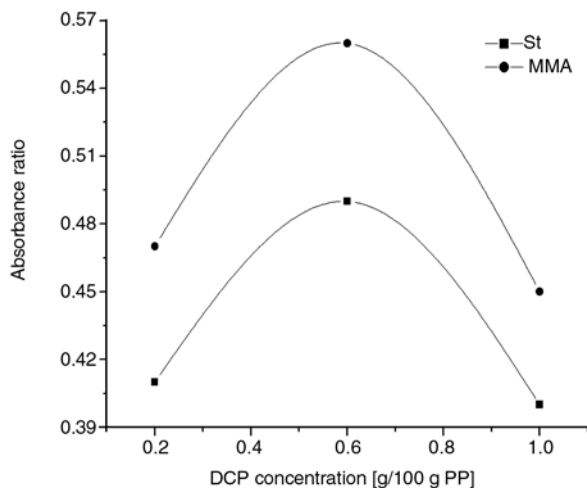


Figure 6. Effect of DCP on grafting degree of the grafted PP

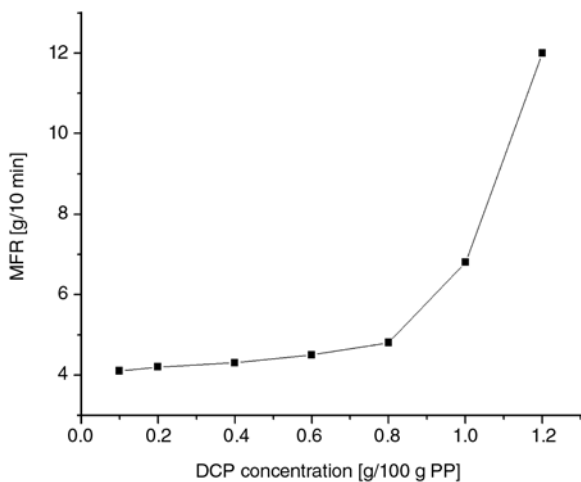


Figure 7. Effect of DCP on MFR value of the grafted PP

DCP increased consecutively, the RAR values decreased rapidly and the MFR values increased; the more the concentration of DCP, the more the decrease of the RAR values and the increase of the MFR values. This might be related to the increased degradation of the PP matrix. Therefore, the surplus of the DCP content was harmful to the graft reactivity. Thus, the optimal concentrations for St, MMA and DCP is 6.0, 6.0, and 0.6, respectively based on PP, the corresponding grafted PP are directly blended with PVC to study their compatibility. Additionally, it was interesting to note that, the RAR values of MMA were higher than that of St and no longer limited by a plateau but increased with increasing initial concentration of MMA. The similar phenomenon was found at other grafting systems. [6–9]. As a result, a comonomer St could

Table 1. Mechanical properties of pure PP, PVC, gPP and their blends

PP [g]	PVC [g]	gPP [g]	Tensile strength [MPa]	Impact strength [KJ/m ²]
0	100	0	45.00	–
100	0	0	35.17	2.014
0	0	100	34.72	1.777
20	80	0	9.16	1.599
40	60	0	9.39	1.447
60	40	0	22.74	1.483
80	20	0	28.06	1.746
0	80	20	19.99	1.630
0	60	40	7.57	1.659
0	40	60	23.61	1.684
0	20	80	34.31	1.794

provide an additional freedom to control different monomers’ grafting yields in some systems.

3.3. Mechanical proprieties of PP/PVC and gPP/PVC blends

PP and PVC are two kinds of important plastics, they were widely used in many fields. Due to their different polarity, poor adhesion, and high interfacial tension, they are incompatible. Thus, the corresponding blend possessing useful properties could not be obtained by direct blending of the two polymers and there were only a few reports on the subject [14–17]. In this study, the multi-monomer grafted PP as a compatibilizer was directly added to PVC and carried on a systematic study.

Table 1 summarizes the mechanical properties of gPP/PVC blends with different proportions. In addition, the mechanical properties of PP/PVC binary blends were also given for comparison. From it we could see that, although the tensile strength of pure PVC (45.00 MPa) was higher than that of PP (35.17 MPa), the tensile strength of PP/PVC blends significantly reduced with the PVC content increasing. Therefore, it was impossible to obtain the good material by direct melt blending of PP and PVC. However, the tensile strengths of gPP/PVC blends were increased largely except for the weight ratio of 40/60 (gPP/PVC). Namely, the multi-monomer grafted PP could improve the compatibility of PP/PVC blend and enhance the tensile strength, whereas the phase inversion played a major role at the weight ratio 40/60 of gPP/PVC. The impact strength of gPP/PVC was unchanged as that of PP/PVC with the whole study range.

Additionally, the grafted PP contained C=O groups, which should be present in the phase interfaces of blends, could form hydrogen bonding with H atom of PVC, which could reduce the interfacial free energy, and decrease the interfacial tension and increase the adhesion between two different phases. On the other hand, due to the similar of dissolubility parameter (δ) about PVC ($\delta = (19.0-22.1) \cdot 10^{-3}(\text{Jm}^{-3})^{1/2}$) and PMMA ($\delta = 19.0 \cdot 10^{-3}(\text{Jm}^{-3})^{1/2}$) [11], according to the principle (the good compatibility of different polymers with the similar values), the MMA chain diffused toward PVC matrix, and the PP part in the grafted PP produced eutectic crystal with PP, thus the grafted PP could take the most optimum conformations at the interface and play its compatibility role

Table 2. Effect of gPP or PP contents on the T_g of PVC in gPP or PP/PVC blends

The weight ratio of PP (or gPP)/PVC blends	80/20	60/40	40/60	20/80
$T_{g(\text{PVC})}$ of PP/PVC [°C]	88.7	89.2	90.1	90.4
$T_{g(\text{PVC})}$ of gPP/PVC [°C]	77.9	79.1	84.3	86.0

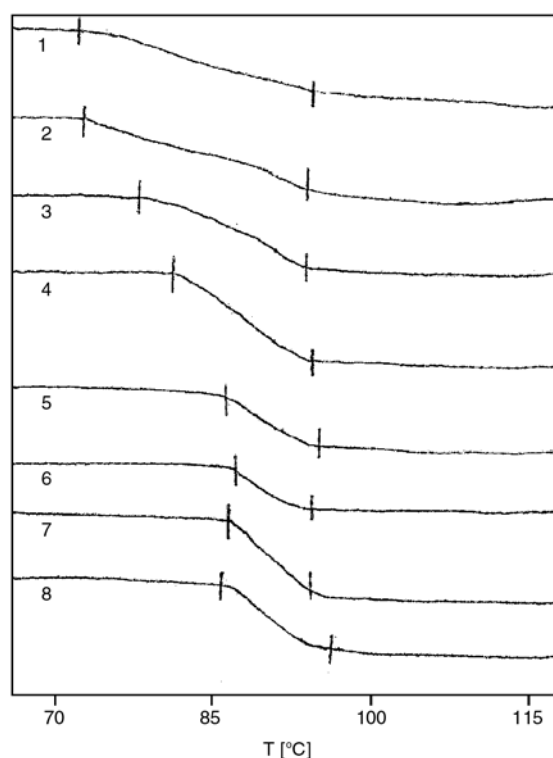


Figure 8. DSC curves for gPP/PVC and PP/PVC blends with different weight ratios. gPP/PVC: (1) 80/20, (2) 60/40, (3) 40/60, and (4) 20/80; PP/PVC: (5) 80/20, (6) 60/40, (7) 40/60, and (8) 20/80

fully [18]. Actually, the grafted polymer acted as an anchor at the interface of PP and PVC.

3.4. DSC investigation

Table 2 is the T_g values of PVC portion in the two different blends, which was denoted as $T_{g(\text{PVC})}$. From it we could see, due to the poor compatibility of PP and PVC, the $T_{g(\text{PVC})}$ values (about 90°C) were almost independent with the weight ratio of PP/PVC blends varying. However, adding the gPP to PVC, it was not difficult to find that all the $T_{g(\text{PVC})}$ values reduced and tended to that of PP (-14°C). As the weight ratio of gPP/PVC was 80/20, the $T_{g(\text{PVC})}$ value decreased about 11°C. Meanwhile, as it can be seen in Figure 8, the $T_{g(\text{PVC})}$ range become wide with the gPP concentration addition. The more gPP were added, the more the $T_{g(\text{PVC})}$ range broadened. All this showed that the gPP improved the compatibility of PP/PVC blends to a certain extent.

4. Conclusions

The multi-monomers melt grafting onto polypropylene was successfully prepared by one-step in a single-screw extruder, and characterized by means of FTIR and MFR. The effects of monomer molar ratio, monomer concentration, and initiator concentration on the grafting reaction were investigated in detail. It was shown that the addition of St to the melt-grafting system as a comonomer could significantly enhance MMA grafting degree onto PP and reduce the chain scission of PP. The maximum MMA grafting degree was obtained when the molar ratio of [St]/[MMA] was about 1:1; and the MFR value of the gPP reached the lowest one in this case, too. As a compatibilizer, compared to pure PP/PVC blends, the tensile strength of gPP/PVC blends was increased significantly with impact strength maintenance; expect for the phase inversion regions. Moreover, the T_g s of DSC results also exhibited that PP-g-(St-co-MMA) improved the compatibility between PP and PVC.

References

- [1] Yanjarappa M. J., Sivaram S.: Recent developments in the synthesis of functional poly(olefin)s. *Progress in Polymer Science*, **27**, 1347–1398 (2002).

- [2] Chung T. C.: Synthesis of functional polyolefin copolymers with graft and block structures. *Progress in Polymer Science*, **27**, 39–85 (2002).
- [3] Neoh S. B., Azanam S. Hashim: Highly grafted polystyrene-modified natural rubber as toughener for polystyrene. *Journal of Applied Polymer Science*, **93**, 1660–1665 (2004).
- [4] Sun Y-J., Hu G-H., Lamba M.: Free radical grafting of methacrylate onto polypropylene in a co-rotating twin screw extruder. *Journal of Applied Polymer Science*, **57**, 1043–1057 (1995).
- [5] Ciardelli F., Aglietto M., Passaglia E., Picchioni F.: Controlled functionalization of olefin/styrene copolymers through free radical processes. *Polymers for Advanced Technologies*, **11**, 371–376 (2000).
- [6] Cartier H., Hu G-H.: Styrene-assisted melt free radical grafting of glycidyl methacrylate onto polypropylene. *Journal of Polymer Science, Part A: Polymer Chemistry*, **36**, 1053–1063 (1997).
- [7] Hu G-H., Cartier H.: Styrene-assisted melt free radical grafting of glycidyl methacrylate onto an ethylene and propylene rubber. *Journal of Applied Polymer Science*, **71**, 125–133 (1999).
- [8] Cartier H., Hu G-H.: Styrene-assisted free radical grafting of glycidyl methacrylate onto polyethylene in the melt. *Journal of Polymer Science Part A: Polymer Chemistry*, **36**, 2763–2774 (1998).
- [9] Li Y., Xie X-M., Guo B-H.: Study on styrene-assisted melt free-radical grafting of maleic anhydride onto polypropylene. *Polymer*, **42**, 3419–3425 (2001).
- [10] Fu Z-S., Fan Z-Q., Zhang Y-Q., Feng L-X.: Structure and morphology of polypropylene/poly(ethylene-copolypropylene) in situ blends synthesized by spherical Ziegler-Natta catalyst. *European Polymer Journal*, **39**, 795–804 (2003).
- [11] Liu C., Zou H. W., Liu P. B.: Study on mechanical properties and optical transparency of PVC/SBS/MBS blend. *China Plastics Industry*, **35**, 17–19 (2007).
- [12] Chen L-F., Wong B., Baker W. E.: Melt grafting of glycidyl methacrylate onto polypropylene and reactive compatibilization of rubber. *Polymer Engineer and Science*, **36**, 1594–1607 (1996).
- [13] Xie X-M., Chen N-H., Guo B-H., Li S.: Study on multi-monomers melt-grafting onto PP in an extruder. *Polymer International*, **49**, 1677–1683 (2000).
- [14] Chung T. C., Rhubright D.: Polypropylene-graft-poly-caprolactone: Synthesis and applications in polymer blends. *Macromolecules*, **27**, 1313–1319 (1994).
- [15] Kim B. J., White J. L.: Compatibilized blends of PVC/PA12 and PVC/PP containing poly(lauryl lactam-block-caprolactone). *Journal of Applied Polymer Science*, **91**, 1983–1992 (2004).
- [16] Xanthos M.: Interfacial agents for multiphase polymer systems: Recent advances. *Polymer Engineer and Science*, **28**, 1392–1399 (1988).
- [17] Byong J. K., James L. W.: Compatibilized blends of PVC/PA12 and PVC/PP containing poly(lauryl lactam-block-caprolactone). *Journal of Applied Polymer Science*, **91**, 1983–1992 (2004).
- [18] Tung T., Chen H., Zhang X., Li L., Huang B.: Molecular state of graft copolymers in the interfacial area of polyolefin and polar polymer. *Polymer*, **35**, 4240–4242 (1994).

Preparation and characterization of electrically conductive composites of poly(vinyl alcohol)-g-poly(acrylic acid) hydrogels impregnated with polyaniline (PANI)

A. K. Bajpai*, J. Bajpai, S. N. Soni

Bose Memorial Research Laboratory, Department of Chemistry, Government Autonomous Science College, Jabalpur, 482 001 (M.P.), India

Received 21 August 2007; accepted in revised form 2 November 2007

Abstract. Novel electrically conducting composite materials consisting of poly(aniline) (PANI) nanoparticles dispersed in a poly(vinyl alcohol) (PVA)-g-poly(acrylic acid) (PAA) hydrogels were prepared within the polymer matrix by *in situ* polymerization of aniline. The conversion yield of aniline into PANI particles was determined gravimetrically while structural confirmation of the synthesized polymer was sought by Fourier Transform Infrared (FTIR), UV-visible analysis and X-ray diffraction (XRD) technique. Morphology and dimension of PANI particles embedded into the colored optically semi-transparent hydrogels were evaluated by Scanning Electron Microscopy (SEM) analysis. Electrical conductivity of composite hydrogels of different composition was determined by LCR meter while electroactive behavior of composite hydrogels swollen in electrolyte solution was investigated by Effective Bend Angle (EBA) measurements.

Keywords: smart polymers, polymer composites, conducting polymers

1. Introduction

A thermodynamic system capable of transforming chemical energy directly into mechanical work is known as a chemo-mechanical system. Many artificial chemo-mechanical systems made of environmentally sensitive polymer gels are being developed for sensor/actuator system such as controllable membrane separation system and electrically regulated drug delivery system [1].

A gel containing ionic groups can be actuated isothermally by an electric field. When the gel is negatively charged, it swells near the anode and contracts near the cathode, the contraction rate being proportional to the external electric current [2].

The absolute change in volume is by no means insignificant-dimensional changes of say some percents are quite usual. Such a gel bar made of poly-electrolyte materials can bend backwards and

forward by the application of an electric field. Water and ions migrate towards the electrode bearing a change opposite in sign to the net change in the gel, and this coupling of electro-osmosis and electrophoresis is thought to be responsible for the observed chemo-mechanical behavior [3].

Electrically conducting polymers (ECPs) and in particular polyaniline, polypyrrole, polythiophene and their derivatives have been the subject of intensive research for their unique electrical, electrochemical and/or optical properties [4–5] and uncountable applications [6–10]. ECPs are also named ‘conjugated polymers’ because they are macromolecules containing a spatially extended π bonding system, which is the reason of their intrinsic semiconducting nature.

Polyaniline is the one of the most promising conducting polymers due to a good combination of

*Corresponding author, e-mail: akbmrl@yahoo.co.in
© BME-PT and GTE

properties, stability, price and ease of synthesis by different routes [11–22]. It exists in a variety of reversible protonated and oxidized forms, differing for electrical, electrochemical and/or optical properties like many ECPs [23–25]. PANI is difficult to process because it is soluble only in a limited number of organic solvents.

Electrically conducting polymers can be prepared by the polymerization of aniline in acidic medium, resulting in the formation of polyaniline (PANI) [26]. Influence of polymerization parameters on the molecular weight of polyaniline has been studied [27] and a new aggregation mechanism for shape and aggregation control of PANI nanoparticles was suggested [28]. PANI is known as being stable, most promising, and of low cost so different synthetic routes have been developed like one phase emulsion polymerization process [29], Triton Y-100 [30], potentiometric method [31], polymerization by different oxidizing agents like cupric sulphate [32], iron (III) chloride [33]. PANI nanowires have also been potentiostatically deposited on a stainless steel electrode [34]. The polymerization process for PANI and poly(2-methoxy-aniline) (POMA) nanotubes formation was also investigated [35]. Electrically conducting hydrogel composites made of PANI nanoparticles and poly(H-vinyl-O-/m amino acetophenone of different compositions were synthesized by oxidative polymerization [36, 37]. PANI powder with crystalline semi-conducting ZnS composite by mechanical mixing was also found to increase conductivity [38]. Similarly, PANI/Co₃O₄ was synthesized [39] to overcome the solubility problem of PANI. Lee *et al.* [40] reported direct patterning of conducting water-soluble polymers. Some more aspects of preparation methods and properties of polyaniline blends and composites with organic polymer have also been reviewed [41].

Thus, being motivated by the significant and diversified applications of PANI and related conducting polymers, the present paper aims at synthesizing a PANI impregnated graft copolymer PVA-g-PAA and characterizing it by various analytical techniques such as FTIR, SEM and UV-visible analysis. The selection of PVA and PAA as the hydrogels components of the polymer matrix lies in their unlimited applications in medicine, biology and technology [42–44]. The present paper also

describes the results on electroactive behavior of the graft copolymer impregnated with PANI molecules.

2. Experimental

2.1. Materials

Polyvinyl alcohol (PVA) (98.6% hydrolyzed) was obtained from Research Lab, Mumbai, India and used as received. Acrylic acid (AA) was purchased from Merck Limited (Mumbai, India) and purified by vacuum distillation at 55°C. Other chemicals such as aniline (AN), hydrochloric acid, potassium persulphate (KPS), ammonium persulphate (APS), N,N'-methylene bis acrylamide (MBA) were also of analytical grade and used without any further purification.

2.2. Methods

2.2.1. Preparation of gel

A polymer matrix composed of PVA-g-PAA was prepared by using MBA as crosslinker and KPS as polymerizing initiator. Schematically, the reaction mechanism may be displayed as shown in Figure 1. In a typical experiment, 1 g PVA was dissolved in 25 ml of hot double distilled water and to this solution were added precalculated amounts of acrylic acid (43.7 mM), MBA (19.45·10⁻² mM) and KPS (11.10·10⁻² mM). The whole reaction mixture was homogenized and kept in a petri dish (corning glass, 2.5" diameter) maintained at 35 ± 0.2°C for 24 h. After the reaction is over, the whole mass converted into a semi-transparent film and it was purified by equilibrating it in double distilled water for a week. The swollen gel was dried at room tem-

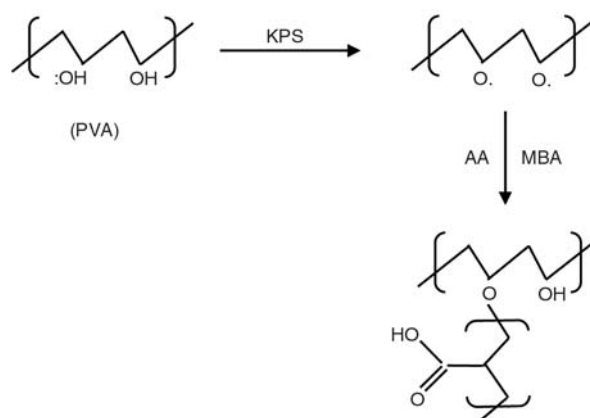


Figure 1. A reaction scheme for graft co-polymerization of PAA onto PVA

perature, cut into rectangular size piece and stored in airtight plastic bags.

2.2.2. PANI impregnation

Required quantity of AN (10.74 mM) was dissolved in 0.5 N HCl (50 ml) and the gel prepared was allowed to soak in the AN solution for 24 h. The aniline (AN) containing swollen gel was dried and then again left in a 0.3 M APS bath to soak required quantity of APS in solution (0.5 N HCl). As soon as the gel swells in APS solution, the entrapped APS initiates polymerization of AN via the mechanism shown in Figure 2.

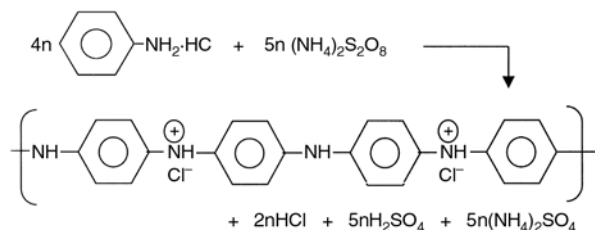


Figure 2. Reaction scheme showing the polymerization of aniline

As the polymerization progresses, the semi-transparent gel turns into black. The PANI impregnated gel is repeatedly washed with distilled water and allowed to dry at $30 \pm 0.2^\circ\text{C}$ for 72 h.

The percentage impregnation of PANI into the gel was calculated by the Equation (1):

$$[\%] \text{ Impregnation of PANI} = \left(\frac{W_{\text{PANI}} - W_{\text{Dry}}}{W_{\text{Dry}}} \right) \cdot 100 \quad (1)$$

where, W_{PANI} is weight of the dry PANI impregnated gel and W_{Dry} is the initial weight of polymer gel.

In order to achieve the objectives undertaken in the study, hydrogels of different composition were prepared by varying the amounts of PVA, AA, MBA, KPS, AN and APS in the feed mixture of the hydrogel.

2.3. Characterization

2.3.1. Fourier Transform Infrared (FTIR) spectra

To gain insights into the structural information of the prepared PANI impregnated gel, the FTIR spectra of PANI powder, polymer hydrogels and PANI-impregnated matrix were recorded in a FTIR

spectrophotometer (FTIR-8400S, Shimadzu). For recording FTIR spectra of native and PANI impregnated films, quite thin and transparent films of respective samples were prepared by solution casting method and the prepared films were directly mounted on spectrophotometer.

2.3.2. UV-visible analysis

UV-visible analysis was also carried out on a double beam UV-VIS spectrophotometer (Systronics, 2201, Ahmedabad, India). For scanning UV-spectra, thin films of samples (native and PANI impregnated) were prepared of sizes $3 \times 1 \times 0.05 \text{ cm}^3$ by solution casting method and put in to the quartz cuvette in vertical orientation.

2.3.3. X-ray diffraction (XRD) analysis

In order to gain insights into the crystalline nature of the prepared native and PANI impregnated gel, the X-ray diffraction spectra were recorded using a Philips (Holland) automated X-ray powder diffractometer. The dried gels were placed on the glass slide specimen holder and exposed to X-rays in a vertical goniometer assembly. The scan was taken between 10 to 90° with a scanning speed of $2.4^\circ \cdot \text{min}^{-1}$. The operating target voltage was 35 kV, tube current was 20 mA and radiation used was $\text{FeK}\alpha$ ($\lambda = 0.193 \text{ nm}$).

2.3.4. Particle size analysis

The distribution of particle size of prepared PANI powder was measured by a particle size analyser (Fritsch Particle Sizer Analysette). The PANI particles were prepared as described below:

A known quantity of aniline ($10.74 \cdot 10^{-2} \text{ mM}$) was dissolved into 50 ml of 0.5 N HCl and to this solution of aniline was added 0.3 M APS. The reaction mixture was kept for polymerization at room temperature for 24 hrs and the resulting polyaniline precipitate was filtered, washed and dried at 35°C for 24 hrs. The PANI powder so prepared was stored in airtight polythene bags.

2.3.5. Scanning Electron Microscopy (SEM) analysis

The SEM of the prepared native and PANI impregnated gels were recorded on a scanning electron microscope (Philips 515) for their surface morphological structure.

2.3.6. Electrical conductivity

The electrical conductivity of prepared gels were measured by Four probe LCR meter (Masstech Digital M/M No. MAS 830L) with the help of silver electrode pressed on both sides of the gel. The electrical conductivity of gels of different compositions was also measured.

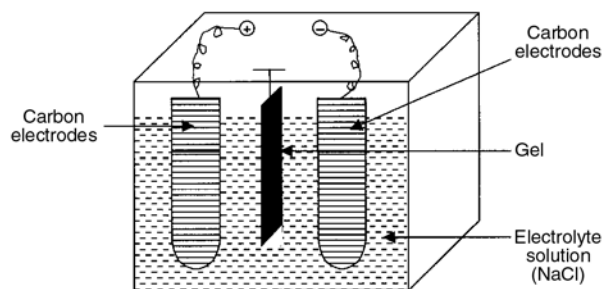


Figure 3. A home-made apparatus for measuring effective bend angle

2.3.7. Effective Bend Angle (EBA) analysis

In order to demonstrate the sensitivity of the gel to the applied external electric field, the bending of the gel under the applied field was measured using a home-made device as shown in Figure 3.

Samples were prepared with varying PANI impregnation percentage and allowed to attain equilibrium swelling in the NaCl aqueous solution at room temperature before electrical stimulation. The same solution was taken in the glass case equipped with two parallel carbon electrodes fixed 30 mm apart at the centre of the glass case. A rectangular specimen having dimensions of $15 \times 1 \times 1 \text{ mm}^3$ was cut and placed vertically at the center of the two electrodes fixing one end of the specimen at the top. The DC voltage was applied across the solution between electrodes and the equilibrium-bending angle was measured with a protractor.

2.3.8. Reproducibility of data

All measurements were carried out at least thrice and average value was utilized for presentation of results. It was found that the experimental errors had never been greater than 1%.

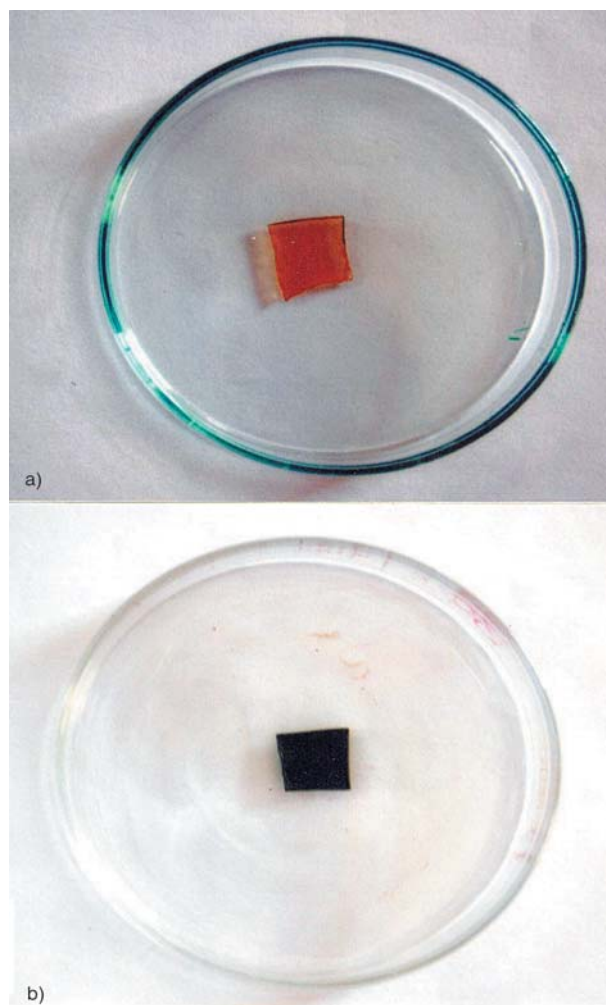


Figure 4. Physical appearance of (a) PVA-g-PAA gel and (b) PANI impregnated PVA-g-PAA gel

3. Results and discussion

3.1. Characterization of gels

3.1.1. Physical appearance

Figures 4a and b depict appearance of the native and PANI impregnated gels which provide a clear evidence of impregnation of PANI into the polymer gel matrix. As evident from the photographs, whereas the native gel is semi-transparent in color while the impregnated gel appears dark-green, which could be attributed to the formation of PANI within the matrix.

3.1.2. FTIR spectra

Figures 5a and b represent FTIR spectra of PVA and PVA-g-PAA polymer films, respectively scanned in the range $400\text{--}4000 \text{ cm}^{-1}$. The characteristic peaks at $1730\text{--}1854 \text{ cm}^{-1}$ are due to the pres-

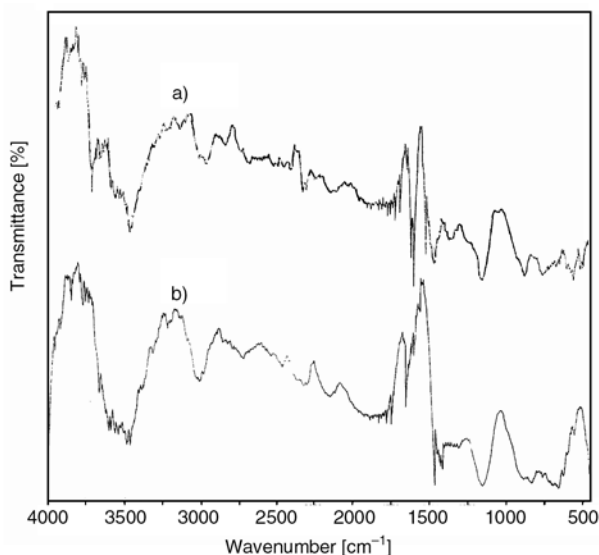


Figure 5. FTIR spectra of (a) PVA and (b) PVA-g-PAA gel

ence of C=O stretching vibration and the peak observed at 650 cm^{-1} is due to the OH out of plane vibration of the carboxylic groups of PAA which appears in the spectra of grafted polymers only, i. e., PVA-g-PAA (Figure 5b). This obviously confirms the grafting reaction. The characteristic peaks at 3468 and 3473 cm^{-1} in both the spectra (a) and (b) are due to the presence of OH groups of PVA, while the spectral bands between 3470 and 3600 cm^{-1} are due to OH stretching vibration of PVA and PAA, respectively, which also confirm the grafting of

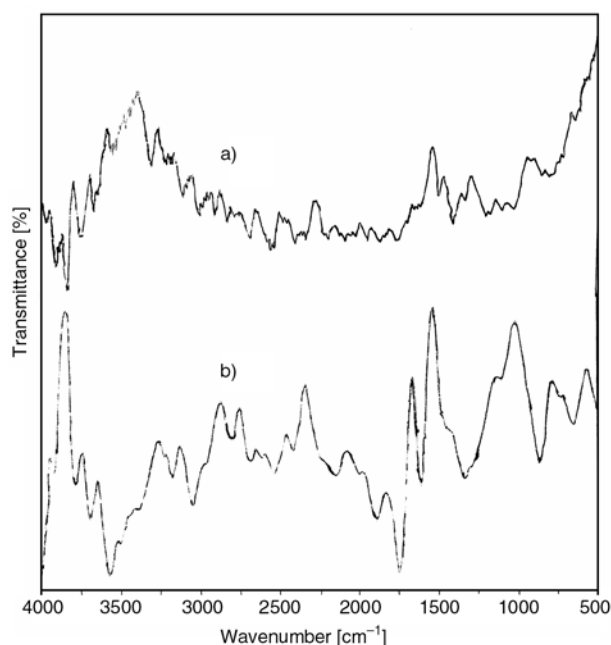


Figure 6. FTIR spectra of (a) PANI powder and (b) PVA-g-PAA impregnated PANI gel

PAA into PVA. The characteristic peak at 1162 cm^{-1} is due to the formation of acetal ring.

Figures 6a and b represent the FTIR spectra of PANI powder and PANI impregnated PVA-g-PAA gel film. The characteristic peaks in Figure 6a appearing at 824 , 1144 and 1312 , 1505 , and 1590 cm^{-1} indicate aromatic C–H, aromatic amide, and aromatic C–C stretching vibrations, respectively. The spectra (b) of PANI impregnated PVA-g-PAA gel film contain peaks at 876 , 1150 , 1347 , 1500 and 1614 cm^{-1} indicating the presence of aromatic C–H, aromatic amide, and aromatic C–C stretching vibrations which confirm the impregnation of PANI into the gel (polymer matrix).

3.1.3. UV-visible spectral analysis

The UV-visible analysis of PVA-g-PAA film and PANI impregnated PVA-g-PAA film was carried out in the range of 200 to 800 nm . It is observed that two characteristic peaks at 334 and at 632 nm in PANI impregnated PVA-g-PAA film spectra (Figure 7b) indicates the presence of PANI into the gel whereas these peaks are not visible in the spectra of PVA-g-PAA (Figure 7a). This obviously confirms the impregnation of PANI into the gel because the emeraldine form of PANI has two characteristic peaks at 334 and 632 nm originating from π - π^* transition of benzenoid rings and the exciton absorption of the quinoid rings, respectively.

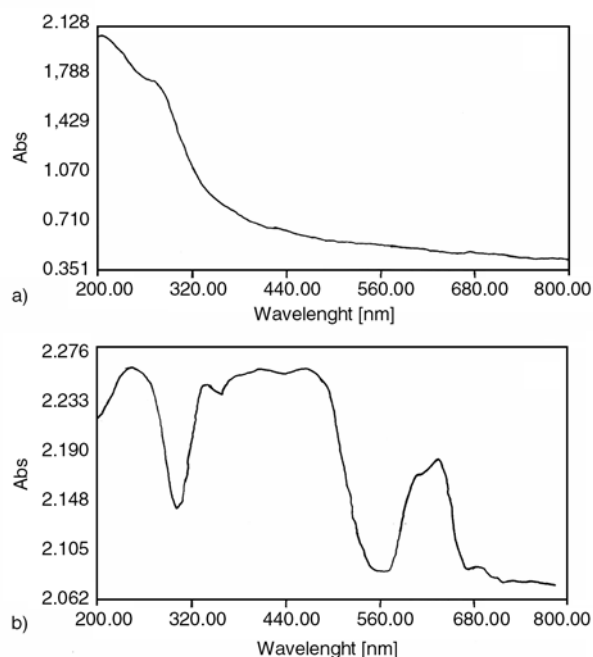


Figure 7. UV-visible spectra of (a) native (PVA-g-PAA) gel and (b) PANI impregnated gel

3.1.4. X-ray diffraction analysis

The XRD patterns of the prepared native and PANI impregnated gels are shown in Figures 8a and b, respectively. Figure 8a shows a prominent peak near 20° , which corresponds to the (101) plane of the PVA crystal. Other minor peaks around 21° and 22° could be attributed to minor crystallites of grafted polyacrylic acid chains.

The diffraction patterns of PANI impregnated gel are shown in Figure 8b which not only shows a characteristic peak at 20° (due to PVA) but also depicts a prominent peak at 25° , which is a characteristic peak of PANI. Thus, the XRD-patterns of impregnated gel provides an additional evidence of PANI formation within the polymer matrix.

A comparison of the peak area of the two diffractograms clearly indicates that upon PANI impregnation, the polymer matrix loses its crystallinity as evident from the increase in broadness of the XRD spectra (b). The loss in crystallinity due to PANI impregnation may be explained by the fact that because of *in situ* polymerization of aniline within the matrix, the PANI chains produced due to polymerization may bring disorder in the chains packing and, therefore, may result in a loss of crystallinity.

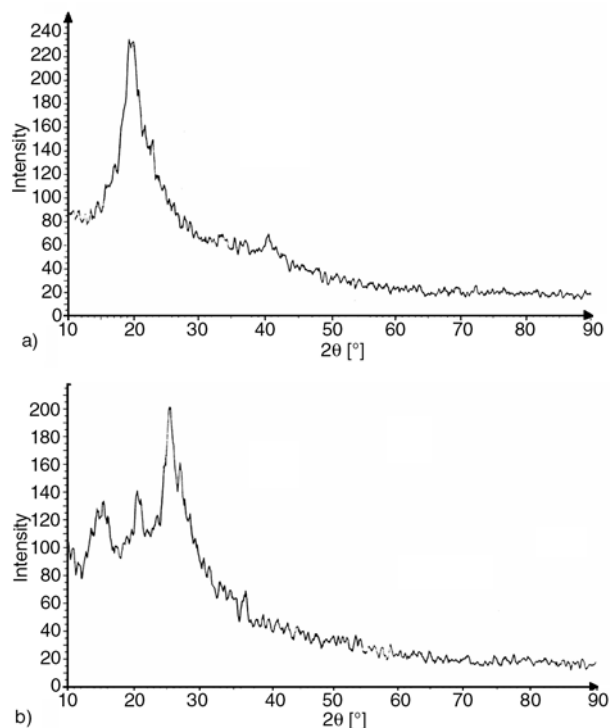


Figure 8. XRD-spectra of (a) native (PVA-g-PAA) gel and (b) PANI impregnated gel

3.1.5. SEM

The morphological features of the prepared native and PANI impregnated composite films have been studied by recording SEM images of the films as shown in Figure 9a and b, respectively. It is clear from the image (a) that the surface of the native gel is quite homogeneous and shows no cracks, voids or unevenness. This suggests that after grafting of polyacrylic acid chains onto PVA backbone, the matrix remains homogeneous in composition. However, impregnation of PANI into the matrix develops heterogeneity in the matrix as evident from the SEM image (b). It is clear from the image (b) that impregnated PANI molecules form clusters like morphology varying in the sizes 0.5 to $2\ \mu\text{m}$. The formation of PANI clusters within the polymer matrix could be attributed to hydrophobic nature of the PANI molecules, which may aggregate due to hydrophobic dispersion forces.

3.1.6. Particle size analysis

The particle size distribution curve of the prepared PANI powder is shown in Figure 10 which indicates that the size of the particles vary in the range

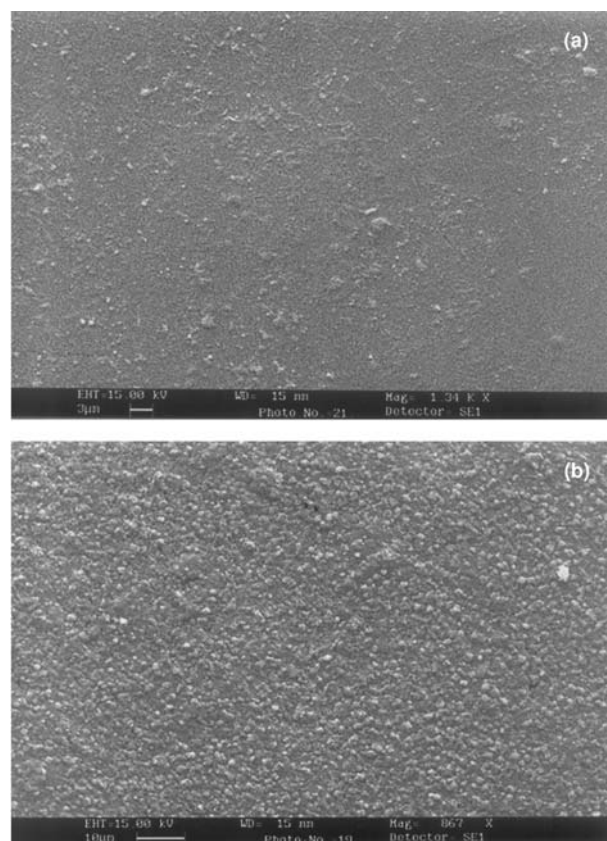


Figure 9. SEM image of (a) native (PVA-g-PAA) gel and (b) impregnated gel

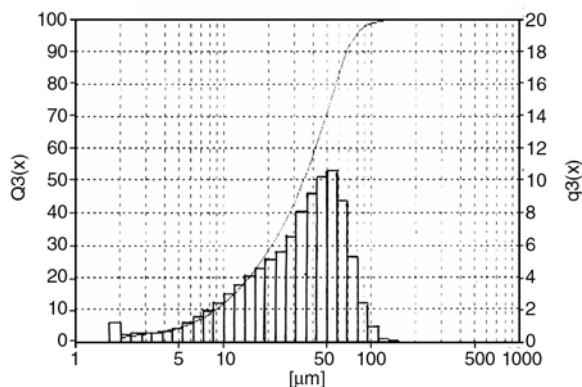


Figure 10. Particle size distribution curve of PANI powder

1 to 100 μm and greatest fraction of particles possess a size of 50 μm . The variation in size of PANI particles could be attributed to varying degree of aggregation of particles under existing experimental conditions.

3.2. PANI impregnation and effects of ingredients

In the present study, AN has been taken as a monomer and in order to get it polymerized within the polymer matrix, it is essential that AN molecules should penetrate into the polymer gel. To achieve the desired objectives of AN polymerization, the monomer AN was dissolved in HCl which formed aniline hydrochloride, thus, yielding cationic species of AN. Now, because of positive charge over the AN molecule, its diffusion into the matrix will be controlled by operative electrostatic forces as well as swelling nature of the hydrogel matrix. It is important to notice here that the polymer matrix is hydrophilic in nature while AN molecules are hydrophobic. In this way one cannot expect hydrophobic/hydrophilic forces being mainly responsible for diffusion of AN. It is, therefore, convincing to consider electrostatic forces as the main factor to cause diffusion of AN into the polymer matrix. Moreover, the presence of PAA segments in the matrix will also contribute to the electrostatic interaction between the entering AN molecules and the matrix itself. Impregnation of PANI into the polymer matrix is basically dependent on the extent of swelling of the polymer film in aniline hydrochloride solution and its subsequent polymerization within the matrix. Thus, the inclusion of aniline into the polymer should definitely be

a function of the chemical composition (and nature also) of the hydrogel and this has been investigated further by varying the concentration of the constituents components of the gel as discussed in the following para.

3.2.1. Effect of PVA

To study the effect of PVA on PANI impregnation, PVA was varied in the range 1.0 to 3.0 g keeping quantities of other ingredients constant. The results summarized in Table 1 reveal that the amount of impregnated PANI constantly increases with increasing PVA concentration in the gel up to 1.5 g. The results may be explained by the fact that with increasing PVA, the hydrophilicity of the matrix increases that allows more aniline to enter into the matrix, which upon polymerization produces greater amount of PANI while beyond 1.5 g of PVA, PANI impregnation decreases. This is due to the fact that the increasing PVA content decreases the interionic repulsion between the PAA chain which allows lesser number of aniline molecules to enter the polymer matrix that results in a decrease in PANI impregnation.

3.2.2. Effect of AA

The influence of AA variation on the extent of PANI impregnation has been investigated by varying the concentration of AA in the range 14.6 to 43.7 mM while keeping the other constituents concentration constant. The results are shown in Table 1, which indicate an increase in the impregnated amount of PANI with increasing PAA content. The increase in PANI impregnation may be explained by the fact that due to ionic nature of PAA, its increasing content in the gel results in interionic repulsion between the PAA chains, which permits a large number of AN molecules to enter the polymer matrix. This results in an enhanced impregnation.

3.2.3. Effect of MBA

The effect of increasing concentration of MBA on the extent of PANI impregnation has been studied by varying its concentration in the range $6.5 \cdot 10^{-2}$ to $25.9 \cdot 10^{-2}$ mM while keeping the other concentration terms constant. The results are shown in Table 1, which show that the amount of impregnated PANI increases initially with the increasing

Table 1. Effect of concentration of constituents of the gel on the amount of PANI impregnation

PVA content [g]	PANI impregnation [%]	Other ingredients
1.0	3.57	AA – 29.1 mM MBA – $13.0 \cdot 10^{-2}$ mM KPS – $7.39 \cdot 10^{-2}$ mM APS – 0.3 M in 0.5 N HCl AN – 10.74 mM in 0.5 N HCl
1.5	3.80	
2.0	3.37	
3.0	1.18	
AA content [mM]	PANI impregnation [%]	Other ingredients
14.6	1.85	PVA – 1 g MBA – $13.0 \cdot 10^{-2}$ mM KPS – $7.39 \cdot 10^{-2}$ mM APS – 0.3 M in 0.5 N HCl AN – 10.74 mM in 0.5 N HCl
29.1	3.57	
36.0	5.75	
43.7	7.55	
MBA content [mM]	PANI impregnation [%]	Other ingredients
$6.50 \cdot 10^{-2}$	12.50	PVA – 1 g AA – 43.7 mM KPS – $7.39 \cdot 10^{-2}$ mM APS – 0.3 M in 0.5 N HCl AN – 10.74 mM in 0.5 N HCl
$13.00 \cdot 10^{-2}$	6.48	
$19.45 \cdot 10^{-2}$	32.69	
$25.90 \cdot 10^{-2}$	19.05	
KPS content [mM]	PANI impregnation [%]	Other ingredients
$3.69 \cdot 10^{-2}$	4.35	PVA – 1 g AA – 43.7 mM MBA – $19.45 \cdot 10^{-2}$ mM APS – 0.3 M in 0.5 N HCl AN – 10.74 mM in 0.5 N HCl
$7.39 \cdot 10^{-2}$	4.07	
$11.10 \cdot 10^{-2}$	10.00	
$14.80 \cdot 10^{-2}$	3.26	
AN content [mM]	PANI impregnation [%]	Other ingredients
5.30	6.25	PVA – 1 g AA – 43.7 mM MBA – $19.45 \cdot 10^{-2}$ mM KPS – $11.10 \cdot 10^{-2}$ mM APS – 0.3 M in 0.5 N HCl
10.74	9.40	
16.11	33.66	
21.48	6.70	
APS concentration [M]	PANI impregnation [%]	Other ingredients
0.2	16.67	PVA – 1 g AA – 43.7 mM MBA – $19.45 \cdot 10^{-2}$ mM KPS – $22.20 \cdot 10^{-2}$ mM AN – 10.74 mM in 0.5 N HCl
0.3	14.19	
0.4	4.21	
0.5	9.09	

concentration of MBA in the range $6.5 \cdot 10^{-2}$ to $19.45 \cdot 10^{-2}$ mM while beyond $19.45 \cdot 10^{-2}$ mM, a fall is noticed. The results may be interpreted by the fact that in the initial concentration range of MBA, the increase observed is due to an enhanced hydrophilicity of the matrix, which in turn, attracts a larger number of aniline hydrochloride molecules to diffuse into the gel which upon subsequent polymerization forms greater amount of PANI. However, beyond $19.45 \cdot 10^{-2}$ mM of MBA, much greater crosslinked network becomes compact and restrains the mobility of both incoming aniline molecules as well as the relaxation of polymer matrix chain. This clearly results in a less amount of PANI impregnation.

3.2.4. Effect of KPS

In the present study, the effect of KPS on PANI impregnation has been investigated by varying the concentration of KPS in the range $3.69 \cdot 10^{-2}$ to $14.8 \cdot 10^{-2}$ mM. The results are summarized in Table 1 which clearly reveal that the amount of impregnated PANI increases with increasing KPS in the range $3.69 \cdot 10^{-2}$ to $11.10 \cdot 10^{-2}$ mM while beyond $11.10 \cdot 10^{-2}$ mM, a fall is obtained. The observed increase may be attributed to the reason that as the concentration of KPS increases, the molecular weight (and also size) of polymer chain decreases which results in a formation of network with large number of pores, but of smaller size, which obviously intakes greater number of AN

molecules, thus, giving rise to greater impregnation.

However, beyond $11.10 \cdot 10^{-2}$ mM of KPS, much smaller size of network pores could restrict the diffusion of AN molecules into the polymer gel, and therefore, results in a decrease in the extent of impregnation.

3.2.5. Effect of AN

The effect of AN (monomer) concentration on PANI impregnation within the polymer matrix has been studied by varying the concentration of AN in 0.5 N HCl solution in the range 5.3 to 21.48 mM while keeping the concentration of other constitution of the gel as constant. The results are shown in Table 1 which indicate that the extent of PANI impregnation increases with increasing AN content within the matrix while beyond 16.11 mM of aniline concentration, the extent of impregnation decreases. The observed findings may be explained by the fact that as AN is a monomer of PANI, its increasing concentration in the gel will obviously facilitate more polymerization and therefore, extent of impregnation increases. However, beyond a definite concentration, i. e., 16.11 mM, the decrease observed in PANI impregnation could be due to a lower degree of swelling in AN hydrochloride solution as much greater ionic concentration (because of aniline hydrochloride ion) in the external solution may result in lower swelling which permits less number of AN molecules for polymerization.

3.2.6. Effect of APS concentration

The influence of concentration of APS on PANI impregnation was studied by varying its concentration in the range of 0.2 to 0.5 M keeping other concentration terms constant. The results summarized in Table 1 show that the amount of impregnated PANI decreases with increasing APS concentration. The reason for the observed decrease may be explained by the fact that at low APS concentration, high molecular weight PANI might have been produced whereas at higher APS concentration, the PANI formed would be of lower molecular weight and, therefore, the possibility of leaching of low molecular weight, PANI could not be ruled out. This may consequently result in low impregnation.

3.3. Electrical conductivity and effects of ingredients

The electrical conductivity of polymer composite in different weight ratio of ingredients has been studied and it is found that the electrical conductivity of the gel is enhanced after impregnation of PANI. Moreover, the conductivity also varies with the constituents of the polymer matrix as discussed below.

3.3.1. Effect of PVA

The effect of PVA content on the conductivity of the matrix has been studied by varying the amount of PVA in the range 1 to 3 g. The results are depicted in Table 2, which reveal that the matrix shows an optimum conductivity at 1 g of PVA content while a drastic fall of about 10 times is noticed in conductivity when the concentration of PVA increases to 1.5 g. However, beyond 1.5 g of PVA content, almost no change in conductivity is observed. The results may be explained as below: The conductivity is determined by both the extent of PANI impregnation as well as poly acrylic acid content of the matrix. The former, in turn, is dependent on the hydrophilicity of the matrix. When the concentration of PVA increases from 1 to 1.5 g, the weight fraction of ionic polymer (PAA) decreases in the matrix. This obviously results in fall in conductivity of the matrix. However, beyond 1.5 g of PVA, increase in PVA content does not bring down the conductivity further, which may be attributed to the fact that the matrix acquire an optimum hydrophilic nature and, therefore, does not show further drop in conductivity.

3.3.2. Effect of PAA

In order to study the influence of PAA on the conductivity of the matrix, the concentration of the AA was increased in the range 14.6 to 43.7 mM and electrical conductivity was measured. The results are shown in Table 2, which reveal that the conductivity gradually increases with increasing PAA content in the gel. The results are quite expected and may be explained by the fact that on increasing the concentration of PAA, the number of COO^- groups increases along the macromolecular chain which add to the electrical conductivity of the matrix by

Table 2. Effect of concentration of constituents of the gel on conductivity

PVA content [g]	Conductivity native [S/cm]	Conductivity PANI impregnated [S/cm]	Other ingredients
1.0	$0.38 \cdot 10^{-2}$	$3.33 \cdot 10^{-2}$	AA – 29.1 mM
1.5	$0.19 \cdot 10^{-2}$	$0.37 \cdot 10^{-2}$	MBA – $13.0 \cdot 10^{-2}$ mM
2.0	$0.27 \cdot 10^{-2}$	$0.38 \cdot 10^{-2}$	KPS – $7.39 \cdot 10^{-2}$ mM
3.0	$0.56 \cdot 10^{-2}$	$0.77 \cdot 10^{-2}$	APS – 0.3M in 0.5N HCl
			AN – 10.74 mM in 0.5N HCl
AA content [mM]	Conductivity native [S/cm]	Conductivity PANI impregnated [S/cm]	Other ingredients
14.6	$0.63 \cdot 10^{-2}$	$2.19 \cdot 10^{-2}$	PVA – 1 g
29.1	$0.53 \cdot 10^{-2}$	$2.24 \cdot 10^{-2}$	MBA – $13.0 \cdot 10^{-2}$ mM
36.0	$0.27 \cdot 10^{-2}$	$2.60 \cdot 10^{-2}$	KPS – $7.39 \cdot 10^{-2}$ mM
43.7	$0.46 \cdot 10^{-2}$	$2.79 \cdot 10^{-2}$	APS – 0.3 M in 0.5 N HCl
			AN – 10.74 mM in 0.5 N HCl
MBA content [mM]	Conductivity native [S/cm]	Conductivity PANI impregnated [S/cm]	Other ingredients
$6.50 \cdot 10^{-2}$	$0.01 \cdot 10^{-2}$	$0.32 \cdot 10^{-2}$	PVA – 1 g
$13.00 \cdot 10^{-2}$	$0.01 \cdot 10^{-2}$	$1.27 \cdot 10^{-2}$	AA – 43.7 mM
$19.45 \cdot 10^{-2}$	$0.11 \cdot 10^{-2}$	$2.87 \cdot 10^{-2}$	KPS – $7.39 \cdot 10^{-2}$ mM
$25.90 \cdot 10^{-2}$	$0.22 \cdot 10^{-2}$	$2.87 \cdot 10^{-2}$	APS – 0.3 M in 0.5 N HCl
			AN – 10.74 mM in 0.5 N HCl
AN content [mM]	Conductivity native [S/cm]	Conductivity PANI impregnated [S/cm]	Other ingredients
5.30	$0.75 \cdot 10^{-2}$	$5.97 \cdot 10^{-2}$	PVA – 1 g
10.74	$0.75 \cdot 10^{-2}$	$3.59 \cdot 10^{-2}$	AA – 43.7 mM
16.11	$0.75 \cdot 10^{-2}$	$3.84 \cdot 10^{-2}$	MBA – $19.45 \cdot 10^{-2}$ mM
21.48	$0.75 \cdot 10^{-2}$	$9.10 \cdot 10^{-2}$	KPS – $11.10 \cdot 10^{-2}$ mM
			APS – 0.3 M in 0.5 N HCl

facilitating conduction of electrons along the PANI chain.

It is also mention that with increasing concentration of PAA, percent impregnation of PANI also increases in the studied range, which thus, contributes to the observed increase in conductivity.

3.3.3. Effect of MBA

In the present investigation, the role of crosslinker has been investigated by varying the amount of crosslinker in the concentration range $6.5 \cdot 10^{-2}$ to $25.9 \cdot 10^{-2}$ mM and observing the change in electrical conductivity. The results are shown in Table 2, which show that the conductivity sharply increases with increasing concentration of MBA in the range $6.5 \cdot 10^{-2}$ to $19.45 \cdot 10^{-2}$ mM while after $19.45 \cdot 10^{-2}$ mM of crosslinker; the conductivity acquires a limiting value.

The observed initial steep increase in conductivity with increasing concentration of MBA may be attributed to the fact that with increasing crosslinker concentration, the network density increases which results in a compact network, thus, facilitating flow of electrons responsible for conductivity behavior. However, beyond an optimum

concentration of crosslinking agent, the gels acquire optimum compactness and, therefore, no further increase in conductivity is observed.

3.3.4. Effect of AN

The effect of PANI content on the conductivity of the matrix has been investigated by increasing the concentration of aniline in the range 5.3 to 21.48 mM in the feed mixture of the gel. The results are given in Table 2 which indicate that the conductivity increases with increasing concentration of AN. The results are quite obvious and may be explained by the fact that with increasing concentration of AN solution, greater number of AN molecules will be available within the matrix for polymerization and as a subsequence, the extent of impregnation also increases.

3.4. Bending behaviour of the matrix

Swollen polyelectrolyte gels when kept under an applied electric field normally exhibit a bending towards the electrodes. This is called Electro-mechano-chemical (EMC) behavior and has been recognized as a promising phenomenon in designing smart materials.

3.4.1. Effect of PANI content

Inclusion of PANI molecules within the polymer matrix is expected to enhance the EMC behaviour and, therefore, has been studied by varying the PANI content in the range 0 to 30% at different applied voltages as shown in Figure 11. The results clearly reveal that the effective bending angle (EBA) constantly increases with increasing PANI content. The observed results may be explained by the fact that the greater the PANI content of the matrix, the larger would be the conductivity of the matrix, which in turn, will respond easily to the applied voltage.

It is also noticed from the Figure 11 that at 10 and 30% of PANI content, the bending is exactly same for a given voltage. The reason for the same bending angle at higher PANI content is that the PANI impregnated matrix acquires optimum conductance and, therefore, shows no further bending. Alternatively, it is also likely that the PANI chains are of the matrix may restrain the bending of the matrix. The Figure 12 also indicates that the magnitude of effective bending angle also increases with increasing applied voltage across the electrodes. The increase in effective bending angle may be attributed to the fact that with increase in voltage the charged matrix is attracted more and more towards the electrodes and thus, the bending angle increases.

3.4.2. Effect of voltage

There is a lower critical voltage (LCV) below which no bending of matrix is observed. In the present study, the LCV is found to be 3.0 volt. Thus, the bending phenomenon is observed only after 3.0 V and, therefore, the effect of voltage on bending phenomenon has been investigated in the range 6.0 to 12.0 V for a given PANI content. The influence of applied voltage on the EMC behavior of the matrix has been studied by varying the voltage in the range 6.0 to 12.0 V. The results are depicted in Figures 12 a, b and c which indicate that the EMC behavior of the matrix shows an increase in effective bending angle with increasing voltage at 0.1, 0.2 and 0.3 N NaCl solution. The observed results are quite obvious as with increasing voltage, the charged matrix shows greater attraction towards electrodes and, therefore, bending angle increases.

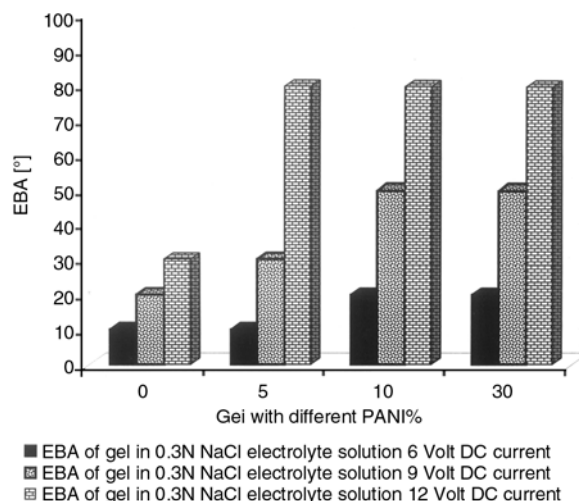


Figure 11. Effect of PANI contents on EBA

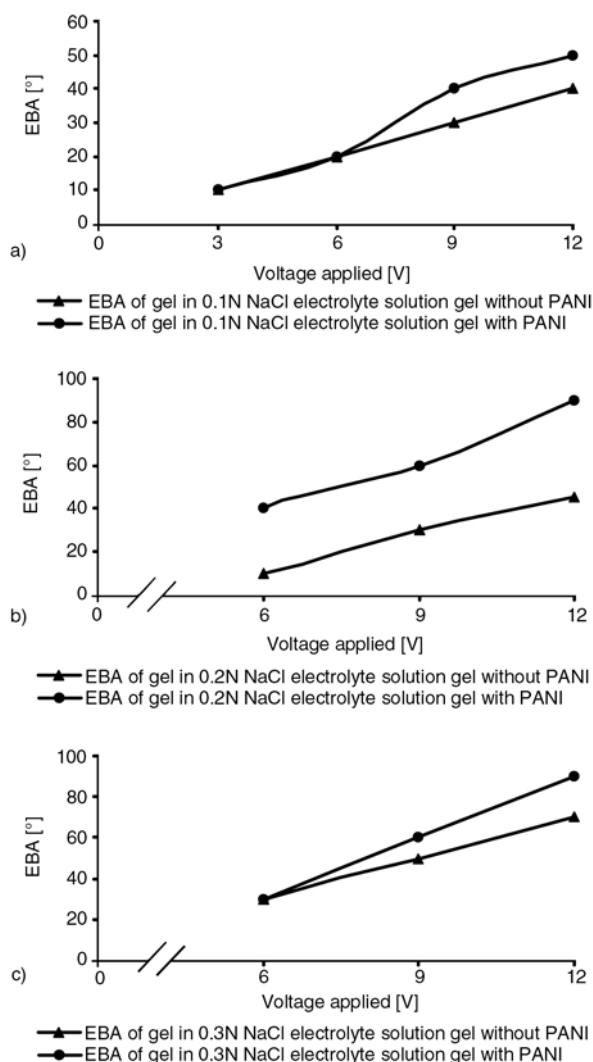


Figure 12. Effects of applied voltage on EBA in (a) 0.1 N NaCl electrolyte solution, (b) 0.2 N NaCl electrolyte solution, and (c) 0.3 N NaCl electrolyte solution

3.4.3. Effect of electrolyte concentration

The concentration of electrolyte solution is an important experimental parameter to exert a significant influence on the effective bending angle of the polymer matrix. The effect of increasing concentration of NaCl solution on bending of the gel has been studied by varying the concentration of NaCl in the range 0.1 to 0.3 N. The results are shown in Figures 13 a, b and c which reveal that the bending angle substantially increases up to 0.2 N NaCl solution and thereafter, it becomes almost constant showing no further increase in bending. The results may be attributed to the fact that increased concentration of NaCl solution facilitates bending of the polymer matrix by binding salt ion to the polyelectrolyte matrix so as to make it more responsive to the applied field. However, beyond 0.2 N NaCl

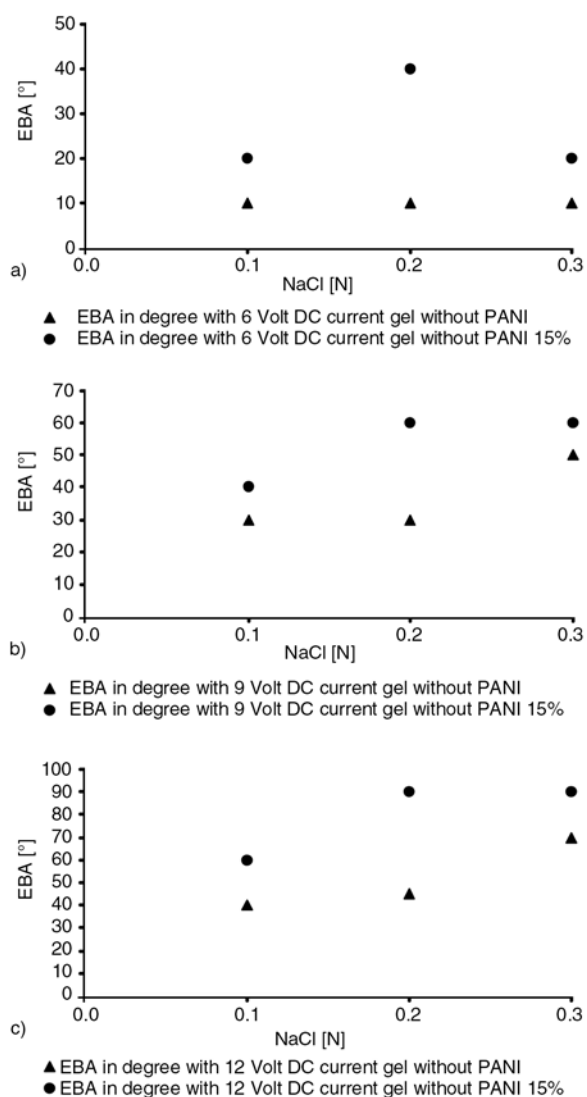


Figure 13. Effect of strength of electrolyte solution in (a) 6 Volt, (b) 9 Volt, and (c) 12 Volt

concentration when the charged centers present along the polyelectrolyte molecules are almost completely ionized, further effect on the effective bending angle of the polymer matrix may not likely to occur. This clearly explains the limiting bending of the matrix at highest applied voltage.

4. Conclusions

Impregnation of polyaniline into poly(vinyl alcohol)-g-poly(acrylic acid) results in a composite hydrogel which shows fair electroconductive and electroactive behaviors. The FTIR spectra of PANI impregnated hydrogel show characteristic peaks of poly aniline and other functional groups of constituent polymers, i. e., PVA and PAA. The impregnation of PANI into polymer matrix is further confirmed by UV spectral analysis. The impregnation of PANI within the polymer matrix brings about a loss in crystallinity as confirmed by the XRD spectra of the native and PANI impregnated gels. The hydrogel composite shows cluster like morphology varying in size between 0.5 to 2.0 μm . The polyaniline (PANI) particles undergo aggregation and show a wide variation in their sizes ranging from 1 to 100 μm .

The extent of PANI impregnation depends on chemical composition of the composite hydrogel. It is noticed that with increasing PVA, MBA, KPS and AN concentration, the amount of PANI impregnation increases up to a certain range and thereafter decreases. On the other hand, whereas an increase in impregnation results with increasing PAA content, a fall in impregnation is observed with increasing APS concentration.

The electrical conductivity also varies with varying composition of the composite. The conductivity increases with increasing PVA and MBA concentration while a drop in conductivity is observed if concentrations are increased further. In the case of AN, the conductivity constantly increases.

The PANI impregnated matrix shows bending behavior when a fixed voltage is applied in the presence of an electrolyte solution (NaCl). The gels show an enhanced bending behavior with increasing PANI content and applied voltage. Moreover, a greater bending is noticed with increasing concentration of electrolyte solution.

References

- [1] Kajiwara K., Ross-Murphy S. B.: Synthetic gels on the move. *Nature*, **355**, 208–209 (1992).
- [2] Kurkuri M. D., Lee J.-R., Han J. H., Lee I.: Electroactive behaviour of poly(acrylic acid) grafted poly(vinyl alcohol) samples, their synthesis using a Ce^(IV) glucose redox system and their characterization. *Smart Materials and Structure*, **13**, 417–423 (2006).
- [3] Ma J. T., Liu L. R., Yang X. J., Yao K. D.: Bending behaviour of gelatin/poly(hydroxyethyl methacrylate) IPN hydrogel under electric stimulus. *Journal of Applied Polymer Science*, **56**, 73–77 (1995).
- [4] Blanchet G. B., Fincher C. R., Lefenfeld M., Roger J. A.: Contact resistance in organic thin film transistors. *Applied Physics Letters*, **84**, 296–298 (2004).
- [5] Tittu M., Hiekkataipale P., Kainen J. H., Makela T. Ikkala O.: Viscoelastic and electrical transitions in gelation of electrically conducting polyaniline. *Macromolecules*, **35**, 5212–5217 (2002).
- [6] Akbayir C., Bulut F., Farrell T., Goldschmidt A., Günther R., Kam A. P., Miclea P., Scherf U., Seekamp J., Solovyev V. G., Sotomayor Torres C. M.: Nanostructured conjugated polymeric system for photovoltaic applications. *Reviews on Advanced Materials Science*, **5**, 205–210 (2003).
- [7] Tiitu M., Talo A., Forsén O., Ikkala O.: Aminic epoxy resin hardeners as reactive solvents for conjugated polymers: Polyaniline base/epoxy composites for anti-corrosion coatings. Elsevier Science (2005). *Polymer*, **46**, 6855–6861 (2005).
- [8] Li M., Guo Y., Wei Y., MacDiarmid A. G., Lelkes P. I.: Electrospinning polyaniline-contained gelatin nanofibers for tissue engineering applications. *Biomaterials*, **27**, 2705–2715 (2006).
- [9] Kim D.-H., Abidian M., Martin D. C.: Conducting polymers grown in hydrogel scaffolds coated on neural prosthetic devices. *Journal Of Biomedical Materials Research, Part A*, **71**, 577–585 (2004).
- [10] Qiang Y., Antony J., Sharma A., Nutting J., Meyer D.: Iron/iron oxide core shell nano clusters for biomedical application. *Journal of Nanoparticles Research*, **8**, 489–496 (2005).
- [11] Schmid A. L., Torresi. S. I. C., Bassetto A. N., Carlos I. A.: Structural, morphological and spectroelectrochemical characterization of poly(2-ethyl aniline). *Journal of the Brazil Chemical Society*, **11**, 317–323 (2000).
- [12] Ansari R., Keivani M. B.: Polyaniline conducting electroactive polymers, thermal and environmental stability studies. *Journal of Chemistry*, **3**, 202–217 (2006).
- [13] Ryu K. S., Chang S. H., Kang S.-G., Oh E. J., Yo C. H.: Physicochemical and electrical characterization of polyaniline induced by crosslinking, stretching and doping. *Bulletin of the Korean Chemical Society*, **20**, 333–336 (1999).
- [14] Jang S.-Y., Seshadri V., Khil M.-S., Kumar A., Marquez M., Mather P. T., Sotzing G. A.: Welded electrochromic conductive polymers nanofibres by electrostatic spinning. *Advanced Material*, **17**, 2177–2180 (2005).
- [15] Deore B. A., Yu I., Anguiar P. M., Siedler C. R., Freund M. S.: Highly crosslinked, self doped polyaniline exhibiting unprecedented hardness. *Chemical Materials*, **17**, 3803–3805 (2005).
- [16] Huang J.: Synthesis and applications of conducting polymer polyaniline nanofibers. *Pure and Applied Chemistry International*, **78**, 15–27 (2006).
- [17] Tang B. Z., Geng Y., Sun Q., Zhang X. X., Jing X.: Processible nanomaterials with high conductivity and magnetizability: Preparation and properties of magnetite/poly aniline nanocomposites film. *Pure Application Chemistry*, **72**, 157–162 (2000).
- [18] Hussain A. M. P., Kumar A.: Electrochemical synthesis and characterization of chloride doped polyaniline. *Bulletin of Material Science*, **26**, 329–334 (2003).
- [19] Ibrahim M., Koglin E.: Spectroscopic study of polyaniline emeraldine base: Modelling approach. *Acta Chimica Slovenica*, **52**, 159–163 (2005).
- [20] Liu G., Freund M. S.: New approach for the controlled crosslinking of polyaniline: Synthesis and characterization. *Macromolecules*, **30**, 5660–5665 (1997).
- [21] Oh K. W., Kim S. H., Kim E. A.: Improved surface characteristic and the conductivity of polyaniline-nylon fabrics by plasma treatment. *Journal of Applied Polymer Science*, **81**, 684–694 (2001).
- [22] Wang Y., Jing X.: Intrinsically conducting polymers for electromagnetic interference shielding. *Polymer for Advanced Technologies*, **16**, 344–351 (2005).
- [23] da Silva P. J. E., Temperini M. L. A., Torresi S. I. C.: Characterization of conducting polyaniline blends by resonance. *Journal of Brazil Chemical Society*, **16**, 322–327 (2005).
- [24] Plesu N., Hiescu S., Ilia G., Popa A., Muntean C.: Rheology of polyaniline aispersims in acrylic resin. *Turkey Journal of Chemistry*, **30**, 155–163 (2006).
- [25] Draman S. F. S., Daik R., Ahmad M.: Fluorescence characteristics of sulfonated polyaniline solution in DMF when exposed to oxygen gas. *Malaysian Journal of Chemistry*, **8**, 37–44 (2006).
- [26] Steyskal J., Gilberg, K. G.: Polyaniline, preparation of a conducting polymer (IUPAC Technical Report). *Pure and Applied Chemistry*, **74**, 857–867 (2002).
- [27] Vilènik M., igon M., Zupan M., Šebenik A.: Influence of polymerization parameters in the molecular weight of polyaniline. *Acta Chimica Slovenica*, **45**, 173–183 (1998).
- [28] Li D., Kaner R. B.: Shape and aggregation control of nanoparticles: Not shaken not stirred. *Journal of American Chemical Society*, **128**, 968–975 (2006).
- [29] Pérez R., Pinto N. J.: Electrical characterization of polyaniline synthesized using one phase emulsion polymerization process. in 'Proceeding of the National Conference on Undergraduate Research (NCUR) 2004, Indianapolis, USA' 15–17 (2004).

- [30] Arsalani N., Khavei M., Entezanai A. A.: Synthesis and characterization of novel-N-substituted polyaniline by Triton X-100. *Iranian Polymer Journal*, **12**, 237–242 (2003).
- [31] Gaikwad P. D., Shirale D. J., Gade V. K., Savale P. A., Kharat H. J., Kakde K. P., Hussaini S. S., Dhumane N. R., Shirsat M. D.: Synthesis of H₂SO₄ doped polyaniline film by potentiometric method. *Bulletin of Material Science*, **29**, 169–172 (2006).
- [32] Mallick K., Witcomb M. J., Binsmore A., Scurrill M. S.: Polymerization of aniline by cupric sulfate: A facile synthetic route for producing polyaniline. *Journal of Polymer Research*, **13**, 397–401 (2006).
- [33] Nestorovic G. D., Jeremic K. B., Jovanovic S. M.: Kinetics of aniline polymerization initiated with Iron III chloride. *Journal of Serbian Chemical Society*, **71**, 895–904 (2006).
- [34] Gupta V., Miura N.: Electrochemically deposited polyanilins network: A high performance electrode materials for redox super capacitors. *Electrochemical and Solid State Letters*, **8**, A630–A632 (2005).
- [35] Mazur M., Tagowska M., Palys B., Jackowska K.: Template synthesis of poly aniline and poly(2-methoxy aniline) nanotubes: Comparison of the formation mechanism. *Electrochemistry Communications*, **5**, 403–407 (2003).
- [36] Dispenza C., Lo Presti C., Belfione C., Spadaro G., Piazza S.: Electrically conductive hydrogel composites made of polyaniline nanoparticles and poly(N-vinyl-2-pyrrolidone). *Polymer*, **47**, 961–971 (2006).
- [37] Savitha P., Swapna Rao P., Sathyanarayana D. N.: Highly conductive new aniline copolymers: poly(aniline-co-amino acetophenone)s. *Polymer International*, **54**, 1243–1250 (2005).
- [38] Pant H. C., Patra M. K., Negi S. C., Bhatia A., Vadera S. R., Kumar, N.: Studies on conductivity and dielectric properties of polyaniline-zinc sulphide composites. *Bulletin of Material Science*, **29**, 379–384 (2006).
- [39] Shantala P., Raghavendra S. D. P., Revansiddappa S., Narsimha P., Ambika Prasad M.: Synthesis, transport and dielectric properties of polyaniline/ Co₃O₄ composites. *Bulletin of Material Science*, **30**, 89–92 (2007).
- [40] Lee K. S., Blanchet G. B., Gao F., Loo Y-L.: Direct patterning of conductive water-soluble polyaniline for thin film organic electrodes. *Applied Physics Letters*, **86**, 076102/1–076102/3 (2005).
- [41] Pud A., Ogurtsov N., Korzhenko A., Shapoval G.: Some aspects of preparation methods and properties of polyaniline blends and composites with organic polymers. *Program Polymer Science*, **28**, 1701–1753 (2003).
- [42] Shukla S., Bajpai A. K.: Preparation and characterization of highly swelling smart grafted polymer networks of poly (vinyl alcohol) and poly (acrylic acid-co-acrylamide). *Journal Applied Polymer Science*, **102**, 84–95(2006).
- [43] Bajpai A. K., Mishra A.: Preparation and characterization of tetracycline-loaded interpenetrating polymer networks of carboxymethyl cellulose and poly (acrylic acid): Water sorption and drug release study. *Polymer International*, **54**, 1347–1356 (2005).
- [44] Bajpai A. K., Saini R.: Preparation and characterization of biocompatible spongy cryogels of poly (vinyl alcohol)-gelatin and study of water sorption behaviour. *Polymer International*, **54**, 1233–1242 (2005).

Improvement in electrical, thermal and mechanical properties of epoxy by filling carbon nanotube

Y. X. Zhou^{1,*}, P. X. Wu², Z-Y. Cheng², J. Ingram¹, S. Jeelani¹

¹Tuskegee University's Center for Advanced Materials (T-CAM), Tuskegee, AL 36088, USA

²Materials Research and Education Center, Auburn University, Auburn, AL 36849, USA

Received 22 September 2007; accepted in revised form 7 November 2007

Abstract. In this study, electrical, thermal and mechanical properties of multi-walled carbon nanotubes (CNTs) reinforced Epon 862 epoxy have been evaluated. Firstly, 0.1, 0.2, 0.3, and 0.4 wt% CNT were infused into epoxy through a high intensity ultrasonic liquid processor and then mixed with EpiCure curing agent *W* using a high speed mechanical agitator. Electric conductivity, dynamic mechanical analysis (DMA), three point bending tests and fracture tests were then performed on unfilled, CNT-filled epoxy to identify the loading effect on the properties of materials. Experimental results show significant improvement in electric conductivity. The resistivity of epoxy decreased from 10^{14} $\Omega\cdot\text{m}$ of neat epoxy to 10 $\Omega\cdot\text{m}$ with 0.4% CNT. The experimental results also indicate that the frequency dependent behavior of CNT/epoxy nanocomposite can be modeled by *R-C* circuit, permittivity of material increase with increasing of CNT content. DMA studies revealed that filling the carbon nanotube into epoxy can produce a 90% enhancement in storage modulus and a 17°C increase in T_g . Mechanical test results showed that modulus increased with higher CNT loading percentages, but the 0.3 wt% CNT-infusion system showed the maximum strength and fracture toughness enhancement. The decrease in strength and fracture toughness in 0.4% CNT/epoxy was attributed to poor dispersions of nanotubes in the composite.

Keywords: nanocomposites, carbon nanotubes, epoxy resin, electric-thermal-mechanical properties

1. Introduction

Epoxy resin is the polymer matrix used most often with reinforcing fibers for advanced composites applications. The resins of this class have good stiffness, specific strength, dimensional stability, and chemical resistance, and show considerable adhesion to the embedded fiber. Over the years, many attempts have been made to modify epoxy by adding either rubber particles [1–2] or fillers [3–4] to improve the matrix-dominated composite properties. The addition of rubber particles improves the fracture toughness of epoxy, but decreases its modulus and strength. The addition of fillers, on the other hand, improves the modulus and strength of epoxy, but decreases its fracture toughness. The

heat deflection temperature of epoxy is also improved by the addition of fillers. In recent years, nanosized fillers such as nanoparticles, nanotubes, clay and nanofibers have been considered as filler material for epoxy to produce high performance composites with enhanced properties [5–10].

Carbon nanotubes are excellent candidates for multi-functional nano-reinforcing a variety of polymer matrices because of their high strength (~100 times stronger than steel) and modulus (about 1 TPa), high thermal conductivity (about twice as high as diamond), excellent electrical capacity (1000 times higher than copper), and thermal stability (2800°C in vacuum) [11]. Nanophased matrices based on polymers and carbon nanotubes have

*Corresponding author, e-mail: yzhou@tuskegee.edu
© BME-PT and GTE

attracted great interest because they frequently include superior mechanical, electronic, and flame-retardant properties. Different polymer/CNT nanocomposites have been synthesized by incorporating CNTs into various polymer matrices, such as polyamides [12], polyimides [13–15], epoxy [16], polyurethane [17, 18] and polypropylene [19–21]. Previous results indicated that the addition of small amounts of CNT (<1 wt%) to a matrix system can increase electric, thermal and mechanical properties without compromising the weight or processability of the composite. These polymer-based nanocomposites derive their high properties, particularly mechanical properties, at low filler volume fractions owing to the high aspect ratio and high surface area to volume ratio of the nano-sized particles. According to Reynaud *et al.* [22], an interface of 1 nm thick represents roughly 0.3% of the total volume of polymer in case of micro particle filled composites, whereas it can reach 30% of the total volume in case of nanocomposites. However, high specific surface area causes strong tendency to agglomerate, which reduces the strength of nanocomposite by stress concentration effect. When dispersing conductive CNT in polymer matrix, it is important to keep the filler volume (or weight) fraction below a certain value to maintain the strength and fracture toughness. Optimal loading of CNT in matrix is key parameter to develop multi-functional nanophased composite.

The purpose of this paper is to show the effect of carbon nanotubes loading on the electronic, thermal and mechanical properties of epoxy. An ultrasonicator was used to process the CNT-epoxy nanocomposite. Dynamic Mechanical Analysis (DMA) was performed to evaluate thermal performances. Flexural tests and fracture test were performed to evaluate mechanical performances. Microscopic

approaches were used to investigate the dispersion of CNT and material's failure mechanisms.

2. Material processing

The epoxy used was Part A: Epon 862 (bisphenol F epoxy) and Part B: EpiCure curing agent W, both purchased from Miller-Stephenson Chemical Company, Inc. Carbon Nanotechnologies, Inc. produced the multi-walled carbon nanotubes (purity > 95%) used in this study. The tube diameter ranges from 30 to 50 nm, the tube length ranges from 3 to μm . The weight fraction of the carbon nanotubes ranged from 0 to 0.4 wt%, to help identify the loading with the best thermal and mechanical properties.

Figure 1 shows the pictures of received carbon nanotubes at different magnifications. High specific surface area and cotton-like entanglements caused the formation of agglomerates [16]. Agglomerates of CNTs, called nanoropes, are difficult to separate and infiltrate with the matrix. For polymer matrix nanocomposites, high power dispersion methods, such as ultrasound and high-speed shearing, are the simplest and most convenient to improve the dispersion of nanosized fillers in a polymer matrix [15, 16]. In this study, the components were mixed using a high-intensity ultrasonic processor. In this case, the application of alternating acoustic pressure above the cavitation threshold creates numerous cavities in the liquid. Some of these cavities oscillate at a frequency of the applied field (usually 20 kHz) whereas the gas content inside these cavities remains constant. However, some other cavities grow intensely under tensile stresses whereas yet another portion of these cavities that are not completely filled with gas start to collapse under the compression stresses of the sound wave. In the latter case, the collapsing cavity generates tiny par-

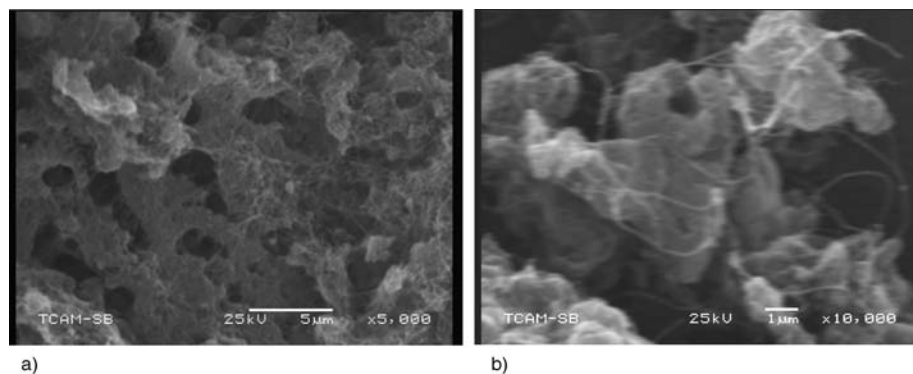


Figure 1. SEM pictures of as received carbon nanotube at different magnification

ticles of debris and the energy of the collapsed one is transformed into pressure pulses. It is noteworthy that the formation of the debris further facilitates the development of cavitation. It is assumed that acoustic cavitation in liquids develops according to a chain reaction. Therefore, individual cavities on real nuclei develop so rapidly that within a few microseconds an active cavitation region is created close to the source of the ultrasound probe. The development of cavitation processes in the ultrasonically processed melt creates favorable conditions for the intensification of various physico-chemical processes. Acoustic cavitation accelerates heat and mass transfer processes such as diffusion, wetting, dissolution, dispersion, and emulsification. The uniform dispersion of CNF was observed in sonication process [8].

Pre-calculated amounts of carbon nanotubes and Epon 862 resin were carefully weighed and mixed together in a beaker. A high-intensity, ultrasonic irradiation mixed the CNTs and resin for an hour on pulse mode, 50 sec on/25 sec off (Ti-horn, 20 kHz Sonics Vibra Cell, Sonics & Materials, Inc). The beaker containing the mixture was submerged in an ice bath to keep it cool during the sonication process. Once the irradiation was complete, Epi-Cure curing agent *W* was added to the modified resin and mixed using a high-speed mechanical stirrer for about 10 minutes. The mix ratio of Epon 862 and *W* agent was 100:26. The mixing of epoxy and curing agent initially produced highly reactive, volatile vapor bubbles, which could create voids and detrimentally affect the properties of the final product. To reduce the chance of voids, the liquid was preheated to 80°C to reduce its viscosity and a high vacuum system was used for about 30 minutes. After the bubbles were completely removed, the mixture was transferred to plastic- and Teflon-coated metal rectangular molds and cured for 4 hours at 120°C. The cured material was then trimmed. Finally, test samples were machined for thermal and mechanical characterization and all panels were post-cured at 170°C for 4 hours in a Lindberg/Blue Mechanical Convection Oven.

3. Experimental results and discussions

3.1. Electric properties

The electrical properties of the neat and nanophased epoxy were measured by using an Agilent 4294-A Precision Impedance analyzer. The composites were cut into rectangular bars with dimension of 8 mm × 4 mm × 1 mm (length, width and thickness) by a diamond saw. The two end surfaces were fully coated with gold as electrodes, which is about 4 mm². The measurement was carried at frequencies from 100 Hz to 10 MHz at room temperature. In the measurement, the impedance of the sample at each frequency was measured and recorded. The resistivity of the composites was calculated using the measured impedance and the geometry of the sample.

The application of conductive nano-particles to an insulating polymer matrix is supposed to induce an electrical conductivity, when the volume fraction exceeds the percolation threshold [23]. Generally, the percolation threshold is considered to be lower for fiber-shaped fillers (high aspect ratio) than for spherical particles. The results shown in Figure 2 are the resistivity of the neat and nanophased epoxy at frequency 100 Hz. In this figure, the impedance results of each material are consistent, even some samples are not very uniform. A dramatic decrease in resistivity has been found in nanophased epoxy. With only 0.2% CNT, resistivity of epoxy decreased from 10¹⁴ Ω·m of neat epoxy to 10 Ω·m.

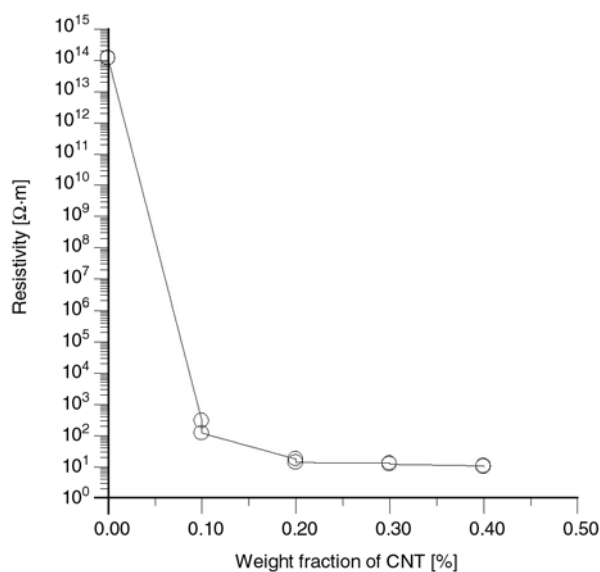


Figure 2. Effect of CNT weight fraction on resistivity of epoxy

According to Gojny’s results [23, 24], a reagglomeration of nanotubes will lead to conductive paths at lower filler contents, depending on the aspect ratio and the mobility in the matrix. The CNTs have the highest tendency to re-agglomerate under formation of conductive paths. The percolation threshold has, therefore, been determined to be below 0.1 wt%. However, once CNT loading is higher than 0.2%, resistivity decreased with CNT content slowly.

Figure 3 shows the effect of frequency on resistivity of nanophased epoxy. It is interesting that the impedance of the sample decreases significantly with frequency at frequencies higher than 100 kHz, indicating that at high frequency the impedance of the sample is dominated by the capacitance of the epoxy matrix. Therefore, it is possible to determine the connectivity between the CNT and polymer matrix by using the complex resistivity of the sample at different frequencies over a broad frequency range.

From Figure 3, the frequency dependent behavior of CNT/epoxy sample can be simulated by using R-C circuit. For R-C circuit, the impedance is given by the Equation (1):

$$Z = \frac{R}{\sqrt{1 + (2\pi f)^2 R^2 C^2}} \quad (1)$$

where R is resistance, C is the capacitor’s capacitance and f is frequency. The resistance and capacitance of rectangular bars are given by Equations (2) and (3):

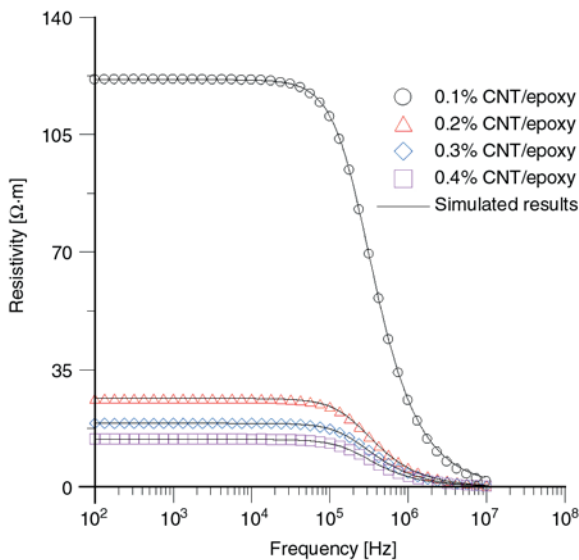


Figure 3. Resistivity vs. frequency for the composites with different concentrations

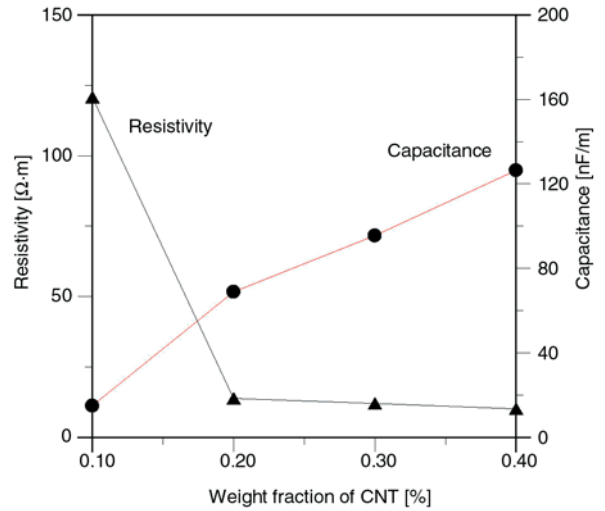


Figure 4. Effect of CNT content on electric parameters

$$R = \frac{\rho L}{WT} \quad (2)$$

$$C = \frac{\epsilon WT}{L} \quad (3)$$

where ϵ is the permittivity of the dielectric and ρ is the resistivity. Both of them are material parameters. L , W and T are length, width and thickness of sample, respectively. Substituting Equations (2) and (3) into Equation (1) and rearranging, one can obtain the Equation (4):

$$\rho^* = \frac{\rho}{\sqrt{1 - (2\pi f)^2 \rho^2 \epsilon^2}} \quad (4)$$

where ρ^* is resistivity of the composites calculated by using the measured impedance and the geometry of the sample. From experimental results and Equation (4), resistivities and permittivities of nanophased epoxy were simulated and plot them as function of CNT content (Figure 4). As we expected, resistivity decreased, and permittivity increased with increasing of CNT. The solid lines in Figure 3 shows simulated results, which agree with experimental data well.

3.2. Thermal properties

Dynamic Mechanic Analysis (DMA) was performed on a TA Instruments 2980, operating in the three-point bending mode at an oscillation frequency of 1 Hz. Data were collected from room temperature to 200°C at a scanning rate of 10°C/min. The sample specimens were cut into rec-

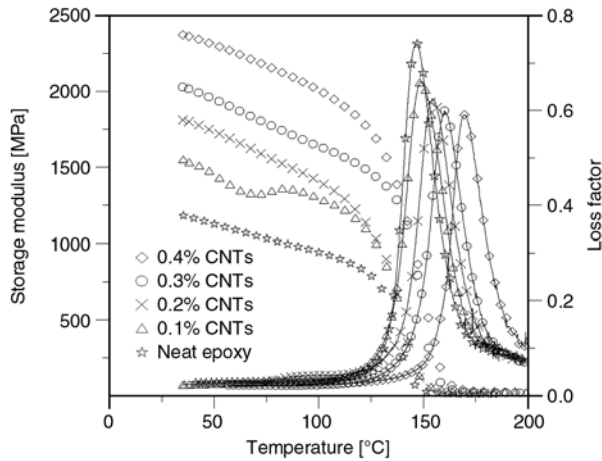


Figure 5. DMA results of neat and nanophased epoxy

tangular bars measuring 2 mm × 30 mm × 12 mm by a diamond saw.

The loss factor curve, $\tan\delta$, of the neat epoxy and its nanocomposites measured by DMA are shown in Figure 5. The peak height of loss factor decreased with higher CNT content, but the temperature determined from the peak position of $\tan\delta$, T_g , increased 17°C. In addition, the width $\tan\delta$ increased with higher CNT content. Similar results have been observed in other nanocomposites [21]. Figure 5 also shows the DMA plots of storage modulus vs. temperature as a function of loading carbon nanotubes. The storage modulus steadily increased with higher CNT weight percents. The addition of 0.4 wt% of carbon nanotube yielded a 93% increase of the storage modulus at 30°C. The high aspect ratio and elastic modulus of CNTs, as compared to nanoclay and nanoparticles [7, 8], increase the storage modulus with smaller amounts of CNTs.

Thermogravimetric Analysis (TGA) was conducted with a TA Instruments TGA2950 in nitrogen gas at a heat rate of 10°C/min, from ambient to 600°C. The TGA samples were cut into small pieces using an ISOMET Cutter and were machined using a mechanical grinder to maintain sample weights between 5–20 mg. Universal Analysis 2000-TA Instruments Inc., a data acquisition system, generated the real-time characteristic curves. All TGA tests are run in nitrogen gas. Figure 6 shows the TGA results of neat and nanophased epoxy. The normalized weights vs. temperature curves of five materials overlap. All samples started to decompose around 340°C and completely decomposed around 460°C. The derivative peaks of weight vs. temperature curves show the decomposition tem-

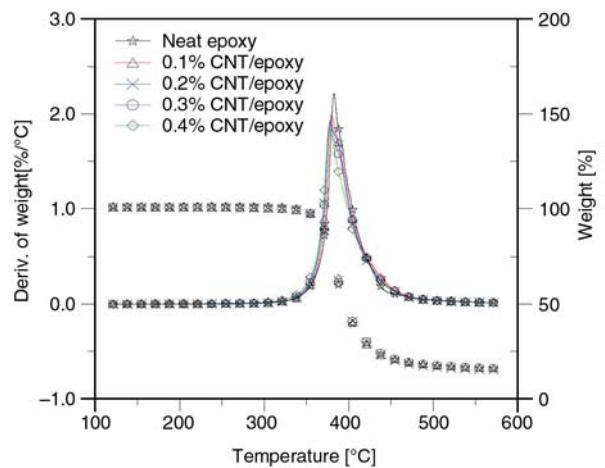


Figure 6. Normalized weight vs. temperature curves of neat and nanophased epoxy

perature. But CNT has little effect on decomposition temperature of epoxy.

3.3. Mechanical response

Flexural tests were performed according to ASTM D790-86 under a three-point bend configuration. The tests were conducted in a 10 kN servo-hydraulic testing machine equipped with a Test Ware data acquisition system. The machine was run under displacement control mode at a crosshead speed of 2.0 mm/min. All the tests were performed at room temperature. Test samples were cut from the panels using a Felker saw fitted with a diamond coated steel blade. Five replicate specimens from four different materials were prepared for static flexure tests.

Typical stress-strain behavior from the flexural tests is shown in Figure 7. All specimens failed immediately after the tensile stress reached the maximum value. The stress-strain curves showed considerable non-linearity before reaching the maximum stress, but no obvious yield point was found in the curves. Five specimens were tested for each condition; the average properties obtained from these tests are listed in Table 1.

Table 1. Mechanical properties of neat and nanophased epoxy

	Modulus [GPa]	Strength [MPa]	Failure strain [%]
Neat epoxy	2.46	93.5	4.02
0.1% CNT	2.54	109	6.06
0.2% CNT	2.60	115	6.80
0.3% CNT	2.65	121	7.58
0.4% CNT	2.75	113	5.12

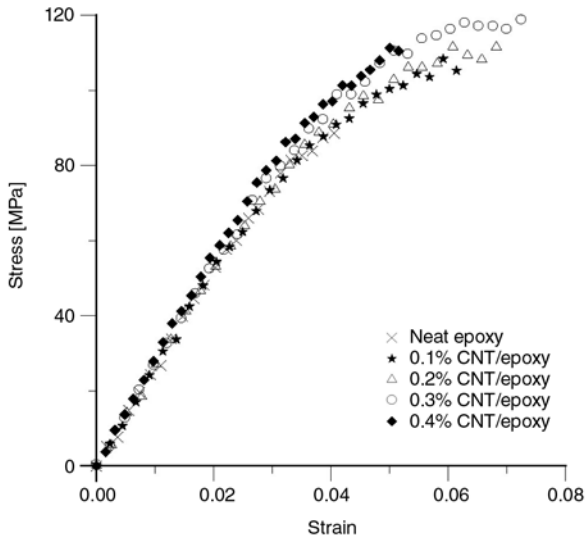


Figure 7. Stress strain curves of epoxy and CNT/epoxy

The modulus of the nanophased epoxy increases continuously with higher CNT content (Table 1, Figure 7). The tensile modulus improved by 11.7% with an addition of 0.4 wt% of CNTs. However, the system with 0.3 wt% infusion is the best, with a 28.3% strength enhancement (Table 1, Figure 7). The strength begins to decrease with 0.4 wt% loading, although the gain in modulus is maintained. See Figure 8 for the relationship between modulus, strength, and CNT weight fraction. The dispersion of CNTs that restricts the mobility of polymer chains under loading improved the modulus and strength in small loadings. The high aspect ratio, high modulus, strength of CNTs also contributed to the reinforcement. However, the decrease of strength with high CNT content can be attributed to

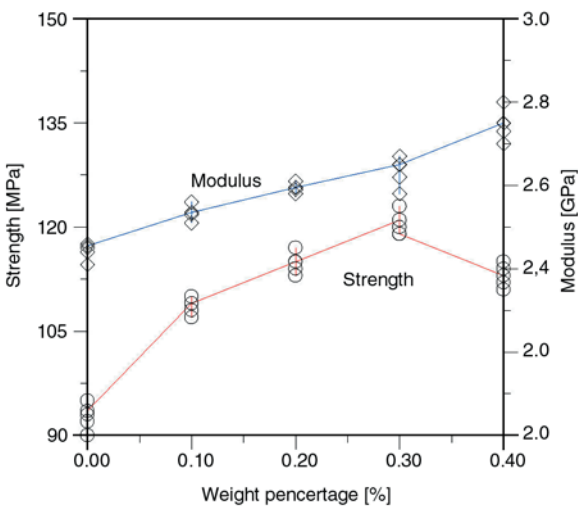


Figure 8. Effect of CNT content on strength and modulus of neat and nanophased epoxy

following two effects: First, the dispersion of CNTs is not uniform in higher loading systems. Acoustic cavitation is one of the most efficient ways to disperse nanoparticles with small loading into the pure materials. Previous results have also indicated that, using the acoustic cavitation method, the optimal loading of carbon nanofibers in epoxy is 2.0 wt% [7] and the optimal loading of SiC nanoparticles in epoxy is 1.0 wt% [6]. The other one, voids may have also decreased the strength. Choi and Gojny reported that few voids were produced during the fabrication process and that voids increased with the higher nanoparticle contents [25, 26].

Fracture toughness of neat and nanophased epoxy was determined from static three-point tests of the single edge notch specimens. Each of these specimens was cycled 100 times between 4 and 40% of the peak load at 1 Hz and then statically tested. During the static tests, the change in specimen length Δl was measured by recording the ram positions through the displacement transducer of the MTS machine.

The critical stress intensity factor, K_{Ic} , was calculated according to the Equations (5) and (6):

$$K_{Ic} = \left(\frac{P}{B} w^{3/2} \right) f(a/w) \tag{5}$$

where P – applied load on the specimen, B – specimen thickness, w – specimen width, a – crack length, and

$$f(a/w) = \frac{3\sqrt{\frac{a}{w}} \left[1.99 - \left(\frac{a}{w} \right) \left(1 - \frac{a}{w} \right) \left(2.15 - 3.93 \frac{a}{w} + 2.7 \frac{a^2}{w^2} \right) \right]}{2 \left(1 + 2 \frac{a}{w} \right) \left(1 - \frac{a}{w} \right)} \tag{6}$$

Figure 9 shows the load-displacement diagrams of neat epoxy and of 0.3 wt% CNT/epoxy. Since non-linearity was seldom observed in load-displacement diagrams, the critical stress intensity factor (K_{Ic}) of materials was calculated from the peak load of each load-displacement curve, and was plotted as a function of the CNT weight fraction (Figure 10). It shows that enhancement reaches a maximum for the critical stress intensity factor at

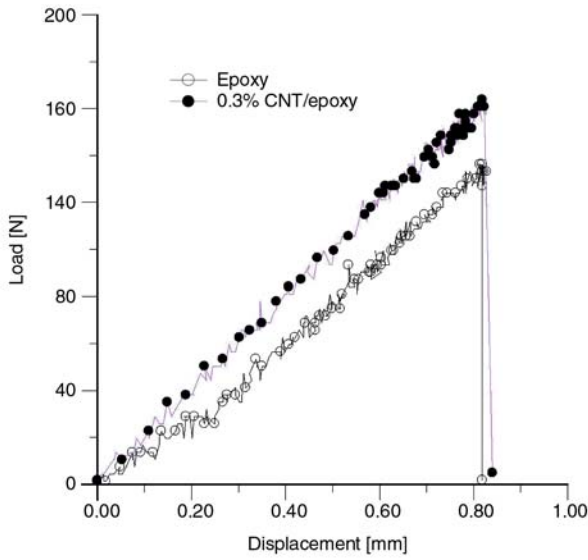


Figure 9. Load-displacement curves in fracture test

0.3 wt%. Degradation in fracture toughness was found in 0.4% system.

3.4. Fracture surface

The fracture surfaces of composites give first information about failure mechanism and influence of CNT on failure process. SEM-images were taken with a Jeol 2001 at acceleration voltages 25 kV on the fracture surfaces of the neat epoxy and its nanocomposites. The initial crack occurred at the tension edge of both the neat and nanophased specimens (Figures 11a and 11b). Neat epoxy resin

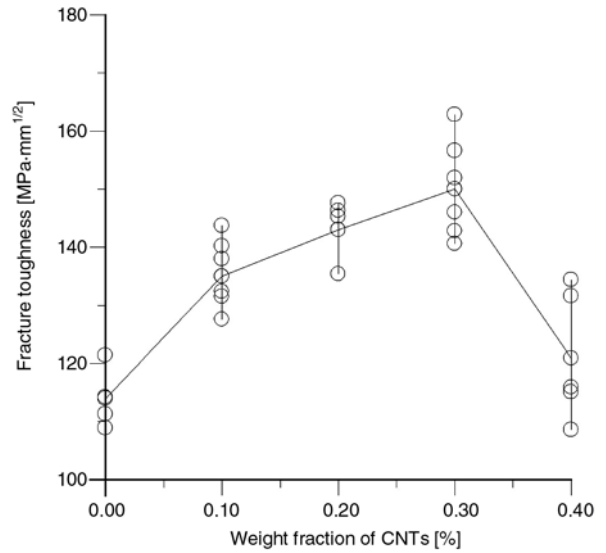


Figure 10. Effect of CNT contents on fracture toughness of epoxy

exhibits a relatively smooth fracture surface and the higher magnification SEM picture in Figure 11c indicates a typical fractography feature of brittle fracture behavior, thus accounting for the low fracture toughness of the unfilled epoxy. The distance between two cleavage steps is range from 40–100 μm and the cleavage plane between them is flat and featureless. Smooth fracture surface in neat epoxy revealed that crack propagated through specimen along the same plane. The fracture surfaces of the nanocomposites show considerably different

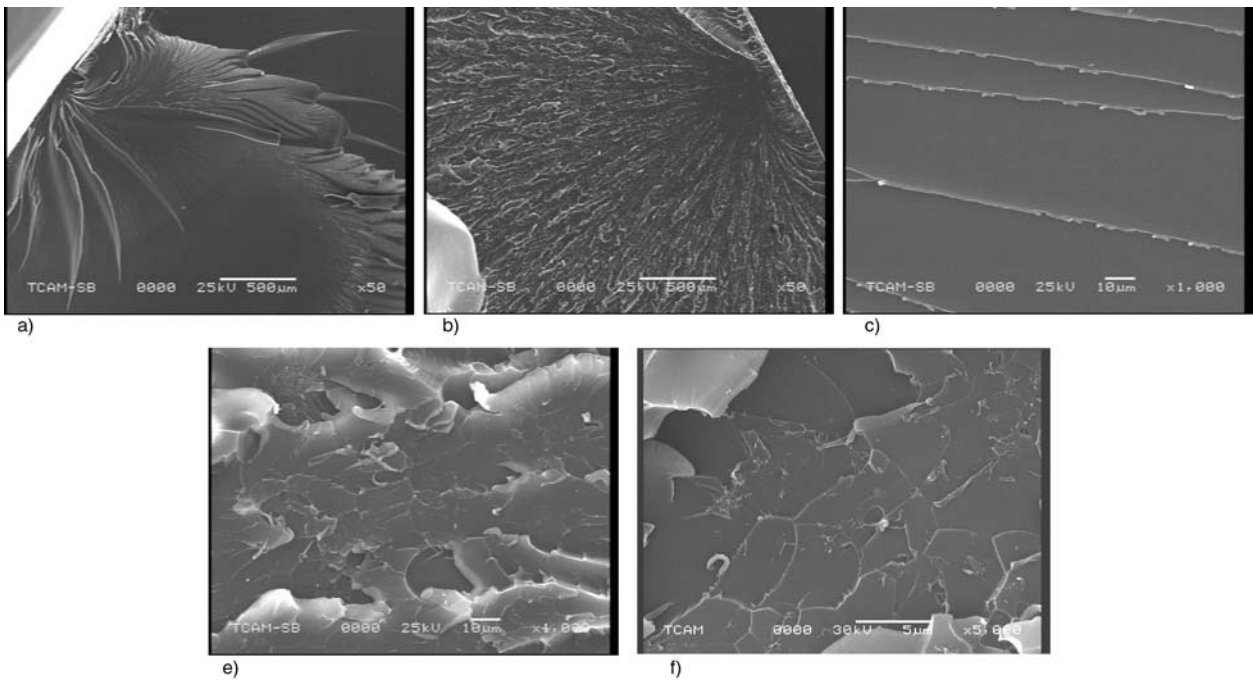


Figure 11. Fracture surface of nanophased epoxy

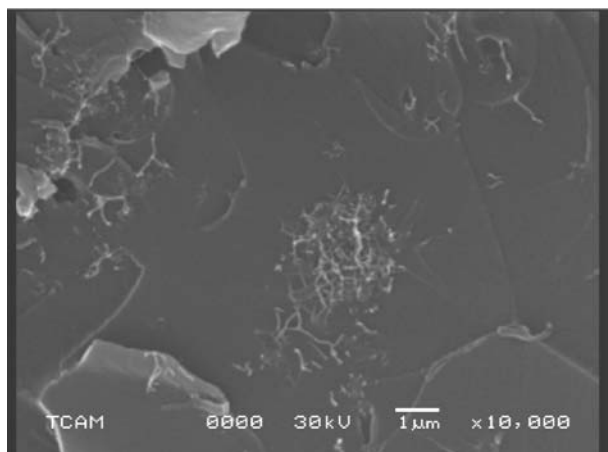


Figure 12. Fracture surface of 0.4% CNT/epoxy

fractographic features. For example, the failure surfaces of the nanocomposite are rougher with the CNTs added into the epoxy matrix (Figures 11b and 11d). The higher magnification SEM picture in Figure 11e shows that the size of the cleavage plane decreased to 10 μm after the infusion of the CNTs. The decreased cleavage plane and the increased surface roughness imply that the path of the crack tip is distorted because of the carbon nanotubes, making crack propagation more difficult. Figure 11d also shows that CNTs were uniformly dispersed in the epoxy. The flat cleavage planes were formed by the network of cleavage steps and each plane contains at least one carbon nanotube. During the failure process, the crack propagation changed direction as it crossed CNTs. The bridge effect, which prevents crack opening, increased strength in the CNT/epoxy matrix.

When the CNT content increased to 0.4 wt%, a large particle, an agglomeration of several carbon nanotubes (Figure 12), was observed in the fracture surface. At a low stress level, the agglomerated particle increased the stiffness of the material, but at a high stress level, the stress concentration caused by the agglomerated particle initiated a crack, which made the sample fail quickly.

4. Conclusions

Multi-walled carbon nanotubes have been infused in epoxy by ultrasonic method. Based on electrical, thermal and mechanical experiment results, we reached the following conclusions.

1. Ultrasonic cavitation is an efficient method of infusing carbon nanotubes into epoxy resin

when CNT weight fractions are lower than 0.3 wt%. Above the 0.3 wt%, CNTs agglomerated.

2. The frequency dependent behavior of CNT/epoxy can be described by using as a *R-C* circuit model. The resistivity of epoxy decreased with CNT content, and permittivity increased with increasing of CNT.
3. Compared to neat epoxy, DMA results indicated a 93% improvement in storage modulus in 0.4 wt% CNT/epoxy at room temperature and a 17°C increase in T_g . However, the decomposition temperature decreased with higher CNT contents.
4. Flexural modulus steadily increases with a higher CNT weight percent. Modulus improved by 11.7% with an addition of a 0.4 wt% of CNTs. Flexural strength and fracture toughness peaked in a 0.3 wt% CNT/epoxy system. The decrease in strength and fracture toughness in 0.4% CNT/epoxy was attributed to poor dispersions of nanotubes in the composite.

Acknowledgements

The authors would like to gratefully acknowledge the support of the Air Force Minority Leaders Nanocomposites Research and Education Program and National Science Foundation.

References

- [1] Imanaka M., Nakamura Y., Nishimura A., Iida T.: Fracture toughness of rubber-modified epoxy adhesives: Effect of plastic deformability of the matrix phase. *Composites Science and Technology*, **63**, 41–51 (2003).
- [2] Chikhi N., Fellahi S., Bakar M.: Modification of epoxy resin using reactive liquid (ATBN) rubber. *European Polymer Journal*, **38**, 251–264 (2002).
- [3] Xian G., Walter R., Hauptert F.: Friction and wear of epoxy/TiO₂ nanocomposites: Influence of additional short carbon fibers, Aramid and PTFE particles. *Composites Science and Technology*, **66**, 3199–3209 (2006).
- [4] Vasconcelos P. V., Lino F. J., Magalhaes A., Neto R. J. L.: Impact fracture study of epoxy-based composites with aluminium particles and milled fibres. *Journal of Materials Processing Technology*, **170**, 277–283 (2005).

- [5] Xian G. J., Walter R., Hauptert F.: Friction and wear of epoxy/TiO₂ nanocomposites: Influence of additional short carbon fibers, aramid and PTFE particles. *Composites Science and Technology*, **66**, 3199–3209 (2006).
- [6] Rodgers R. M., Mahfuz H., Rangari V. K., Chisholm N., Jeelani S.: Infusion of SiC nanoparticles into SC-15 epoxy: An investigation of thermal and mechanical response. *Macromolecular Materials and Engineering*, **290**, 423–429 (2005).
- [7] Zhou Y., Pervin F., Biswas M. A., Rangari V. K., Jeelani S.: Fabrication and characterization of montmorillonite clay-filled SC-15 epoxy. *Materials Letters*, **60**, 869–873 (2006).
- [8] Zhou Y., Farhana P., Rangari V. K., Jeelani S.: Fabrication and evaluation of carbon nano fiber filled carbon/epoxy composite. *Materials Science and Engineering, Part A: Structural Materials*, **426**, 221–228 (2006).
- [9] Abacha N., Kubouchi M., Tsuda K., Sakai T.: Performance of epoxy-nanocomposite under corrosive environment. *Express Polymer Letters*, **1**, 364–369 (2007).
- [10] Du J-H., Bai J., Cheng H-M.: The present status and key problems of carbon nanotube based polymer composites. *Express Polymer Letters*, **1**, 253–273 (2007).
- [11] Liao Y-H., Marietta-Tondin O., Liang Z-Y., Zhang C., Wang B.: Investigation of the dispersion process of SWNTs/SC-15 epoxy resin nanocomposites. *Materials Science and Engineering, Part A: Structural Materials*, **385**, 175–181 (2004).
- [12] Zhao C., Hu G., Justice R., Schaefer D. W., Zhang S., Yang M., Han C. C.: Synthesis and characterization of multi-walled carbon nanotubes reinforced polyamide 6 via in situ polymerization. *Polymer*, **46**, 5125–5132 (2005).
- [13] Kim S., Pechar T. W., Marand E.: Poly(imide siloxane) and carbon nanotube mixed matrix membranes for gas separation. *Desalination*, **192**, 330–339 (2006).
- [14] Cai H., Yan F., Xue Q.: Investigation of tribological properties of polyimide/carbon nanotube nanocomposites. *Materials Science and Engineering, Part A: Structural Materials*, **364**, 94–100 (2004).
- [15] Ogasawara T., Ishida Y., Ishikawa T., Yokota R.: Characterization of multi-walled carbon nanotube/phenylethynyl terminated polyimide composites. *Composites, Part A: Applied Science and Manufacturing*, **35**, 67–74 (2004).
- [16] Gojny F. H., Wichmann M. H. G., Fiedler B., Schulte K.: Influence of different carbon nanotubes on the mechanical properties of epoxy matrix composites-A comparative study. *Composites Science and Technology*, **65**, 2300–2313 (2005).
- [17] Koerner H., Liu W., Alexander M., Mirau P., Dowty H., Vaia R. A.: Deformation-morphology correlations in electrically conductive carbon nanotube-Thermoplastic polyurethane nanocomposites. *Polymer*, **46**, 4405–4420 (2005).
- [18] Kuan H-C., Ma C-C. M., Chang W-P., Yuen S-M., Wu H-H., Lee T-M.: Synthesis, thermal, mechanical and rheological properties of multiwall carbon nanotube/waterborne polyurethane nanocomposite. *Composites Science and Technology*, **65**, 1703–1710 (2005).
- [19] Seo M-K., Park S-J.: Electrical resistivity and rheological behaviors of carbon nanotubes-filled polypropylene composites. *Chemical Physics Letters*, **395**, 44–48 (2004).
- [20] Li C., Liang T., Lu W., Tang C., Hu X., Cao M., Liang J.: Improving the antistatic ability of polypropylene fibers by inner antistatic agent filled with carbon nanotubes. *Composites Science and Technology*, **64**, 2089–2096 (2004).
- [21] Seo M. K., Lee J. R., Park S. J.: Crystallization kinetics and interfacial behaviors of polypropylene composites reinforced with multi-walled carbon nanotubes. *Materials Science and Engineering: A*, **404**, 79–84 (2005).
- [22] Reynaud E., Gauthier C. Perez J.: Nanophases in polymers. *Review Metallurgie*, **96**, 169–176 (1999).
- [23] Gojny F. H., Wichmann M. H. G., Fiedler B., Bauhofer W., Schulte K.: Influence of nano-modification on the mechanical and electrical properties of conventional fibre-reinforced composites. *Composites, Part A: Applied Science and Manufacturing*, **36**, 1525–1535 (2005).
- [24] Gojny F. H., Wichmann M. H. G., Fiedler B., Kinloch I. A., Bauhofer W., Windle A. H., Schulte K.: Evaluation and identification of electrical and thermal conduction mechanisms in carbon nanotube/epoxy composites. *Polymer*, **47**, 2036–2045 (2006).
- [25] Choi Y-K., Sugimoto K-I., Song S-M., Gotoh Y., Ohkoshi Y., Endo M.: Mechanical and physical properties of epoxy composites reinforced by vapor grown carbon nanofibers. *Carbon*, **43**, 2199–2208 (2005).
- [26] Gojny F. H., Schulte K.: Functionalisation effect on the thermo-mechanical behaviour of multi-wall carbon nanotube/epoxy-composites. *Composites Science and Technology*, **64**, 2303–2308 (2004).

Development of structure and properties during thermal calendering of polylactic acid (PLA) fiber webs

G. S. Bhat*, P. Gulgunje, K. Desai

Department of Materials Science and Engineering, 434, Daugherty Hall, The University of Tennessee, Knoxville, TN 37996, USA

Received 4 August 2007; accepted in revised form 8 November 2007

Abstract. Due to its thermoplastic and biodegradable nature, poly(lactic acid) (PLA) holds good promise in its increasing use in the form of fibers for medical, agricultural, apparel, upholstery, hygiene, and other applications. Most of the research being done on PLA fibers is to understand their production by melt spinning, solution spinning, and the structure-property relationships during fiber formation. Nonwovens are one of the important forms of the materials into which PLA polymer can be converted to create many useful products. Thermal bonding is the most widely used bonding technique employed to impart strength, and other useful characteristics to the nonwovens. However, there is limited research done to study the behavior of PLA fibers during thermal bonding of nonwovens. Hence the research was carried out to investigate the thermal bonding of nonwovens made from PLA staple fibers. The PLA fibers were carded and then calendered at different temperatures. The webs were characterized for their structure and properties. The observed results are discussed with respect to the investigated processing conditions.

Keywords: thermal properties, mechanical properties, PLA fiber, thermal calendering

1. Introduction

With ever increasing use of synthetic polymeric fibers, and their adverse impact on the environment, degradation behavior of the polymer at the end of the life cycle is gaining more importance. This is where the conventional polymers such as polyethylene terephthalate (PET), nylon, and polypropylene used for fiber manufacture have negative impact on the environment since these polymers are not biodegradable. The availability of landfills is becoming scarce due to the increasingly large amounts of waste that is being dumped. The incinerator emissions are also of growing concern in the era of global warming. One of the ways to reduce the negative impact on the environment and keeping the earth greener for longer time is by recycling these products that would otherwise go into landfills. Recycling is easier said than done due to

the cost and quality implications involved with many nonwoven products. Under these circumstances, biodegradable polymers hold good promise in various applications so that at the end of the products' life cycle, they will degrade on their own with no harm to the environment. The biodegradable polymers break down in physiological environments by macromolecular chain scission into smaller fragments, and finally into simple stable end-products [1].

Today, a variety of biodegradable polymers are available in the market, both natural and synthetic, such as polysaccharides, proteins, polycaprolactone (PCL), polyhydroxybutyrate-valerate (PHBV) and polyesters such as PLA. PLA is one of the most promising biodegradable polymers due to its good mechanical properties that stem from L-lactic acid, thermoplastic processability, biocompatibility and

*Corresponding author, e-mail: gghat@utk.edu
© BME-PT and GTE

biodegradability. In most applications, it exhibits very good durability as compared to some of the other biodegradable polymers [2]. Compared to PET, it crystallizes faster and to a greater extent. By controlling the isomer content i. e. L-form, D-form and Meso form in the polymer, relatively wider range of properties can be obtained in the fibers. Extensive review of PLA fibers was carried out by Gupta *et al.* [3] covering fiber manufacturing methods, properties development, and various applications. The review elucidates the point that much of the research is confined to fiber manufacture and its properties development. The limited research published on nonwovens processing of PLA fiber includes melt blown nonwovens made out of PLA polymer by Khan *et al.* [4], manufacture of PLA nonwoven fabrics using CO₂ laser thinning method by Akaoka and Suzuki [5], and preparation of cellulosic nonwoven based composites made from PLA staple fibers by Kamath *et al.* [6]. A review published by Dharmadhikary *et al.* [7] discusses thermal bonding of nonwoven fabrics from several fibers. However, there is no report on the behavior of PLA fibers into nonwoven processes, especially during thermal bonding. Bhat *et al.* [8] have shown the importance of thermal bonding process variables in the development of structure-properties in the nonwovens made from polypropylene fibers. Since thermal bonding process is very important in the production of nonwovens, this study was conducted to understand the behavior of PLA fibers during thermal bonding. The main objective of this research was to investigate the effect of bonding temperature during thermal calendaring on the structure and properties of PLA nonwoven webs.

2. Experimental details

2.1. Materials and processing

PLA staple fibers were provided by Fiber Innovations Technology (FIT), Johnson City, TN. The fibers were converted to nonwoven webs using the laboratory model SDS Atlas carding machine. The schematic of the carding machine is shown in Figure 1. Weighed amount of PLA staple fibers was fed to the feed section of the carding machine to produce the webs with basis weight of approximately 35 grams per square meter (gsm). Sequences

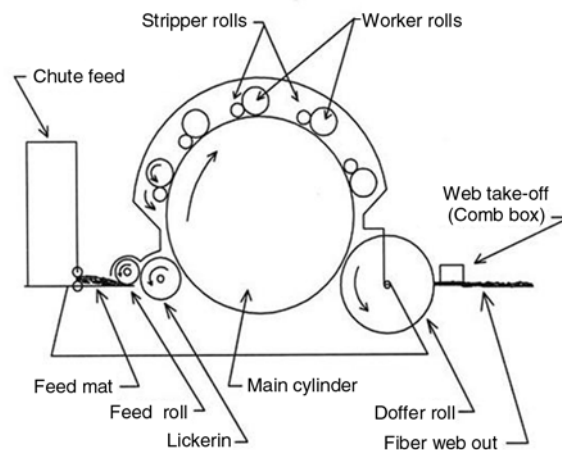


Figure 1. Schematic of the carding machine [9]

of rollers located in the machine individualize the fibers and lay them parallel in the machine direction. The continuous web of fibers coming out of the doffer was made to roll on the rotating drum. When all the material fed was deposited onto the drum completely, the card was stopped and the web was cut. Several webs of 120 cm × 30 cm dimension were thus produced, each with a basis weight of 35 gsm and used for thermal calendaring. The carded webs were thermally bonded at series of temperatures above the glass transition temperature and below the melting point of the fibers. The calender rolls speed and pressure were kept constant throughout the experiment. The schematic of the thermal bonding process consisting of a pair of rollers, which are heated to required temperature, through which nonwoven web is passed under desired pressure is shown in Figure 2. The bottom roll is smooth and the top roll is embossed with diamond patterns. Besides the bonding temperature and pressure, the raised patterns on the top rolls

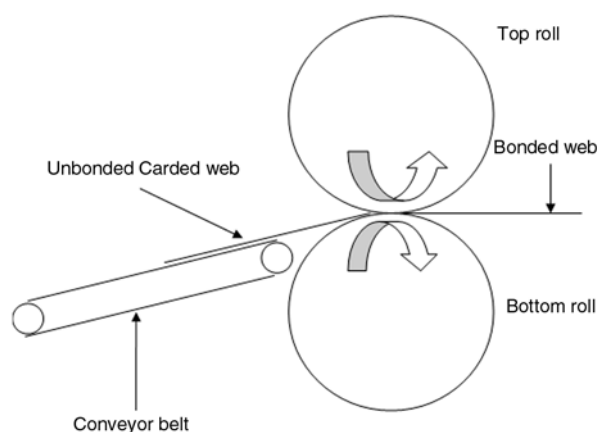


Figure 2. Schematic of the thermal calendaring

determine the degree of bonding. Five different calender roll temperatures 130, 137, 140, 145 and 150°C were used, and the calendar speed and pressure were maintained at the same value for all the samples.

2.2. Characterization

Fibers were characterized for tensile and thermal properties. Tensile properties were determined using the Thwing Albert tensile tester with a load cell of capacity 2 kg. Five samples, each as a bundle of 10 fibers, were tested and average of the five readings is reported. Young's modulus was calculated at 5% extension. The gauge length was 25 mm and the test speed was 300 mm/min.

Melting temperature and percent crystallinity of the original fibers and webs were determined using the Mettler DSC at a heating rate of 10°C/min. Heat of fusion for 100% crystalline PLA polymer was taken as 93.7 J/gm [10] for estimating the crystallinity of the samples.

The calendered webs were characterized for various properties such as basis weight, thickness using the ASTM standard D5729-97 [11], thermal analysis by DSC, tensile strength and elongation using the ASTM standard D5035-95 [12], air permeability using the ASTM standard D737-96 [13], tear strength using the ASTM standard D5734-95 [14], optical micrographs and photographs by scanning electron microscopy (SEM).

3. Results and discussion

3.1. Fiber properties

The fiber properties are listed in Table 1. The melting temperature of PLA fiber was determined to be

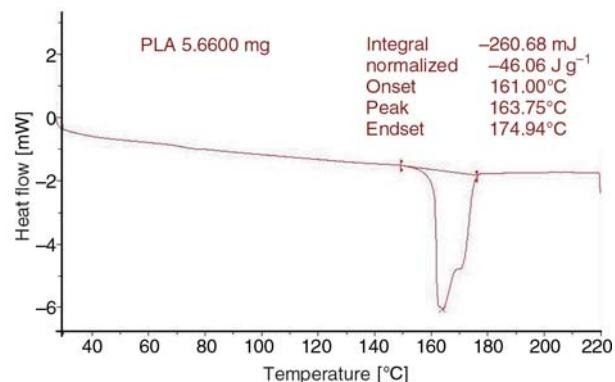


Figure 3. DSC thermogram of original PLA fiber

Table 1. PLA fiber properties

Fiber property	value
Denier [den]	3
Staple length [mm]	76
Tensile strength [gm/den]	2.8
Peak elongation [%]	64.35
Young's modulus [gm/den] (at 5% extension)	31.07
Melting temperature [°C]	164

around 164°C (Figure 3). Hence the calendaring temperatures were chosen to be below 164°C. The original fiber crystallinity as determined by DSC was around 53.3%.

3.2. Web properties

The basis weights of the webs were found to be around 40 gsm. The change in web thickness against calendaring temperature is as shown in Figure 4. As the calendaring temperature was increased, the thickness of the webs showed a decreasing trend. At constant calendaring pressure and constant calender speed, higher roll temperature lead to better compaction of the web and hence decrease in nonwoven web thickness. This is evident from the optical micrographs shown in Figure 5 which were taken at the same magnification for all the webs. At lower calendaring temperatures, the bond point appeared to be hazy due to the inability to focus on the entire thicker bond point simultaneously. With increase in calendaring temperature, the picture of bond point became more clear over the entire bond point.

3.3. Thermal properties

DSC study was done to analyse the effect of bonding temperature on the degree of crystallinity

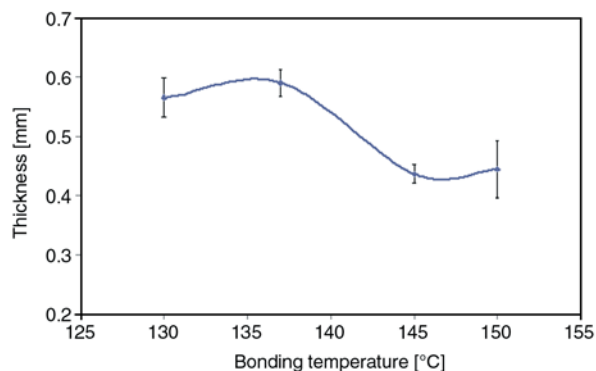


Figure 4. Thickness of the calendered PLA webs

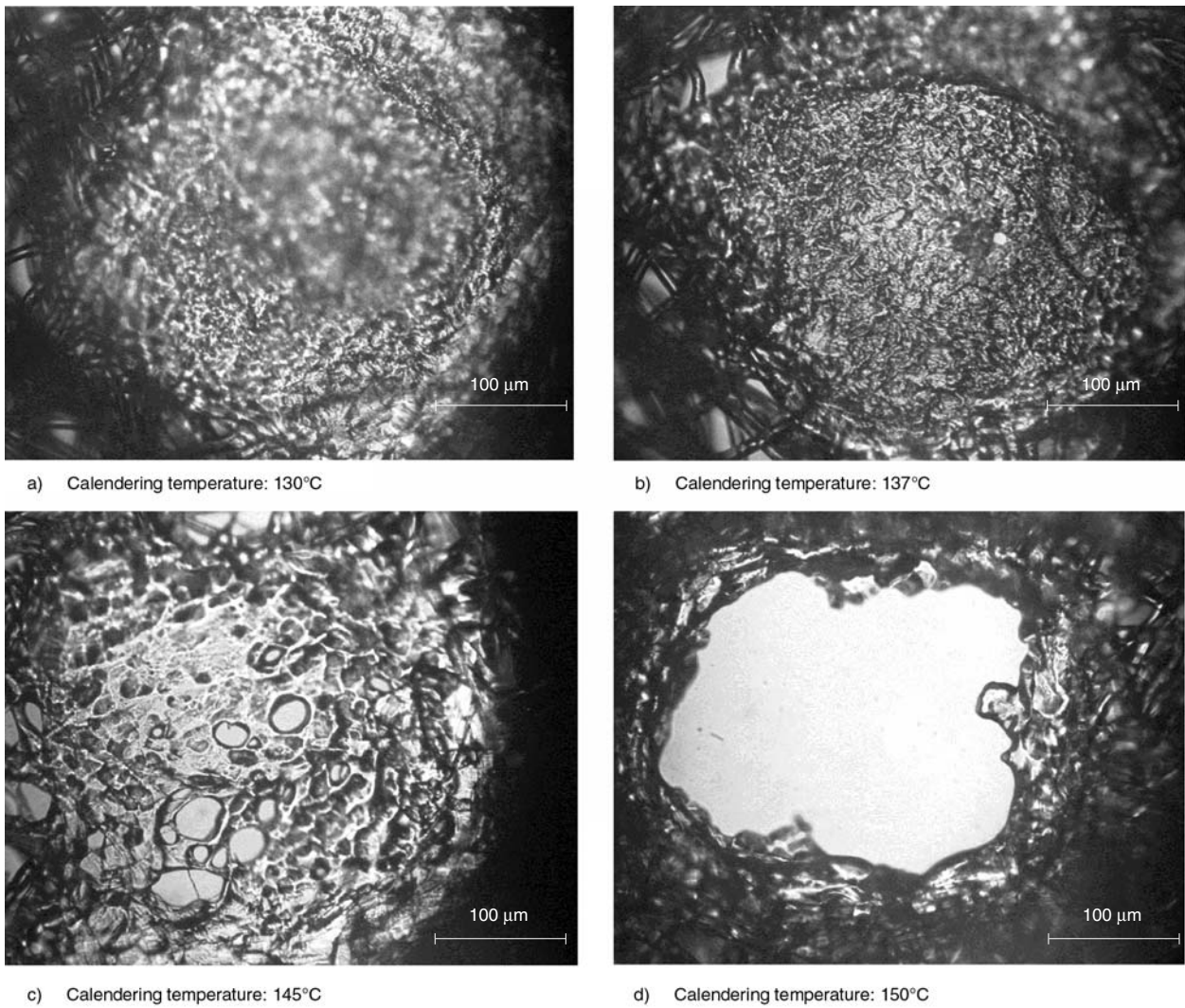


Figure 5. Optical Micrographs of the calendered PLA webs at the bond points

developed in the fibers after thermal calendering and is depicted in Figure 6. The crystallinity of the fibers before thermal calendering was 53.3%. Upon thermal calendering, crystallinity was lower than that in the fiber before calendering for all the bonding temperatures. Similar observations have been reported by Chand *et al.* [15] on thermal bonding of polypropylene webs. They had observed that the crystallinity of the polypropylene webs was increasing if the initial fiber crystallinity was lower and decreasing if the starting fiber crystallinity was very high. Obviously PLA fibers have high crystallinity before calendering and hence during calendering there is reduction in crystallinity due to partial melting and recrystallization in the unoriented conditions. Further there appears to be a decrease in crystallinity with increase in calendering temperature. Mezghani *et al.* [16] reported that

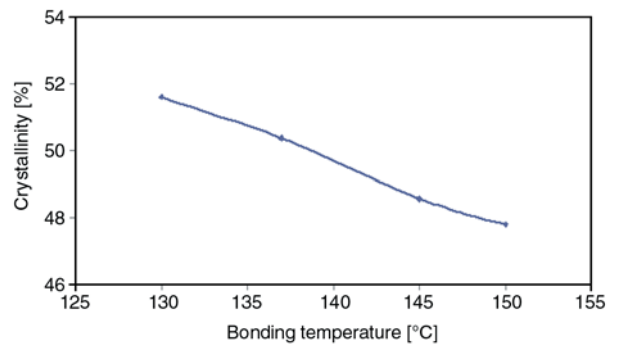


Figure 6. DSC crystallinity vs. calendering temperature of the calendered PLA webs

in the absence of molecular orientation in the melt, the crystallization kinetics of PLA become so slow that the polymer develops amorphous structure. In the present study, at various bonding temperatures, the molecular chains might have tried to relax upon partial melting. As is evident from the optical

micrographs in Figure 5, at higher calendering temperatures holes are apparent in the bond point region, most probably due to relaxation within the fibers, and further shrinkage of the webs. Such stress relaxation might have led to the loss of some of the orientation present in the original fibers and thereby slowing the crystallization kinetics leading to decrease in crystallinity with calendering temperature.

3.4. Tensile properties

The tensile strength of bonded webs was found to increase with increase in calendering temperature with the maximum at 145°C calendering temperature. The tensile strength increased sharply between 137 and 145°C (Figure 7) and above 145°C, the strength started dropping. This behavior shows that 145°C is the optimum calendering temperature for PLA under the given processing conditions. The tensile strength was higher in the machine direction (MD) than in the cross direction (CD) due to better fiber orientation in the web along the MD. The thickness data and the optical micrographs suggest that at lower calendering temperatures the web compaction at the bond point is not good, and exhibits poor bond integrity and tensile strength. With increase in calendering temperature, the bond point compactness was found to be improving, with better bond integrity, leading to increase in tensile strength. Further, optical micrographs clearly indicate that at a bonding temperature of 150°C, the bond quality is very poor. At this temperature, most of the fibers in the bond region were seen to be melted, and due to the stress relaxation by these fibers, the webs shrunk towards the edge of the bond point, creating hole in the bond region. This observation implied that beyond 145°C, over-bond-

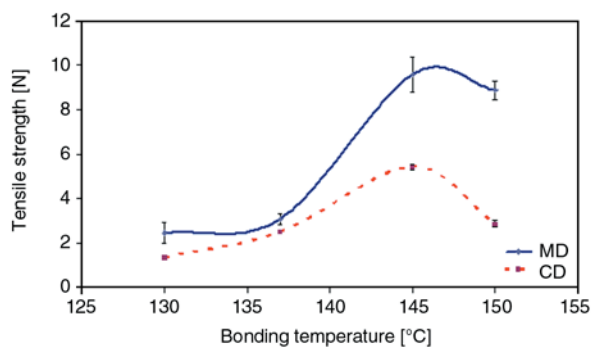


Figure 7. Tensile strength vs. calendering temperature of the calendered PLA webs

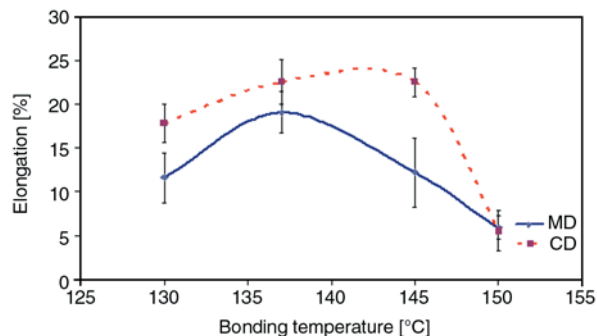


Figure 8. Elongation vs. calendering temperature of the calendered PLA webs

ing occurred and led to drop in tensile strength. Of course, the optimum bonding temperature will be shifted slightly, when calendar speed is altered due to change in residence time. Such optimum calendering temperature was also reported for thermally bonded polypropylene nonwovens produced through spun bonding process by Bhat et al. [17]. It has been shown that the calendering pressure has a minimum effect above the minimal value [18]. Referring to Figure 8, peak elongation showed a slight increase, and then a decreasing trend with increasing bonding temperature. This is because with increase in bonding temperature, the bond points became stiffer reducing the web elongation. Elongation was found to be higher in the CD than in the MD for the same reasons discussed above for tensile strength.

3.5. Tear strength

The tear strength of the bonded webs in the MD (Figure 9), improved with increasing calendering temperatures reaching its maximum at 145°C. At 150°C, the tear strength values were much lower indicating 145°C as the optimum calendering tem-

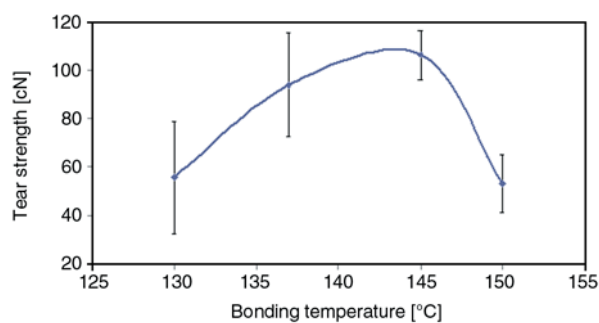


Figure 9. Tear strength vs. calendering temperature of the calendered PLA webs

perature. Comparing Figure 9 with Figure 7, it is seen that tear strength results correlate with the tensile strength results. Such a correlation between tear strength and tensile strength results has been reported by Bhat *et al.* [8] in thermal bonding of polypropylene spunbonded webs. Improved bond integrity up to 145°C and over bonding at 150°C as discussed in above section, might be associated with the observed behavior of web tear strength with respect to bonding temperature. Primentas

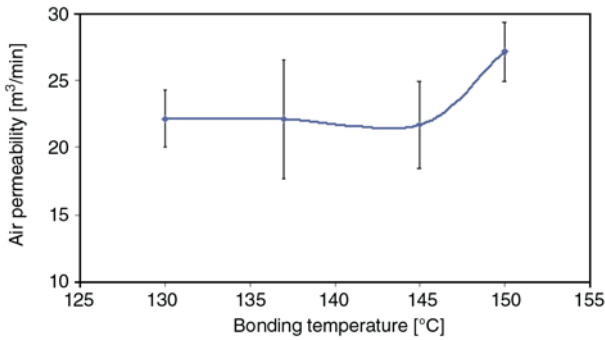
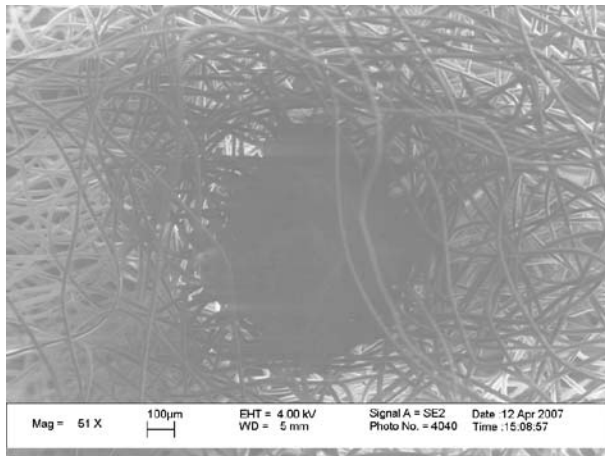


Figure 10. Air permeability vs. calendering temperature of the calendered PLA webs

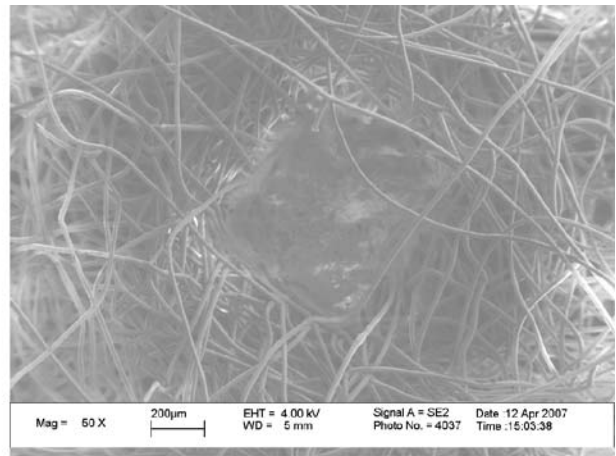
et al. [19] discussed that the mechanism by which tear resistance of the fabric can be improved is by the movement of individual fibers or yarns such that they form bundle at the tip of the tear, share the load and resist the tear propagation further. It is reported that in the tear test, yarns which were tested for tear resistance actually failed in tension [20]. Improving bond integrity increases load sharing between the fibers and hence increase in tear strength is exhibited. However, upon over bonding, the webs became stiffer and hamper the fiber movements to adjust into a bundle, thus reducing the load sharing ability of the fibers in the bonded structure leading to drop in tear strength.

3.6. Air permeability

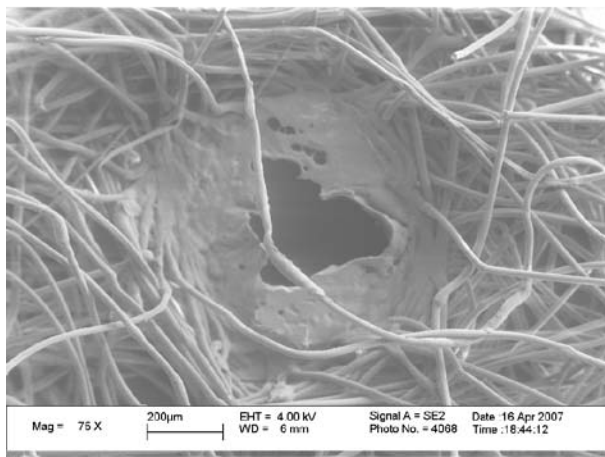
Thermally bonded carded webs showed almost the same air permeability with increasing calendering temperatures up to 145°C as shown in Figure 10. However for webs calendered at 150°C, there was a significant increase in air permeability. Since the



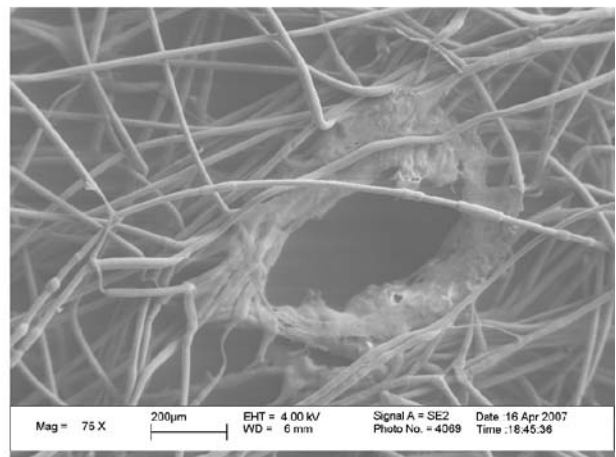
a) Calendering temperature: 130°C



b) Calendering temperature: 137°C



c) Calendering temperature: 145°C



d) Calendering temperature: 150°C

Figure 11. SEM Micrographs of the calendered PLA webs

basis weight of the webs is the same, it is expected that the air permeability remain more or less at the same level. The significant increase in air permeability at 150°C could be explained with the help of the structure at the bond points of the webs as seen in the optical micrographs in Figure 5 and in SEM photographs in Figure 11. Webs produced at 150°C showed big holes at the center of the bond points which could have formed due to the fact that as fibers approach their melting temperature of 164°C, they tend to relax more and more from the built in stresses in the fiber. Such stress relaxation caused the softened material to shrink and move towards the boundary of the bond points, thus leaving a hole in the center. Shrinkage of the softened polymer, and holes formation appeared to be taking place above 140°C, and was seen to be growing in size from 145 to 150°C. Such openness in the bond point area can explain the significant increase in air permeability at 150°C. In a study on the effect of bonding temperature on specialty elastomeric polyolefin spunbonded webs, Dharmarajan *et al.* [21] had observed the hole formation in the case of the webs produced from 100% elastomeric polyolefins. However, they did not discuss the reasons for formation of holes.

4. Conclusions

PLA staple fibers can be converted into nonwoven webs using the carding process and a subsequent thermal calendering. Selection of proper calendering conditions, especially the temperature, is important to produce stronger nonwovens. The optimum calendering temperature was found to be 145°C for the PLA carded webs produced under these conditions. The phenomenon of relaxation, as evidenced from hole formation was observed at higher calendering temperatures. This may be the combined effect of loss of molecular orientation, slower crystallization kinetics, and hence a decrease in crystallinity with increase in calendering temperature. The hole formation at bond point affected the characteristics of nonwoven webs such as air permeability and strength. Overall, strong webs can be produced by carding and thermal calendering, as long as optimum calendering conditions are selected.

Acknowledgements

Authors sincerely acknowledge the support from Fiber Innovations Technology, Johnson City, TN, for supplying PLA fibers used in this study.

References

- [1] Mooney D. J., Sano K., Kaufmann M. P., Majahod K., Schloo B., Vacanti J. P., Langer R.: Long term engraftment of hepatocytes transplanted on biodegradable polymer sponges. *Journal of Biomedical Materials Research*, **37**, 413–420 (1997).
- [2] Dugan J. S.: Novel properties of PLA fibers. *International Nonwovens Journal*, **10**, 29–33 (2001).
- [3] Gupta B., Revagade N., Hilborn J.: Poly(lactic acid) fiber: An overview. *Progress in Polymer Science*, **32**, 455–482 (2007).
- [4] Khan A. Y. A., Wadsworth L., Ryan C. M.: Melt processing of PLA resin into nonwovens. in 'Proceeding of Annual TANDEC conference. University of Tennessee, Knoxville, USA', **3**, 1–2 (1993).
- [5] Akaoka Y., Suzuki A.: PLLA nonwoven fabric prepared by CO₂ laser-thinning method II. (in Japanese) in 'Proceeding of Polymer Preprints, 55th SPSJ Symposium on Macromolecules, Nagoya, Japan', **55**, 4031 (2006).
- [6] Kamath M. G., Bhat G. S., Mueller D., Parikh D. V.: Cellulosic nonwoven-based composites. in 'Proceeding of Annual International TANDEC Nonwovens Conference. University of Tennessee, Knoxville, USA', **14**, 1–8 (2004).
- [7] Dharmadhikary R. K., Gilmore T. F., Davis H. A., Batra S. K.: Thermal bonding of nonwoven fabrics. *Textile Progress*, **26**, 1–39 (1994).
- [8] Bhat G. S., Jangala P. K., Spruiell J. E.: Thermal bonding of polypropylene nonwovens: effect of bonding variables on the structure and properties of the fabrics. *Journal of Applied Polymer Science*, **92**, 3593–3600 (2004).
- [9] Dahiya A., Kamath M. G., Hegde R. R.: Dry laid nonwovens. <http://www.engr.utk.edu/mse/Textiles/Dry%20Laid%20Nonwovens.htm>
- [10] Fischer E. W., Sterzel H. J., Wegner G.: Investigation of the structure of solution grown crystals of lactide copolymers by means of chemical reactions. *Colloid and Polymer Science*, **251**, 980–990 (1973).
- [11] ASTM D5729: Textiles. Standard test method for thickness of nonwoven fabrics (1997).
- [12] ASTM D5035: Textiles. Standard test method for breaking force and elongation of textile fabrics (Strip Method) (1995).
- [13] ASTM D737: Textiles. Standard test method for air permeability of textile fabrics (1996).
- [14] ASTM D5734: Textiles. Standard test method for tearing strength of nonwoven fabrics by falling-pendulum (Elmendorf) apparatus (1995).

- [15] Chand S., Bhat G., Spruiell J., Malkan S.: Role of fiber morphology in thermal bonding. *International Nonwovens Journal*, **11**, 12–20 (2002).
- [16] Mezghani K., Spruiell J. E.: High speed melt spinning of poly (L-lactic acid) filaments. *Journal of Polymer Science, Part B: Polymer Physics*, **36**, 1005–1012 (1998).
- [17] Bhat G. S., Malkan S. R.: Extruded continuous filament nonwovens: Advances in scientific aspects. *Journal of Applied Polymer Science*, **83**, 572–585 (2002).
- [18] Bhat G. S., Malkan S. R.: Polymer laid web formation. in 'Handbook of Nonwovens' (ed.: Russell S.) Woodhead Publishers, Cambridge, 143–200 (2007).
- [19] Primentas A.: Puncture and tear of woven fabrics. *Journal of Textile and Apparel, Technology and Management*, **1**, 1–8 (2001).
- [20] Hamkins C. P., Backer S.: On the mechanisms of tearing in woven fabrics. *Textile Research Journal*, **50**, 323–327 (1980).
- [21] Dharmarajan N.: Tailoring the performance of specialty polyolefin elastomer based elastic nonwoven fabrics. in 'Proceeding of INTC 2006, Houston, USA', 1–16 (2006).

Modeling and simulation of high-pressure industrial autoclave polyethylene reactor

E. Caliani¹, M. Cavalcanti², L. M. F. Lona¹, F. A. N. Fernandes^{3*}

¹Universidade Estadual de Campinas, Faculdade de Engenharia Química, Campinas – SP, Brazil

²Politeno Indústria e Comércio S/A, Camaçari – BA, Brazil

³Universidade Federal do Ceará, Departamento de Engenharia Química, Campus do Pici, Bloco 709, 60455-760 Fortaleza – CE, Brazil

Received 23 October 2007; accepted in revised form 12 November 2007

Abstract. High-pressure technology for polyethylene production has been widely used by industries around the world. A good model for the reactor fluid dynamics is essential to set the operating conditions of an autoclave reactor. The high-pressure autoclave reactor model developed in this work was based on a non-isothermal dynamic model, where PID control equations are used to maintain the operation at the unstable steady state. The kinetic mechanism to describe the polymerization rate and molecular weight averages are presented. The model is capable of computing temperature, concentration gradients and polymer characteristics. The model was validated for an existing industrial reactor and data for production of homopolymer polyethylene and has represented well the behavior of the autoclave reactor used in ethylene homopolymerization.

Keywords: modeling and simulation, polyethylene, LPDE, polymerization, autoclave reactor

1. Introduction

Low density polyethylene is produced by high-pressure processes either in autoclave vessel reactors or in tubular reactors. The process requires a highly purified ethylene feed and the operating pressure ranges from 1000 to 3000 atm. This work has developed a mathematical model based on the mixing model for the production of low density polyethylene in an industrial high-pressure autoclave vessel reactor and has compared the results with industrial data.

Several modeling techniques have been used to model this type of reactor [1–6] and some authors have shown that the mixing model is best fitted to this process. Although the mixing model is already known, few studies [1, 7–10] have reported and compared the results obtained from the mixing

model with actual industrial data. Furthermore, the autoclave vessel reactor has a complex controlling system where the temperature is controlled by the feed flow rate of initiator into the reactor and until now no study has published values for the PID controller parameters.

2. Autoclave vessel reactor

The autoclave vessel reactor is an autoclave with high length to diameter ratio, divided into several compartments. The reaction requires high power input per unit of volume to maintain good mixing conditions in each compartment. Because of the thickness of the wall, low surface area, and high heat load, the reactor can be considered essentially adiabatic. Polymerization temperature ranges from

*Corresponding author, e-mail: fabiano@ufc.br
© BME-PT and GTE

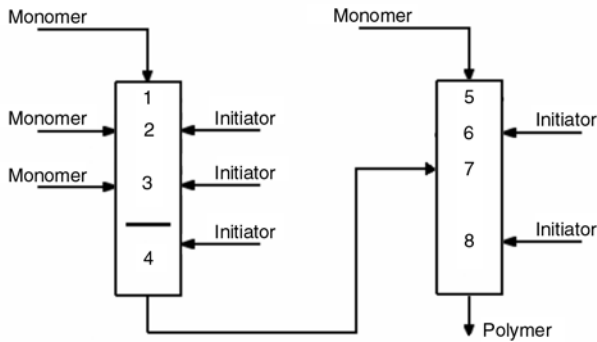


Figure 1. Industrial high-pressure vessel reactor

150 to 300°C and is set depending on the desired LDPE grade. Temperatures above 300°C should be avoided because of possible polyethylene decomposition. Fresh ethylene is fed to some compartments together with a radical source, usually an azocompound or peroxide, which decomposes and generates free radicals starting the polymerization reaction [3].

The reactor system modeled in this work consists of a series of two autoclave vessel reactors connected in series as shown in Figure 1. Fresh ethylene is fed into sections 1, 2, 3 and 5 of the reactors and the product from the first reactor is fed into section 7 of the second reactor. Mixing, in both reactors, is provided by a shaft running down the center of the reactor with several impeller blades. In the first reactor a baffle is placed near the bottom of the reactor to reduce backmixing of the mixture.

Heat transfer through the walls is limited and cooling is provided by the inflow of cold monomer. Temperature is controlled regulating the inflow of initiator to the reactor. Initiator is fed into sections 2, 3, 4, 6 and 8. Sections 1 and 5 (first section of

each reactor) have low reaction rates and have the primary function of cooling the agitator motor.

3. Mixing model

The mixing pattern in an autoclave type reactor tends to be of a recirculating nature. The effect of mixing on reactor performance is very important, especially because an imperfectly mixed vessel requires more initiator per unit of polymer produced than does a more perfectly mixed reactor under the same conditions [2]. The initiator tends to decompose near the feed points and not in the bulk of the reactor, thus not promoting as much polymerization as if the initiator were uniformly distributed throughout the reaction mixture. The temperature gradient down the reactor also suggests imperfect mixing [1].

The mixing pattern in the high-pressure reactor makes it behave more like a continuous stirred tank reactor (CSTR) rather than a tubular reactor. To account for imperfect mixing in the reactor, the autoclave reactor can be subdivided into several sections which can be represented by a series of small reactors consisting of a CSTR segment followed by a plug-flow segment that accounts for the temperature gradient down the reactor. Each plug-flow segment can be modeled as a series of small volume CSTRs avoiding to solve partial differential equations. The back mixing promoted by the impeller blades is considered, allowing each main CSTR segment of the reactor to recycle part of its volume back to the previous CSTR main segment (Figure 2).

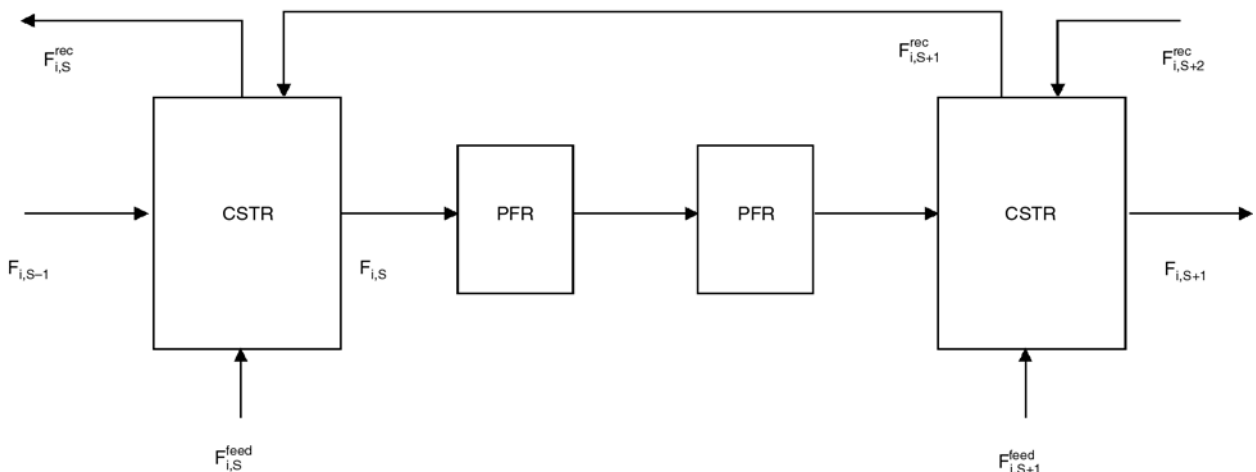


Figure 2. Mixing model structure and flow rates between two sections of the reactor

The mathematical model developed herein includes temperature controller equations to maintain the operation point at a desired steady state. The controller equations are needed because the industrial reactor normally operates at an unstable steady state in which the operation can either cause the temperature to rise or to cool down the reactor until no polymerization occurs.

Based on the flow rates shown in Figure 2, the mass balance for a species in a volume segment of the reactor is given by Equation (1):

$$\frac{dN_{i,S}}{dt} = F_{i,S}^{feed} + F_{i,S-1} + F_{i,R}^{rec} - F_{i,S} - F_{i,S}^{rec} + r_{i,S} \cdot V_S \quad (i, S \geq 1) \quad (1)$$

where, $F_{i,S}$ is the molar flow rate of the component i in the section S [mol/s]; $N_{i,S}$ is the number of mols of the component i in the section S [mol]; $r_{i,S}$ is the reaction rate of the component i in the section S [mol/s·l]; t is the time [s]; V_S is the volume of the section S [l]; and the superscript feed refers to the feed stream and rec refers to the recycle stream.

The plug-flow segments (PFR) do not have feed streams nor recycle streams going to other segments, and for these segments Equation (1) can be simplified to Equation (2):

$$\frac{dN_{i,S}}{dt} = F_{i,S-1} - F_{i,S} + r_{i,S} \cdot V_S \quad (i, S \geq 1) \quad (2)$$

To evaluate the effect of the macromixing parameters on the reactor fluid dynamics, two main parameters were defined: volume fraction of the CSTR segment to the total volume of the section (θ) and recycle ratio (β), as shown in Equations (3) and (4):

$$\theta = \frac{V_{S,CSTR}}{V_{S,TOTAL}} \quad (3)$$

$$\beta = \frac{Q_S^{rec}}{Q_S + Q_S^{rec}} \quad (S \geq 1) \quad (4)$$

where, Q_S is the total volumetric flow rate of the section S [l/s]; Q_S^{rec} is the volumetric flow rate of the recycle stream exiting the section S [l/s]; $V_{S,CSTR}$ is the volume of the CSTR segment of the section S [l]; $V_{S,TOTAL}$ is the total volume of section S [l]; θ is the recycle ratio; and θ is the volume fraction of the CSTR segment to the total volume of section S .

These parameters should be estimated for each reactor and for each section in the reactor. High θ values denote that the section resembles an ideal CSTR, while high β values denote good axial mixing among contiguous sections.

The energy balance of the reactor requires accounting for the inflows, outflows, recycles and reaction in each segment (Equation (5)). The reactor is assumed to be adiabatic and cooling is supplied by cold monomer feed. Heat generation is considered to come from the propagation reaction only.

$$\begin{aligned} (\rho_S \cdot Cp_S \cdot V_S) \frac{dT_S}{dt} = & \rho_S^{feed} \cdot Q_S^{feed} \cdot Cp_S^{feed} \cdot (T_S^{feed} - T_{ref}) + \\ & \rho_{S-1} \cdot Q_{S-1} \cdot Cp_{S-1} \cdot (T_{S-1} - T_{ref}) + \\ & \rho_R^{rec} \cdot Q_R^{rec} \cdot Cp_R^{rec} \cdot (T_R^{rec} - T_{ref}) - \\ & \rho_S \cdot Q_S \cdot Cp_S \cdot (T_S - T_{ref}) - \\ & \rho_S \cdot Q_S^{rec} \cdot Cp_S \cdot (T_S - T_{ref}) - \Delta H \cdot r_S \cdot V_S \end{aligned} \quad (5)$$

where, Cp_S is the heat capacity of the mixture in section S [J/g·K]; T_S is the temperature of section S [K]; T_{ref} is the reference temperature [K]; ρ_S is the density of the mixture in section S [g/l]; ΔH is the heat of reaction [J/mol].

Temperature is controlled by manipulating the flow rate of the initiator feed stream based on the actual temperature of some measured segments and on the set-point temperature. The controller applied to the reactor modeled herein was a proportional-integral-derivative type (PID controller – Equation (6)) and 5 controllers were used to control the initiator feed into sections 2, 3, 4, 6 and 8, as in the industrial reactor.

$$\begin{aligned} \Delta F_I = & \\ & K_c \cdot \left[(E_n - E_{n-1}) + \frac{\Delta t}{\tau_I} \cdot E_n + \frac{\tau_D}{\Delta t} \cdot (E_n - 2 \cdot E_{n-1} + E_{n-2}) \right] \end{aligned} \quad (6)$$

where, F_I is the molar flow rate of initiator in the initiator feed stream [mol/s]; K_c is the proportional gain [mol/s·K]; E is the error between the actual temperature and the set-point temperature [K]; τ_I is the integral gain [s]; and τ_D is the differential gain [s].

Ethylene free radical polymerization mechanism and kinetics was outlined by Zabisky *et al.* [11] and Chan *et al.* [1] for a two phase kinetic mechanism where a monomer and a polymer rich phase exist in the reaction mixture. Herein, a homopolymer presenting only one phase in the reactor (monomer rich phase) was assumed and the momentum equations to account for the molecular weight of the polymer were adapted from Zabisky *et al.* [11] for a one phase kinetic mechanism.

The kinetic mechanism considered the initiation of radical by thermal decomposition of the initiator, chain propagation, termination by combination and disproportionation, transfer to monomer and to polymer and reaction with terminal double bond. The moments for live and dead polymers are given by Equations (7) to (12). The fraction of dead polymers with terminal double bond was calculated dividing the reaction rates of the reactions that produce dead polymers with terminal double bonds by the reaction rates of all reactions taking place during polymerization.

$$\frac{dY_0}{dt} = F_{i,S-1}^{Y_0} - F_{i,S}^{Y_0} + F_{i,S+1,rec}^{Y_0} - F_{i,S,rec}^{Y_0} + 2 \cdot f \cdot k_d \cdot [I] - k_{tc} \cdot Y_0^2 - k_{td} \cdot Y_0^2 \quad (7)$$

$$\frac{dY_1}{dt} = F_{i,S-1}^{Y_1} - F_{i,S}^{Y_1} + F_{i,S+1,rec}^{Y_1} - F_{i,S,rec}^{Y_1} + k_p \cdot [M] Y_0 - k_{tc} \cdot Y_0 \cdot Y_1 - k_{td} \cdot Y_0 \cdot Y_1 + k_{fp} \cdot (Y_0 \cdot Q_2 - Y_1 \cdot Q_1) + k_{fm} \cdot [M] (Y_0 - Y_1) + k_{db} \cdot \alpha \cdot (Y_0 \cdot Q_2 - Y_1 \cdot Q_1) \quad (8)$$

$$\frac{dY_2}{dt} = F_{i,S-1}^{Y_2} - F_{i,S}^{Y_2} + F_{i,S+1,rec}^{Y_2} - F_{i,S,rec}^{Y_2} + k_p \cdot [M] (2 \cdot Y_1 + Y_0) - k_{tc} \cdot Y_0 \cdot Y_2 - k_{td} \cdot Y_0 \cdot Y_2 + k_{fp} \cdot (Y_0 \cdot Q_3 - Y_2 \cdot Q_1) + k_{fm} \cdot [M] (Y_0 - Y_2) + k_{db} \cdot \alpha \cdot (Y_0 \cdot Q_3 - Y_2 \cdot Q_1) \quad (9)$$

$$\frac{dQ_0}{dt} = F_{i,S-1}^{Q_0} - F_{i,S}^{Q_0} + F_{i,S+1,rec}^{Q_0} - F_{i,S,rec}^{Q_0} + 0.5 \cdot k_{tc} \cdot Y_0^2 + k_{td} \cdot Y_0^2 + k_{fp} \cdot (-Y_0 \cdot Q_2 + Y_1 \cdot Q_1) + k_{fm} \cdot [M] Y_0 - k_{db} \cdot \alpha \cdot Q_1 \cdot Y_0 \quad (10)$$

$$\frac{dQ_1}{dt} = F_{i,S-1}^{Q_1} - F_{i,S}^{Q_1} + F_{i,S+1,rec}^{Q_1} - F_{i,S,rec}^{Q_1} + k_{tc} \cdot Y_0 \cdot Y_1 + k_{td} \cdot Y_0 \cdot Y_1 + k_{fp} \cdot (-Y_0 \cdot Q_2 + Y_1 \cdot Q_1) + k_{fm} \cdot [M] Y_1 - k_{db} \cdot \alpha \cdot Q_2 \cdot Y_0 \quad (11)$$

$$\frac{dQ_2}{dt} = F_{i,S-1}^{Q_2} - F_{i,S}^{Q_2} + F_{i,S+1,rec}^{Q_2} - F_{i,S,rec}^{Q_2} + k_{tc} \cdot (Y_0 \cdot Y_2 + Y_1^2) + k_{td} \cdot Y_0 \cdot Y_2 + k_{fp} \cdot (-Y_0 \cdot Q_3 + Y_2 \cdot Q_1) + k_{fm} \cdot [M] Y_2 - k_{db} \cdot \alpha \cdot Q_3 \cdot Y_0 \quad (12)$$

where, f is the initiator efficiency; $[I]$ is the initiator concentration [mol/l]; k_d is the decomposition rate constant of the initiator [1/s]; k_{db} is the reaction with terminal double bond rate constant [l/mol·s]; k_{fm} is the transfer to monomer rate constant [l/mol·s]; k_{fp} is the transfer to polymer rate constant [l/mol·s]; k_p is the propagation rate constant [l/mol·s]; k_{tc} is the termination by combination rate constant [l/mol·s]; k_{td} is the termination by disproportionation rate constant [l/mol·s]; $[M]$ is the monomer concentration [mol/l]; Y_i is the i^{th} live polymer moment [mol/l]; Q_i is the i^{th} dead polymer moment [mol/l]; α is the fraction of polymer with terminal double bonds.

The transfer to polymer reaction and reaction with terminal double bonds lead to polymer moment equations that are not closed, where the i^{th} moment depends on the $(i+1)^{\text{th}}$ moment. To solve this problem, the closure technique presented by Hulburt and Katz [12] was used to calculate the third moment of the polymer distribution, as recommended by Zabisky *et al.* [11]. As such, the third moment of the dead polymer was calculated by Equation (13):

$$Q_3 = \left(\frac{Q_2}{Q_1 \cdot Q_0} \right) (2 \cdot Q_0 \cdot Q_2 - Q_1^2) \quad (13)$$

The kinetic parameters used in the simulations are presented in Table 1 and were based on the data published by Zabisky *et al.* [11] and Chan *et al.* [1]. The full dynamic mathematical model comprised 308 ordinary differential equations to calculate the

Table 1. Kinetic parameters for polyethylene homopolymer production [1, 11]

Reaction	k_0 [l/mol·s]	E_a [cal/mol]
Initiation [s ⁻¹]	8.4·10 ¹⁵	36 900
Propagation	3.0·10 ⁸	8 065
Termination by disproportionation	1.25·10 ⁹	999
Termination by combination	1.25·10 ⁹	999
Transfer to monomer	1.25·10 ⁵	8 078
Transfer to polymer	2.0·10 ⁸	21 235
Reaction with terminal double bond	1.25·10 ⁷	8 078

material balance of all components, the energy balance and the population balance (via method of moments). The model was written in Fortran and was solved using a 5th order Runge-Kutta integration method with variable integration step.

4. Results and discussion

Industrial production recipes from Politeno (Brazil) were used to simulate and validate the model. Validation of the model was carried out comparing the values predicted by the model with observed industrial steady-state values for monomer profile, initiator flow rates, temperature profile and final product characteristics.

The industrial reactor was divided into eight sections (Figure 1). The volumes of the reaction sections were 16.8, 13.7, 12.8, 13.3, 16.8, 8.3, 15.3 and 3.0% of the total volume of the reactor. The monomer feed distribution assumed that 12.5, 25.0, 50.0 and 12.5% of the total monomer feed entered the first segment of sections 1, 2, 3 and 5 respectively. The initiator (di-tert-butyl peroxide) was fed into the first segment of sections 2, 3, 4, 6 and 8. The operating pressure was 1600 atm and the temperature of the ethylene feed was 353 K. The temperature of the third segment of sections 2, 3, 4 and 6 and 8 were controlled at 513, 513, 537, 513 and 531 K, respectively.

The best controller parameters found for the reactor were: $K_c = 0.0001$, $\tau_D = 0.005$, $\tau_I = 3.0$ for the first controlled section and $K_c = 0.00005$, $\tau_D = 0.005$,

$\tau_I = 5.0$ for the other controlled sections. Figure 3 shows a representative result of the variation of temperature (controlled variable) at reactor startup. Temperature control is a key factor for the operation of the autoclave reactor and it is very important that the controller manages to stabilize the temperature within a short time span. The PID controller implemented in the model and the control parameters found were able to control the temperature within a few residence times showing the efficiency of the control system.

The mixing parameters (θ and β) are important parameters for the model and must be thoroughly studied, as well as the number of plug-flow segments within a section of the reactor (N_p). Several simulations were carried out to find the best set of mixing parameters and N_p for the industrial autoclave reactor being simulated.

These parameters need to be correctly estimated because they have a significant influence in the simulations and thus must be validated with industrial reactor data. The number of plug-flow segments was studied running simulations with 1 to 5 plug-flow segment in each section of the reactor. The addition of plug-flow segments in the model lead to a more gradual increase of segment temperature and a more gradual decrease of segment ethylene concentration. Figure 4 presents the effect of the number of plug-flow segments on temperature and ethylene concentration (for sections 2 and 3).

Although using a large number of plug-flow segments (7) have been suggested by Chan *et al.* [1], in our simulations we have observed that the use of only 2 plug-flow segments provided a more satisfactory simulation with the model with better representation of the industrial reactor. This result is corroborated by the observations made by Pladis and Kiparissides [10] for similar reactors. These results show that when the reactor has good back-mixing of the reaction mixture the simulations should consider more plug-flow segments within each section because the changes in temperature and ethylene concentration along the reactor will be smoother. However, if the reactor does not present good back-mixing or if the flow rate of ethylene is high then the temperature along each reactor section will increase considerably. In this latter case, few plug-flow segments should be incorporated to the reactor model.

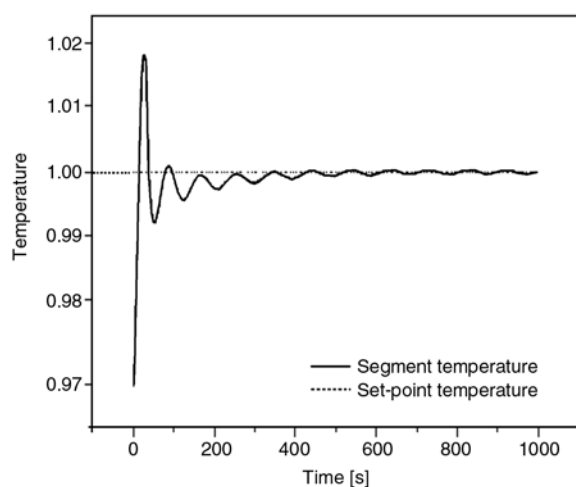


Figure 3. Dynamic response of an internal segment of the reactor (Segment 12). Temperature was normalized due to contract reasons

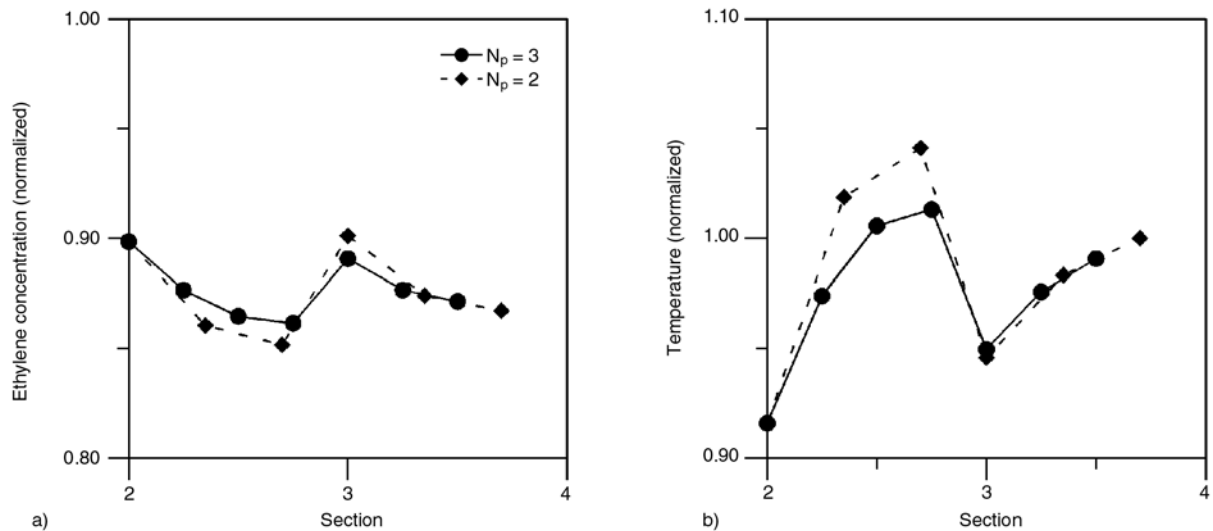


Figure 4. Effect of the number of plug-flow segments on monomer concentration (a) and temperature profiles (b) for sections 2 and 3 of the first reactor ($\theta = 0.70$)

Volume fractions of the CSTR segment to the total volume of the section (θ) from 0.5 to 1.0 were studied. Increasing the CSTR segment volume (θ) in the model provided better mixing of the segment resulting in a gradual increase of temperature between the sections of the reactor, as well as a gradual decrease of ethylene concentration along the reactor. Figure 5 presents the effect of the CSTR segment volume on temperature and ethylene concentration (for sections 2 and 3). Our simulations showed that the use of a CSTR segment volume of 0.70 provided a more satisfactory simulation with the model fitting better with the industrial reactor. This result corroborated with the observations made by Chan *et al.* [1] for a simi-

lar reactor. These results showed that the industrial reactor presents poor mixing in each segment and steep temperature and concentration variations occur near the feeding points of the reactor as is observed between sections 2 and 3.

Recycle ratios (β) from 0.0 to 0.4 were studied. The increase in the recycle ratio (β) in the model provided better mixing among the sections resulting in a flatter temperature profile between the segments and the sections of the reactor. Figure 6 presents the effect of the CSTR segment volume on temperature and ethylene concentration for sections 2 and 3. Figure 7 presents the same effect for all 8 sections of the two reactors.

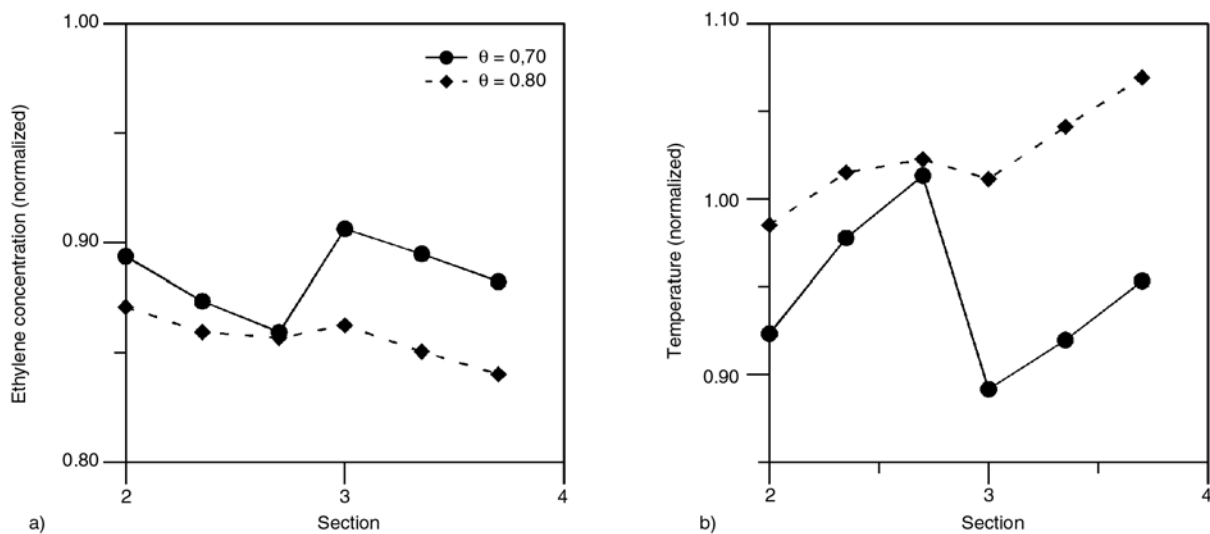


Figure 5. Effect of the CSTR segment volume on monomer concentration (a) and temperature profiles (b) for sections 2 and 3 of the first reactor ($N_p = 2$)

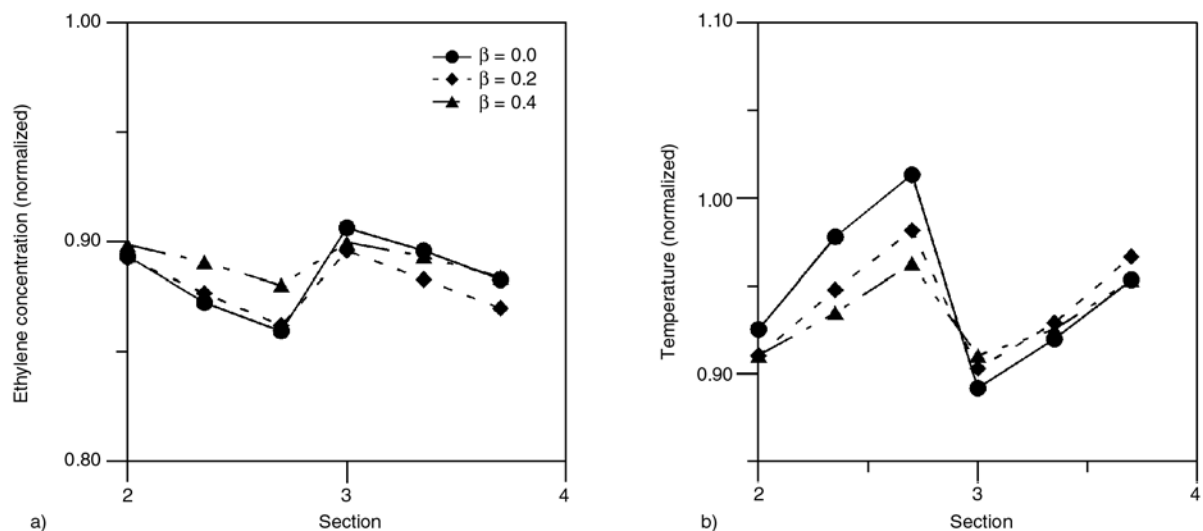


Figure 6. Effect of the recycle ratio on the monomer concentration (a) and the temperature profiles (b) for the first segment (CSTR segment) of each section of the reactor ($\theta = 0.70$; $N_p = 2$)

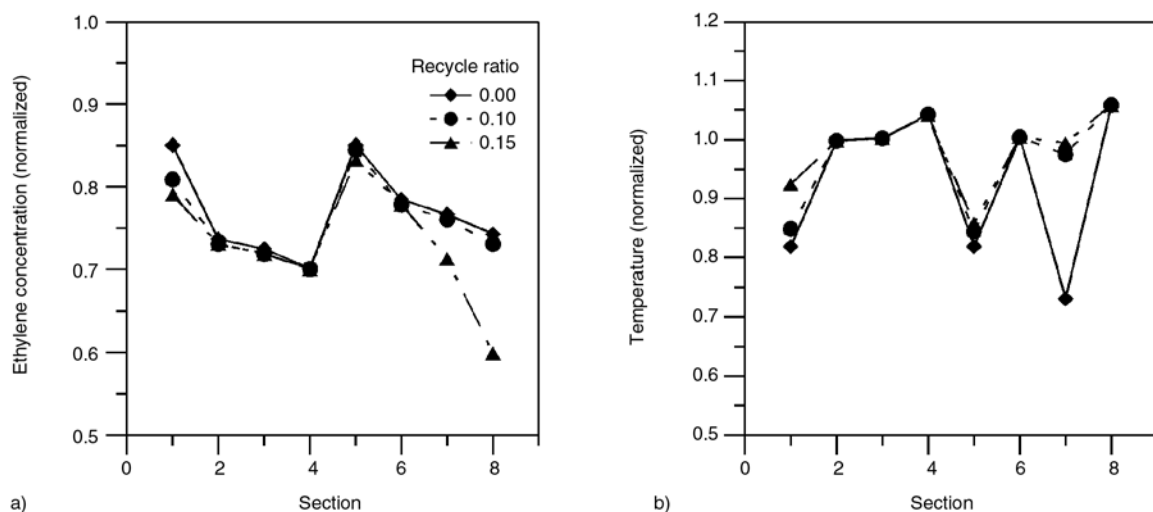


Figure 7. Effect of the recycle ratio on the monomer concentration (a) and the temperature profiles (b) for the first segment (CSTR segment) of each section of the reactor ($\theta = 0.70$; $N_p = 2$)

Comparing the profiles obtained in Figure 7 to actual reactor profiles have showed that none of the profiles obtained with simulations that were carried out with constant recycle ratios (all sections using the same recycle ratio) have displayed a satisfactory fit to the actual reactor data. Analyzing the configuration of the reactor and the fraction of ethylene feed in each section, we could establish that not all sections would display the same recycle ratio and that this parameter has to be carefully set for each reactor design. For the design shown in Figure 1, the recycle ratio of section 4 (towards section 3) was set to zero since the baffle between sections 3 and 4 minimizes the recycle and back-mixing of the reaction mixture. The recycle ratio of

section 3 (towards section 2) was increased since the flow rate of ethylene fed into section 3 is larger and as such a better mixing can occur near this feeding point. The best configuration found for the mixing parameters of the model where: volume fraction of the CSTR segment to the total volume of the section (β) of 0.70 for all sections; and recycle ratio (β) of 0.15, 0.30, 0.15, 0.15 and 0.05 for the sections 2, 3, 6, 7 and 8, respectively. A comparison with industrial data is shown in Figure 8.

The results found in Figure 8 are quite good and the largest relative error of the predicted values was less than 5% and as such we can state that the model truly represents the industrial reactor behavior.

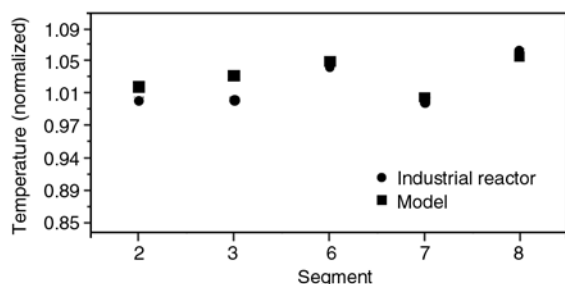


Figure 8. Comparison of temperature profiles between the proposed model and actual industrial data for polyethylene homopolymerization

5. Conclusions

A comprehensive model describing the high-pressure autoclave reactor for polyethylene production was developed, accounting for the mixing pattern in the reactor, the mechanistic polymerization reaction and temperature control. The model was proven satisfactory and has fitted homopolymer recipes for ethylene flow rates, initiator flow rates and temperature profiles.

Acknowledgements

The authors wish to acknowledge Politeno, Finep and CNPq for the financial support for this project.

References

[1] Chan W-M., Gloor P. E., Hamielec A. E.: Kinetic model for olefin polymerization in high-pressure autoclave reactors. *AIChE Journal*, **39**, 111–126 (1993).
 [2] Marini L., Georgakis C.: The effect of imperfect mixing on polymer quality in low density polyethylene vessel reactors. *Chemical Engineering Communications*, **30**, 361–375 (1984).

[3] Marini L., Georgakis C.: Low density polyethylene vessel reactors. Part I: A novel controller. *AIChE Journal*, **30**, 401–415 (1984).
 [4] Topalis E., Pladis P., Kiparissides C., Goossens I.: Dynamic modelling and steady-state multiplicity in high pressure multizone LDPE autoclaves. *Chemical Engineering Science*, **51**, 2461–2470 (1996).
 [5] Sarmoria C., Brandolin A., López-Rodríguez A., Whiteley K. S., Del Amo Fernandez B.: Modeling of molecular weights in industrial autoclave reactors for high pressure polymerization of ethylene and ethylene-vinyl acetate. *Polymer Engineering Science*, **40**, 1480–1494 (2000).
 [6] Wells G. J., Ray W. H.: Mixing effects on performance and stability of low-density polyethylene reactors. *AIChE Journal*, **51**, 3205–3218 (2005).
 [7] Ghiass M., Hutchinson R. A.: Simulation of free radical high-pressure copolymerization in a multi-zone autoclave reactor: Compartment model investigation. *Macromolecular Symposia*, **206**, 443–456 (2004).
 [8] Ghiass M., Hutchinson R. A.: Simulation of free radical high-pressure copolymerization in a multi-zone autoclave reactor: Model development and application. *Polymer Reaction Engineering*, **11**, 989–1015 (2004).
 [9] López A., Pedraza J. J., Del Amo B.: Industrial application of a simulation model for high pressure polymerization of ethylene. *Computers and Chemical Engineering*, **20**, S1625–S1630 (1996).
 [10] Pladis P., Kiparissides C.: Dynamic modeling of multizone, multifeed high-pressure LDPE autoclaves. *Journal of Applied Polymer Science*, **73**, 2327–2348 (1999).
 [11] Zabisky R. C. M., Chan W-M., Gloor P. E., Hamielec A. E.: A kinetic model for olefin polymerization in high-pressure tubular reactors: a review and update. *Polymer*, **33**, 2243–2262 (1992).
 [12] Hulburt H. M., Katz S.: Some problems in particle technology: A statistical mechanical formulation. *Chemical Engineering Science*, **19**, 555–574 (1964).

Stabilizing effect of epoxidized sunflower oil as a secondary stabilizer for Ca/Hg stabilized PVC

M. T. Taghizadeh*, N. Nalbandi, A. Bahadori

Department of Physical Chemistry, Faculty of Chemistry, University of Tabriz, Tabriz, Iran

Received 21 May; accepted in revised form 26 November 2007

Abstract. Unsaturated triglyceride oil sunflower was epoxidized and characterized by chemical and spectroscopic methods. Epoxidized sunflower oil (ESO) was used as an organic thermal co-stabilizer for rigid poly(vinyl chloride) (PVC) in the presence of tricalcium dicitrate ($\text{Ca}_3(\text{C}_6\text{H}_5\text{O}_7)_2$) and mercury (II) acetate ($\text{Hg}(\text{CH}_3\text{COO})_2$). The thermo-oxidative degradation of PVC was studied in the presence of these ternary stabilizer systems at 170, 180, 190 and 200°C in N_2 atmosphere. The effects of metal carboxylate combination Ca/Hg in the absence and in the presence of epoxidized sunflower oil on static heat treatment of PVC have been studied. The formation of polyene sequences was investigated by UV-visible and FT-IR spectroscopy and by comparing viscosity data obtained in the presence and in the absence of the additives. It was found that the additives retard the rate of degradation and reduce the extent of polymer chain scission associated with the thermal degradation of poly(vinyl chloride). Synergistic effects were found when stabilizer was blended in 50:50 weight ratios with either. It was found that ESO exerted a stabilizing effect on the degradation of PVC. The activation energy for degraded PVC in absence of stabilizers was $38.6 \text{ kJ}\cdot\text{mol}^{-1}$ and in the presence of Ca/Hg and Ca/Hg/ESO were 53.3 and $64.7 \text{ kJ}\cdot\text{mol}^{-1}$ respectively.

In order of compare the efficiency of the epoxidized sunflower oil with these metal soap stabilizers, thermal stabilities were evaluated on the basis of evolved hydrogen chloride determined by conductometry technique and degree of discoloration are discussed.

Keywords: thermal properties, poly(vinyl chloride), thermal stabilization, thermo-oxidative degradation, secondary stabilizer

1. Introduction

Poly(vinyl chloride), PVC, is one of the leading thermoplastic materials. It stands second in the world after polyethylene so far as production is concerned. However, PVC shows low thermal stability [1]. It is generally accepted that poly(vinyl chloride), PVC, is an unstable polymer when exposed to high temperatures during its moldings and applications. Therefore, the poor thermal stability of PVC still remains one of its main problems [2]. Thermal degradation of PVC occurs by an autocatalytic dehydrochlorination reaction with the subsequent formation of conjugated double bonds [3].

Dehydrochlorination initiated at the labile site in the polymer chains. This leads to an extensive discoloration of the polymer and deterioration of its physical and mechanical properties. Possible defect structures in PVC are allylic chlorine [4], tertiary hydrogen and chlorine atom [5], end groups such as double bonds [6], oxygen containing group, peroxide residue [7], head-to-head structures [8]. Some authors have claimed that these structural irregularities are responsible and can account for the low thermal stability of PVC.

Although structural defects considerably increase the initial rate of PVC degradation, and indeed ini-

*Corresponding author, e-mail: mttaghizadeh@tabrizu.ac.ir
© BME-PT and GTE

tial rates of degradation at low conversions ($0.1\pm 0.3\%$) have been shown to correlate well with allylic and/or tertiary chloride content of PVC [9]; it has been argued that on account of the low concentrations in normal PVC of these structural irregularities, that initiation of thermal degradation of PVC also takes place at regular monomer units [8]. In addition to the difficulties in identification and quantification of such small amount of labile allylic and tertiary chlorides within normal PVC structure, it is difficult to separate their effects on degradation from that of normal polymer units. It is now generally well accepted that random elimination of HCl from regular monomer sequence are responsible for the higher degree of conversion which degrades the polymer [10].

Because these changes are accompanied by deterioration on some of the useful properties of the polymer, it has become the practice to process PVC in the presence of heat stabilizers. Thermal stabilizers for PVC are known to function by replacing labile chlorine atoms in the polymer; they modify chain reactions and thereby inhibit the elimination of hydrogen chloride and interrupt the formation of polyene sequences in the polymer [5].

Additives that have found practical application as thermal stabilizers for PVC include metal soaps of carboxylic acids, organometallic compounds and inhibitors of radical chain reactions [9]. The most important stabilizers of PVC are different metal soaps like Pb, Cd, Ba, Ca and Zn carboxylates and some di- and mono-alkyltin compounds, e.g., maleates, carboxylates, mercaptides [11]. A wide variety of stabilizers is used industrially to improve the thermal stability of the polymer. The commonly used stabilizers are usually basic lead salts that can react with the evolved hydrogen chloride gas thus they retard the deleterious catalytic action of the eliminated hydrogen chloride, or substances that can exchange the labile functional group in the backbone chain for other more stable substituent derived from the stabilizer; for example, metallic soaps [12], esters or mercaptides of alkyl tin or material whose stabilizing action is through intervention with the radical process of degradation such as quinone tin polymer.

Moreover, the stabilizer may function by disruption of the conjugated system, thus reducing the discoloration of the polymer. Mercaptans are typical

example of these stabilizers. However, irrespective of their stabilizing efficiencies; they suffer from the deleterious effect of their byproduct, mostly metal chloride, accumulated during the reaction of these stabilizers with the polymeric chain [13].

These metal chlorides are considered as strong catalysts for the subsequent dehydrochlorination process, and they are responsible for the sudden blackening of certain formulation, and may present a serious environmental problem. This has led, recently, to the extensive use of stabilizers of an organic nature for the thermal stabilization of PVC [14].

Epoxy compounds are well known as typical non-metallic stabilizers for PVC [15]. They are generally regarded as secondary stabilizers used to enhance the effectiveness of metal soaps. They act as acceptors for the liberated hydrogen chloride [16, 17] and retardants for the appearance of discoloration [18, 19]. The effects of epoxidized sunflower (ESO) on the thermal degradation and stabilization of PVC in the presence of metal carboxylates (Ba/Cd and Ca/Zn stearates) have been investigated. ESO showed excellent properties as secondary stabilizer for PVC [20].

In this work, commercial sunflower oil was epoxidized. The stabilizing effect of epoxidized sunflower oil (ESO) on the thermal degradation of PVC in presence and absence of mixture tricalcium dicitrate and mercury (II) acetate and the ratios of Ca and Hg carboxylate (1/1, 1/2, 1/3, 2/1, 2/2, 2/3, 3/1, 3/2) and ESO in combination with Ca/Hg carboxylate under atmosphere of nitrogen have been investigated. The dehydrochlorination process in PVC degradation has been studied in detail using viscometric and spectrophotometric analysis and the values of the kinetic parameters have been calculated.

2. Experimental

2.1. Materials

Poly(vinyl chloride), PVC, suspension, with K value of 69–71; tricalcium dicitrate and mercury (II) acetate from Fluka Company were used for this investigation. PVC was purified by solution in THF/acetone mixture and precipitated with constant stirring in a large excess of methanol. The precipitated polymer was filtered off after 24 h,

washed with methanol, and air-dried (60°C) [21]. Commercial sunflower oil, was used. Epoxidized sunflower oil was prepared by epoxidation. Amberlite IR-120 cross-linked ploy(styrene-sulfonic acid) ion exchange resin and hydrogen peroxide (30%) were purchased from Fluka Company. All analytical grade solvents were used as obtained from pro-labo.

2.2. Preparation of epoxidized sunflower oil (ESO)

The epoxidation of sunflower oil was carried out at 50°C using peroxy-acetic acid prepared *in situ* by reacting hydrogen peroxide (30% v/v) with excess glacial acetic acid and Amberlite IR-120 [22]. The level of epoxidation was determined using a standard analytical method [23]. ESO with oxirane oxygen level 4.5% was prepared.

2.3. Degradation of PVC: rates of dehydrochlorination

Degradation studies were carried out using PVC powder in the presence of ESO (0.04 g), tri-calcium dicitrate and mercury (II) acetate (0.008 g) at 170, 180, 190 and 200°C under nitrogen atmosphere. The PVC sample (0.5 g) was mixed thoroughly with an appropriate amount of the additive and transferred into a degradation tube. The tube was connected to a source of nitrogen maintained at a flow rate of 250 ml·min⁻¹. The degradation tube was then immersed in a thermostat oil bath. The amount of evolved HCl was established after various periods of time by conductometry. The extent of dehydrochlorination (conversion %) was calculated from the ratio of evolved HCl to the amount available in the polymer [24].

2.4. UV-visible analysis

UV-visible spectra of purified PVC solutions in distilled 1,2-dichloroethane (2 g/l) were obtained by using a Shimadzu 120-02 UV-visible spectrophotometer. The polymer was purified by dissolution in 1,2-dichloroethane, precipitation with methanol and filtration.

The extent of discoloration of the degradation polymer sample was measured colorimetrically at $\lambda = 360$ nm as a function of the degradation time.

2.5. FT-IR analysis

IR spectra were measured using a Shimadzu infrared spectrophotometer (FTIR-4300) in the range 600–4000 cm⁻¹ at 25°C. All the samples were mixed with KBr for these analyses.

2.6. Intrinsic viscosity measurements

The degraded PVC (0.05 g) was purified by solution in cyclohexanone and precipitated in a large excess of methanol. The precipitated polymer was filtered off, washed several times with methanol, dried in vacuum at room temperature. Intrinsic viscosities were determined using a setgvis kinematic from measurements in cyclohexanone solution at 30°C. The intrinsic viscosities and relative and specific viscosities of solutions were calculated by Equations (1)–(3) [25]:

$$\eta = \frac{(\eta_{sp} + 3 \ln \eta_{rel})}{4C} \quad (1)$$

$$\eta_{rel} = \frac{\eta}{\eta_0} = \frac{t}{t_0} \quad (2)$$

$$\eta_{sp} = \eta_{rel} - 1 \quad (3)$$

where η , η_{sp} and η_{rel} are the intrinsic, specific and relative viscosities, respectively, C is the concentration of the solution [g/ml]. In these expressions, t is the time of flow of polymer solution and t_0 , the time of flow of solvent at the temperature of measurement. The ratios of the intrinsic viscosity of PVC samples degraded in the presence of additives to the intrinsic viscosity of undegraded samples, (η/η_0), was used to deduce the effect of the additives on the degradation of PVC.

3. Results and discussion

3.1. Effect of the stabilizer concentration on the efficiency of stabilization

The results of the dehydrochlorination of rigid PVC (0.5 g) stabilized by tricalcium dicitrate in different concentrations (0.4–3% w/w) are shown in Figure 1. They indicate that with increasing of [tricalcium dicitrate]/[PVC] ratio up to about 1.6% w/w of stabilizer, the rate of dehydrochlorination decreases and thereafter it increases. It can be seen from the results that the effect of Ca on the degra-

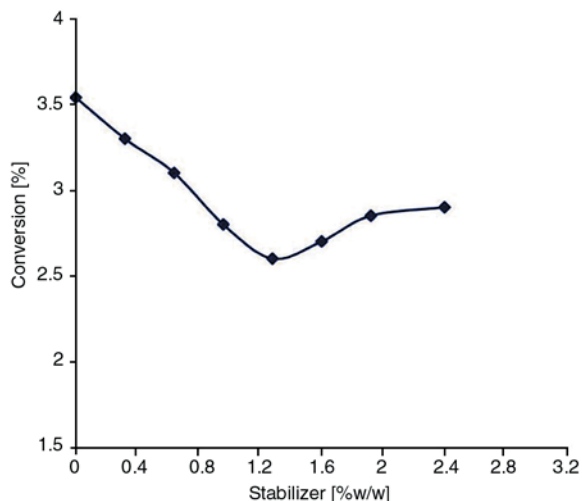


Figure 1. Conversion [%] of rigid PVC at 180°C with 0.5 g of PVC for various concentration of tricalcium dicitrate

dation of PVC is not additive: showing antagonistic effect up to 1.6% w/w Ca and synergistic effect at higher Ca. The data of others compounds show that the stabilizing efficiency of mercury (II) acetate and ESO is greater with concentration of 1.6% w/w and 0.8% w/w, respectively. It is known that labile chlorine atoms in PVC, especially allylic and tertiary chlorine, reduce the thermal stability of this polymer [26–31].

3.2. Stabilization of thermally degraded rigid PVC using mixed stabilizer (Ca/Hg) in the absence of ESO

The results of the dehydrochlorination of thermally degraded rigid PVC (0.5 g) at 180°C in N₂ in the presence of the mixed stabilizers (Ca/Hg) are shown in Figure 2. The results clearly reveal the greater stabilizing efficiency of the mixed stabilizers, reaching its maximum when the two stabilizers were mixed in a 2:2 ratio, respectively. It can be seen that the stabilizing effect of Ca stabilizer is enhanced by the presence of Hg stabilizer. The marked reductions in the rate of dehydrochlorination using mixed stabilizer (Ca/Hg) may be attributed to synergism of Hg and Ca compounds in stabilizing PVC against thermal degradation.

The mechanism by which metal soaps stabilize PVC against thermal degradation was first proposed by Frye and Horst [32, 33] and it involves the replacement of labile chlorine atoms within PVC

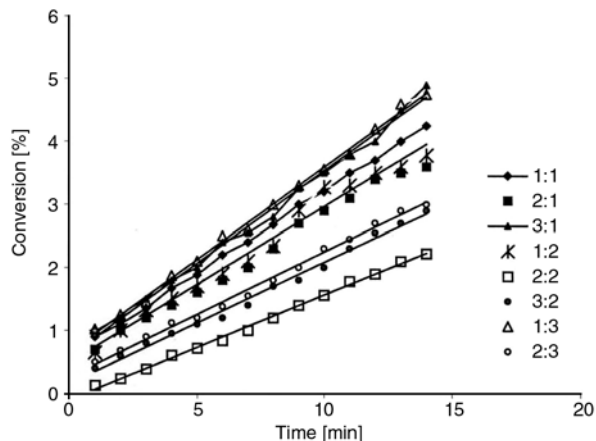


Figure 2. Conversion [%] of rigid PVC at 180°C with 0.5 g of PVC containing various ratios of Ca/Hg in the absence of ESO

structure with carboxylate groups which are more stable to heat treatment.

3.3. Stabilization of thermally degraded rigid PVC using mixed stabilizer (Ca/Hg/ESO)

It is well known that the ability to prevent dehydrochlorination of PVC is an important characteristic in the evaluation of the stabilizing effect. The experimental values of dehydrochlorination of rigid PVC at 180°C in N₂ in the presence of additives and mixed additives are given in Figure 3.

Figure 3 shows the dehydrochlorination curves of PVC containing metal carboxylates and Ca/Hg (2/2) in the absence and in the presence of ESO for comparable the Ca/Hg stabilizer in the weight ratio of 1/1 when used in combination with ESO was found to be most effective.

It can be seen from Figure 3 that the lower value was obtained for the Ca/Hg (1/1)-ESO, for this synergistic mixture of stabilizers, the presence of ESO reduced effectiveness the initial rates of dehydrochlorination (DHC).

The investigated ESO exhibits a greater stabilizing efficiency compared to others. The greater stabilizing efficiency is illustrated not only by lower rates of DHC during the subsequent stages of degradation reaction, but also by the longer induction periods or the thermal stability value (*T_s*) during which no detectable amounts of hydrogen chloride gas are liberated and the values of the required time for dehydrochlorination to attain 1% conversion, *t_{DH}*, for all additives are shown in Table 1.

Table 1 gives the values of induction times and of initial rates of DHC which were computed from the slopes of the kinetic curves (Figure 3), The addition of ESO to Ca/Hg (1/1) increases the induction time and decreases the rate of DHC.

The effectiveness of ESO depends on the amount of epoxy groups in the molecule. The higher the amount of epoxy groups the better is the effectiveness. This stabilizing effect of ESO on the thermal degradation of PVC is a result of the facile reaction of HCl with epoxy groups to form chlorohydrins which is thought to reduce the autocatalytic effect of the HCl evolved. Furthermore, the esterification and etherification reactions which occur with unstable allylic chlorine groups in PVC provide an explanation for the very low values of the initial rates of DHC observed when ESO is used in combination with the Ca/Hg stearates. The observed enhanced stabilization effectiveness of the metal soaps of ESO is considered to results from the combined action of the peroxide [34].

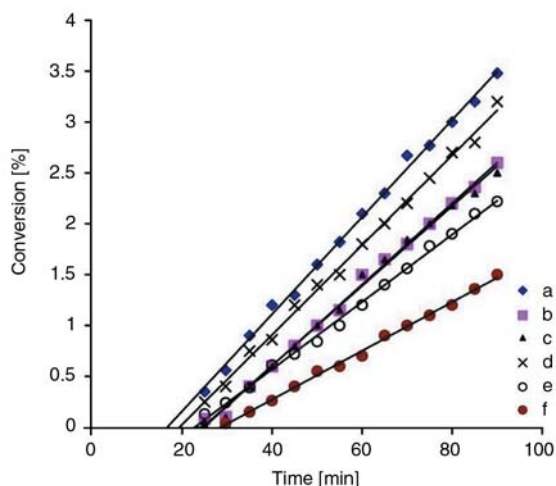


Figure 3. Comparison of stabilizers on the rate of dehydrochlorination of degraded PVC at 180°C: (a) PVC alone, (b) PVC with 0.008 g Hg stabilizer, (c) PVC with 0.008 g Ca stabilizer, (d) PVC with 0.04 g ESO stabilizer (e) PVC with Ca/Hg stabilizers, (f) PVC with Ca/Hg/ ESO stabilizer

Table 1. Dehydrochlorination data at 180°C with 0.5 g PVC containing various stabilizers systems

Stabilizer system	T _s [min]	t _{DH} [min]	R·10 ² [conversion%/min]
none	14	38	4.8
Ca/Hg	23	53	3.3
Cu/Hg/ESO	38	71	2.4

3.4. The UV-visible absorption spectra of PVC samples degraded in N₂ at 180°C

After the degradation of PVC in inert atmosphere, the resulting material was dissolved in freshly distilled 1,2-dichloroethane and UV-visible spectrum was recorded. The combination of Ca/Hg, reduced considerably the initial rates of DHC. The lower value was obtained for the Ca/Hg. For this synergistic mixture of stabilizers, UV-visible characterization of purified PVC samples treated for various times at 180°C and heated 60 min at 180°C for combination of Ca/Hg were realized. As shown in Figures 4 and 5, the combined effect would reduce the amounts of HCl evolved leading to the formation of short polyene sequences absorbing in the ultraviolet region.

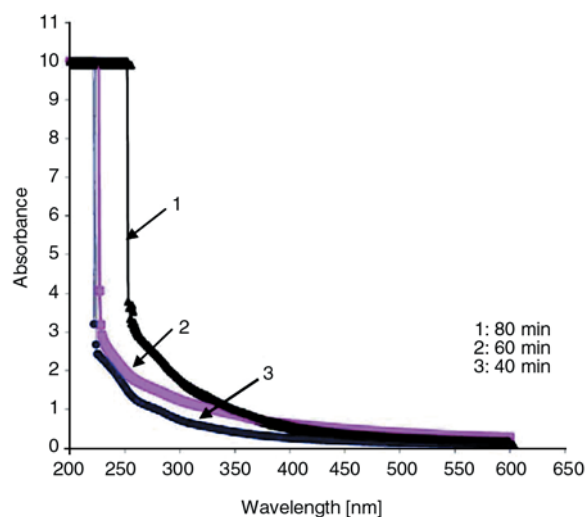


Figure 4. UV-visible spectra of purified PVC stabilized with Ca/Hg (1/1) and treated for various times at 180°C

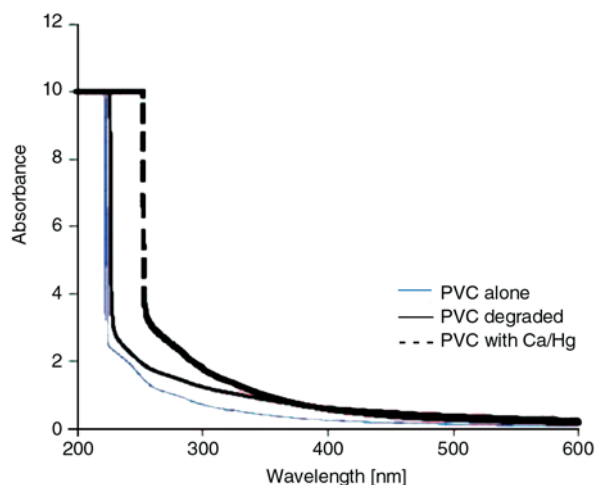


Figure 5. UV-visible spectra of purified PVC stabilized with Ca/Hg heated 60 min at 180°C

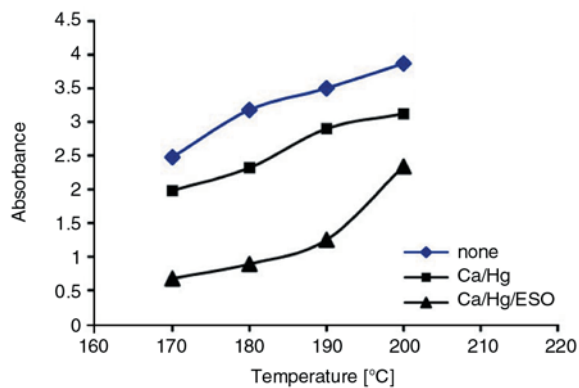


Figure 6. Absorbance-temperature curves for PVC thermally degraded at 90 min in N₂ (samples concentration, 50 mg in 25 ml 1,2-dichloroethane)

The absorption bands were characterized using the maximum wavelength values [35]. The absorption pattern indicates that longer conjugated bond systems are present in PVC samples degraded in the absence of these materials than in the PVC samples degraded in the presence of these materials. The UV-visible absorption spectra of PVC samples degraded in N₂ are generally regarded as not providing accurate or reliable information on the level of unstauration in the polymer, however such spectra could be useful in providing a basis for assessing the relative effectiveness of stabilizers in stabilizing PVC against degradation.

A proof for the high stabilizing efficiency is obtained by measuring the extent of discoloration of degraded PVC. The extent of coloration was determined colorimetrically by measuring the absorbance at $\lambda = 360$ nm for the various samples as a function of the degradation temperatures. The results shown in Figure 6, reveal the lower discoloration of PVC samples was obtained for the Ca/Hg (1/1)-ESO.

3.5. FT-IR spectra of degraded PVC samples

In order to examine the effect of stabilizer on PVC degradation by FT-IR spectroscopy, films of appropriate thickness to give adequate absorption in the required range were prepared. The FT-IR spectra of undegraded PVC and unstabilized degraded PVC and treated for various times are shown in Figure 7. In this study attention was focused on change in the absorption pattern in three main regions: (a) stretching vibration of the COO⁻ group between 1500 and 1600 cm⁻¹; (b) stretching vibration of the

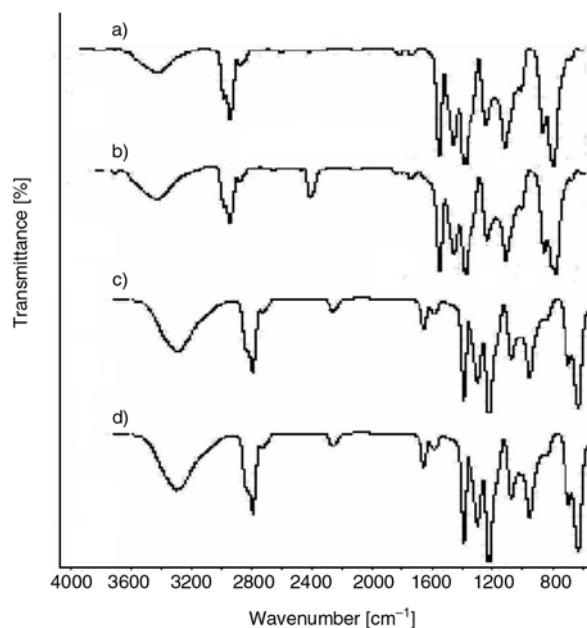


Figure 7. Variations in the FT-IR spectra of PVC samples undegraded and degraded at 170°C in N₂ as a function of degradation time: (a) undegraded PVC, (b) heated 30 min, (c) heated 60 min, (d) heated 90 min

C=C group between 1600 and 1680 cm⁻¹ and (c) the C=O stretching vibration between 1690 and 1750 cm⁻¹.

The FT-IR absorption pattern characteristic of alkenic structure was observed for all the degraded PVC samples at about 1630 cm⁻¹. It indicated that when the temperature increases, absorption by C=C would increase, although the absorption by C=O group has been increased. The assignment of the observed band to the stretching vibration of the C=C bonds in PVC is favored by the fact that a rather weak absorption band at 1710 cm⁻¹ attributed to C=O was observed for all PVC samples. The spectral range 1690–1750 cm⁻¹ is characteristic of absorption bands of esters, carboxylic acids and ketones, and is indicative of the esterification of the polymer chain.

FT-IR spectra of PVC alone and PVC stabilized with Ca/Hg (1/1) in the absence and in presence of ESO are presented in Figure 8.

In comparison with PVC alone, stabilized PVC samples show a band at 1560 cm⁻¹ is due to the metal carboxylate which has not yet been mentioned. The band at 1730 cm⁻¹ is due to oxidation products [36].

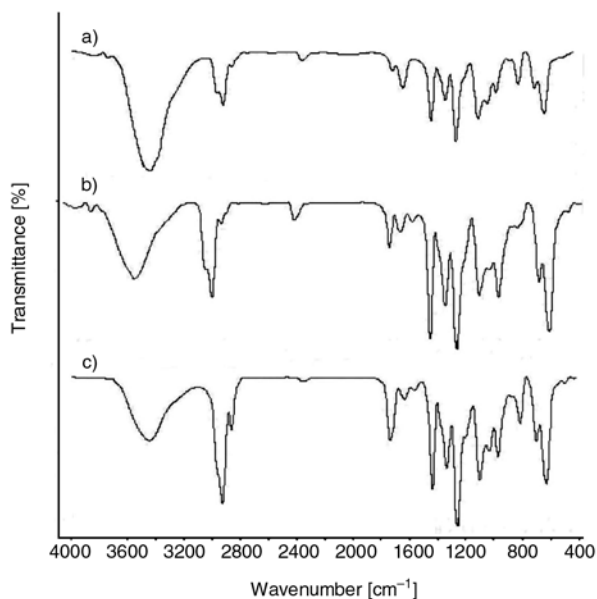
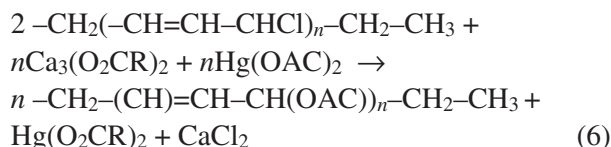
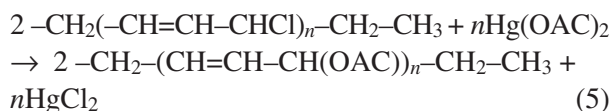
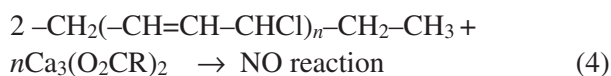


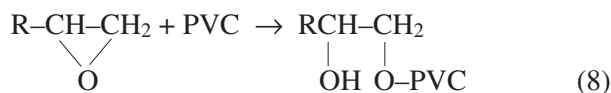
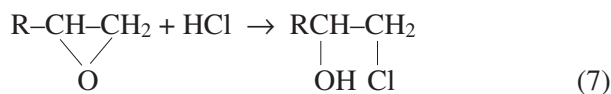
Figure 8. FT-IR spectra of (a) PVC alone, (b) PVC stabilized with Ca/Hg (1/1) and heated 90 min at 190°C, (c) PVC stabilized with Ca/Hg (1/1)-ESO and heated 90 min at 190°C

Figure 8 shows the FT-IR spectra of unstabilized PVC and PVC stabilized with Ca/Hg and PVC stabilized with Ca/Hg/ESO. The FT-IR spectra of PVC containing Ca/Hg/ESO characterized by an absorption band in the 1710–1730 cm⁻¹ range. This band was absent from the spectrum of unstabilized PVC. When combined with the results from the FT-IR studies on the interaction of PVC with Ca/Hg and with Ca/Hg/ESO, these results show that these stabilizers stabilize PVC against thermal degradation by replacing labile chlorine atoms in PVC in addition to acting as HCl scavenger.

From the aforementioned observation and results, it seems reasonable to propose the following mechanism for the stabilization of thermally degraded PVC in the presence of Ca/Hg/ESO: The esterification and reactions which occur with allylic chlorine groups in PVC provide an explanation for the synergism observed in the stabilization of PVC containing a combination of an epoxy compound with metal stabilizer [37]. The mechanism of epoxidation can be displayed by Equations (4), (5) and (6):



Epoxy compounds are well known as typical non-metallic stabilizers for PVC [20]. They are generally regarded as secondary stabilizers used to enhance the effectiveness of metal soaps. They act as acceptors for the liberated hydrogen chloride [9, 21] and retardants for the appearance of discoloration (as in Equations (7) and (8)):



3.6. Extent of thermal degradation: intrinsic viscosity

The variation in the values of relative intrinsic viscosities η/η_0 ; where η_0 is the intrinsic viscosity of undegraded polymer; and η is the intrinsic viscosity of the degraded PVC samples with degradation time are shown in Figure 9. The major types of reactions that may take place during the thermal degradation of PVC in N₂ at moderate temperature such as dehydrochlorination, polymer chain scission, cross-linking, would influence the viscosity of the degraded polymer samples. It has been reported that the intrinsic viscosity of PVC under-

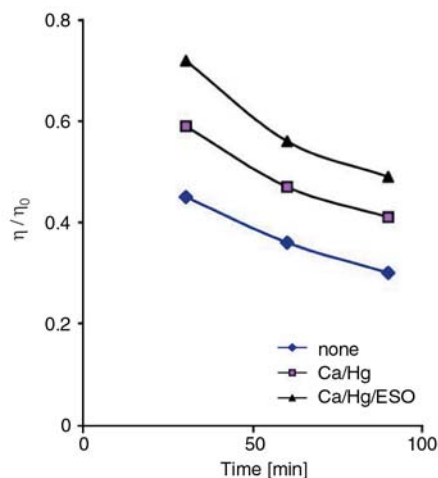


Figure 9. Relative intrinsic viscosity for PVC degraded in N₂ at 180°C after 90 min

going degradation decreases initially to a minimum and then increases with further increase in the number of double bonds in the polymer [38], probably due to reduced flexibility along the main polymer chain. Therefore, in low extents of degradation, it can be assumed that reactions accompanying dehydrochlorination are negligible and that the values of intrinsic viscosity would represent the extent of degradation, the lower the values of intrinsic viscosity, the greater the extent of degradation. The results in Figure 9 show that the values of intrinsic viscosity obtained for PVC samples degraded in the presence of stabilizers are much higher than the values for unstabilized PVC samples. These results are indicative of a stabilizing effect of the materials on the thermal degradation of PVC.

3.7. Kinetics of dehydrochlorination of PVC

3.7.1. Determination of reaction order with respect of stabilizer at constant amount of PVC

The rate of reaction is determined in Equation (9):

$$R = \frac{dx}{dt} \tag{9}$$

where R is the rate of the reaction and x is the concentration of product in the reaction.

The plots of conversion % vs. $[S]$ are linear and slopes of the lines give the rate of the reaction dehydrochlorination. The rate of dehydrochlorination

depends on the concentration of stabilizer and polymer as in Equations (10) and (11):

$$R = k \cdot [PVC]^\alpha [S]^\beta \tag{10}$$

$$R = k' [S]^\beta \tag{11}$$

Experimental values of dehydrochlorination of all additives are given in Tables 2 and 3 and depicted in Figures 10, 11 and 12.

The plot of $\ln R$ vs. $\ln [S]$ is linear and for Hg, Ca and ESO stabilizers is plotted in Figure 13. The slopes of the lines give the order of the reaction with respect to stabilizers.

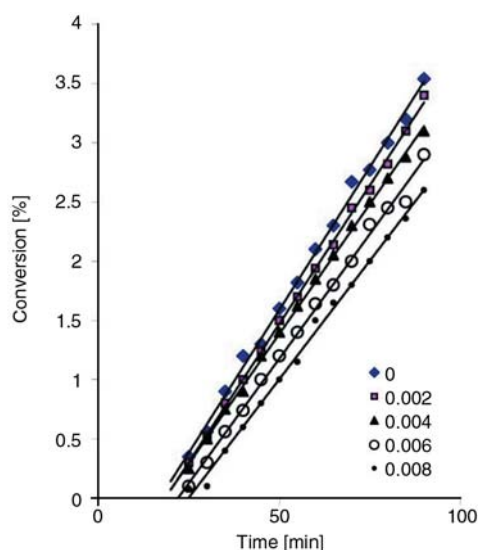


Figure 10. Conversion [%] of PVC at 180°C with 0.5 g of PVC for various amounts of mercury (II) acetate [g]

Table 2. Effect of metal carboxylate amount on the rate of dehydrochlorination of PVC at 180°C with 0.5 g polymer

[S]/g	R·10 ² [conversion%/min]	
	Hg(CH ₃ COO) ₂	Ca ₃ (C ₆ H ₅ O ₇) ₂
0.002	4.7	4.5
0.004	4.4	4.3
0.006	4.1	4.2
0.008	4.0	3.9

Table 3. Effect of ESO amount on the rate of dehydrochlorination of PVC at 180°C with 0.5 g PVC

[ESO]/g	R·10 ² [conversion%/min]
0.01	0.7
0.02	4.6
0.03	4.4
0.04	4.2

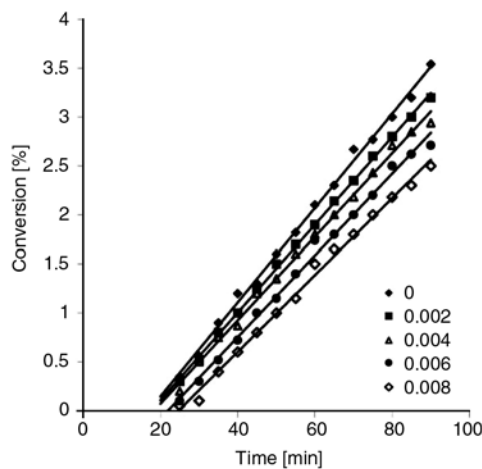


Figure 11. Conversion [%] of PVC at 180°C with 0.5 g of PVC for various amounts of tricalcium dicitrate [g]

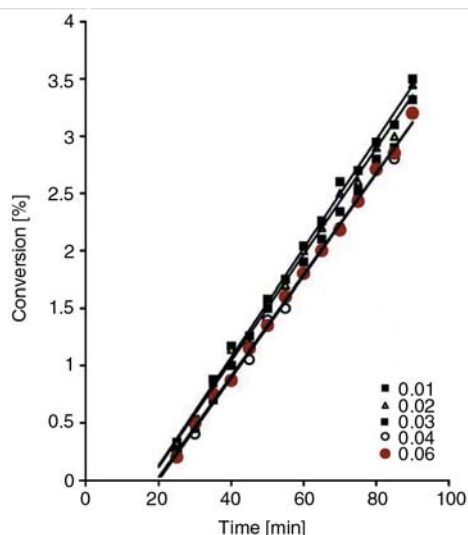


Figure 12. Conversion [%] of PVC at 180°C with 0.5 g of PVC for various amounts of epoxidized sunflower oil [g]

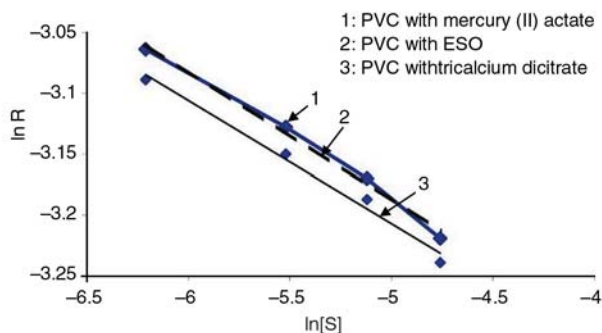


Figure 13. $\ln R$ vs. $\ln[S]$ for mercury (II) acetate, tricalcium dicitrate and ESO stabilizer at 180°C

From the data of Tables 2 and 3 the reaction order with respect to mercury (II) acetate, tricalcium dicitrate and ESO were determined -1.05 , -1.01 and -0.05 respectively. These results show that all stabilizers are the negative orders. Thus the more negative reaction order shows that the more PVC stabilization. It is clear that $\text{Hg}(\text{CH}_3\text{COO})_2$ and $\text{Ca}_3(\text{C}_6\text{H}_5\text{O}_7)_2$ exhibited a greater stabilizing efficiency relative to ESO.

3.7.2. Temperature effect on the rate dehydrochlorination in degradation of PVC

The rates of degradation of PVC at various temperatures are shown in Figure 14. It can be seen that the extent of dehydrochlorination at temperatures between 170–200°C is linear.

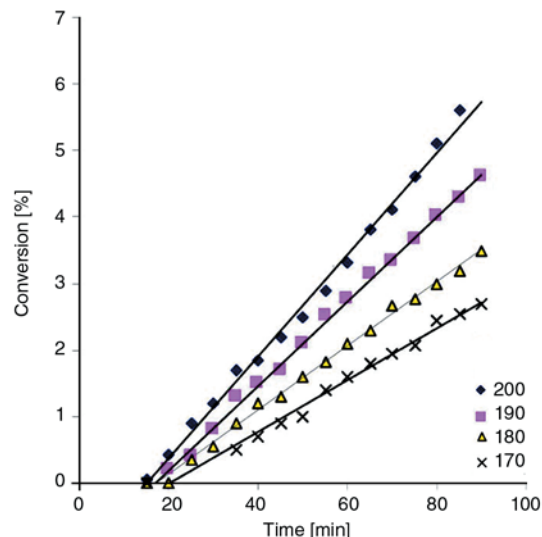


Figure 14. Conversion [%] of PVC with 0.5 g of PVC at different temperatures

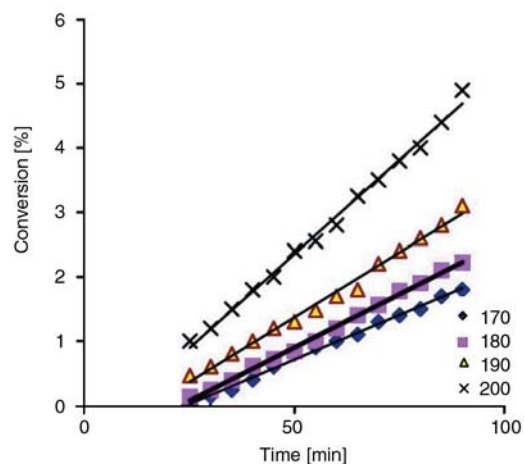


Figure 15. Conversion [%] of PVC with 0.5 g of PVC in the presence of Hg/Ca (2/2) at different temperatures

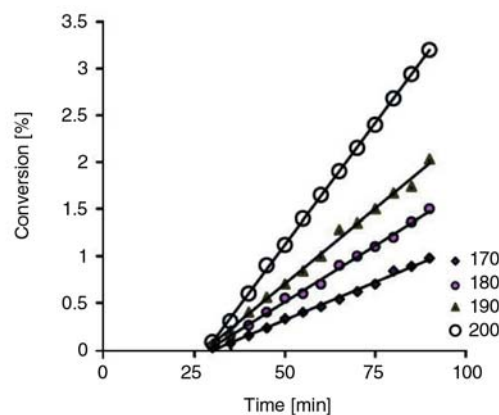


Figure 16. Conversion [%] of PVC with 0.5 g of PVC in the presence of Hg/Ca/ESO (1/1/5) at different temperatures

Similar trends were observed in the degradation of PVC in the presence of mixed stabilizers 0.008 g of each metal carboxylate and 0.04 of ESO (Figures 15 and 16).

3.7.3. Calculation of activation energy

The degraded of PVC was carried out at different temperature in constant conditions (Figures 12, 13, 14). It was observed that the degradation of PVC increases with increasing temperature. The degradation rate was determined and the effect of temperature on the rate of dehydrochlorination are listed in Table 4. Then we may equalize the reaction rate to the degradation rate. Substitution of Arrhenius relation in general rate Equation (12) yields:

$$R = A [PVC]^\alpha [S]^\beta e^{-E_a / RT} \tag{12}$$

where A , E_a and T indicate collision parameter in Arrhenius equation, activation energy and absolute temperature, respectively. Other abbreviations have been defined already. In this manner, temperature is the sole variable. Recent Equation (13) may be rewritten as:

Table 4. Effect of temperature on the rate of dehydrochlorination of PVC with 0.5 g PVC

Compound	R·10 ² [conversion%/min]				E _a [kJ·mol ⁻¹]
	Temperature [°C]				
	170	180	190	200	
PVC	4.1	4.8	6.3	8.0	38.6
Hg/Ca/PVC	2.8	3.3	4.0	5.8	53.3
Hg/Ca/ESO/PVC	1.6	2.4	3.2	5.2	64.7

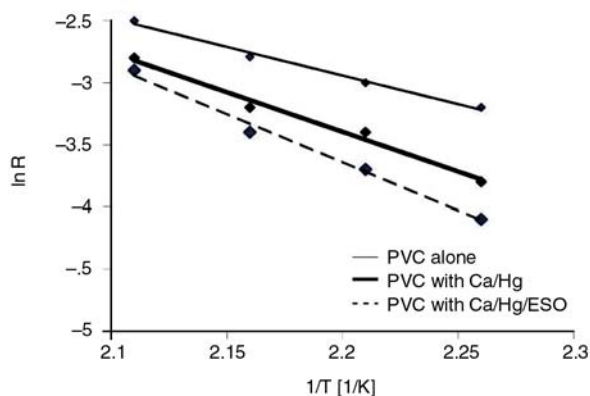


Figure 17. Plot of degradation rate upon the inverse of temperature in the absence and in the presence of mixture of stabilizers

$$\ln R = \ln k' - \frac{E_a}{RT} \tag{13}$$

where $k' = A[PVC]^\alpha[S]^\beta$. It means that if $\ln R$ versus $1/T$ [K^{-1}] values are fitted with a straight line, the activation energies of reaction, slope of plot, may be derived. The results of Table 4 are depicted in Figure 17.

The data of Table 4 show that the variation of the rates and activation energies of dehydrochlorination of PVC. The degradation rates are lower and the activation energies are higher at the presence of stabilizers, compared to the absence of stabilizer. This daringly indicates that the polymer with stabilizer is more stable than the polymer alone. Results observed in our laboratory are consistent with other investigative works [22].

4. Conclusions

In this work, we studied degradation and stability of PVC in the absence and presence of different stabilizers at various temperatures. Epoxidized sunflower oil shows excellent properties as a secondary stabilizer for PVC when used in combination with the synergetic metal soaps (Hg/Ca). The marked effects of ESO on the thermal stabilization of PVC could not be observed by using without the synergetic metal soaps. This ternary system retards the development of dehydrochlorination and reduces the rate of degradation. In the first case, the synergism between ESO and metal soaps results from the reduction of the initial rate of DHC due to the reaction between HCl evolved at the early stages of DHC with ESO and metal soaps which reduces its catalytic effect on the degradation of PVC as well as etherification and esterification reactions of labile chlorine atoms leading to the formation of short polymer sequences which are responsible of the absence of initial coloration. Reduction of initial rate of DHC due to the reaction between HCl evolved at the early stages of dehydrochlorination with ESO and metal soaps which reduces its catalytic effect on the degradation of PVC.

References

- [1] Mohamed N. A., Al-Magribi W. M.: N-(Substituted phenyl) itaconimides as organic stabilizers for rigid poly(vinyl chloride) against thermal degradation. *Polymer Degradation and Stability*, **78**, 149–165 (2002).
- [2] Taghizadeh M. T., Fakhimi F.: Kinetics study of degradation and stabilizing effect of organic thermal stabilizers (EDTA, 1,2 propane diol, benzoic acid and phenol) for rigid poly(vinyl chloride). *Iranian Polymer Journal*, **14**, 685–692 (2005).
- [3] Sivalingam G., Madras G.: Effect of metal oxides/chlorides on the thermal degradation of poly(vinyl chloride), poly(bisphenol a carbonate), and their blends. *Industrial and Engineering Chemistry Research*, **43**, 7716–7722 (2004).
- [4] Starnes W. H., Ge X.: Mechanism of autocatalysis in the thermal dehydrochlorination of poly(vinyl chloride). *Macromolecules*, **37**, 352–359 (2004).
- [5] Arkis E., Balköse D.: Thermal stabilization of poly(vinyl chloride) by organotin compounds. *Polymer Degradation and Stability*, **88**, 46–51 (2005).
- [6] Veronelli M., Mauro M., Bresadola S.: Influence of thermal dehydrochlorination on the photooxidation kinetics of PVC samples. *Polymer Degradation and Stability*, **66**, 349–357 (1999).
- [7] Andricic B., Kovacic T., Klaric I.: Kinetic analysis of the thermo-oxidative degradation of poly(vinyl chloride) in poly(vinyl chloride)/methyl methacrylate-butadiene-styrene blends I Isothermal degradation. *Polymer Degradation and Stability*, **78**, 459–465 (2002).
- [8] Mohamed N. A., Sabaa M. W., Yassin A. A.: Organic thermal stabilizers for rigid poly(vinyl chloride) IV. N-aryl phthalimides. *Polymer Degradation and Stability*, **76**, 355–365 (2002).
- [9] Starnes W. H.: Structural and mechanistic aspects of the thermal degradation of poly(vinyl chloride). *Progress in Polymer Science*, **27**, 2133–2170 (2002).
- [10] Okieimen F. E., Eromonsele O. C.: Stabilizing effect of derivatives of Khaya seed oil on the thermal degradation of poly(vinyl chloride). *European Polymer Journal*, **36**, 525–537 (2000).
- [11] Minagawa M.: New developments in polymer stabilization. *Polymer Degradation and Stability*, **25**, 121–141(1989).
- [12] Kalouskova R., Novotna M., Vymazal Z.: Investigation of thermal stabilization of poly(vinyl chloride) by lead stearate and its combination with synthetic hydro-talcite. *Polymer Degradation and Stability*, **85**, 903–909 (2004).
- [13] Sabaa M. W., Mohamed R. R., Yassin A. A.: Organic thermal stabilizer for rigid poly(vinyl chloride) IX. N-Benzoyl-N-p-substituted phenylthiourea derivatives. *Polymer Degradation and Stability*, **81**, 431–440. (2003).
- [14] Sabaa M. W., Mohamed N. A., Oraby E. H., Yassin A. A.: Organic thermal stabilizer for rigid poly(vinyl chloride) V. Benzimidazolylacetonitrile and some of its derivatives. *Polymer Degradation and Stability*, **76**, 367–380 (2002).
- [15] Stepek J., Daoust H.: Additives for plastics. New York, Springer-Verlag (1983).
- [16] Wypych J.: On the mechanism of action of epoxy stabilizers in poly(vinyl chloride) compositions. *Journal of Applied Polymer Science*, **19**, 3387–3389 (1975).
- [17] Okieimen F. E., Sogbaike C. E.: Stabilising effect of derivatives of jatropha seed oil on the thermal degradation of in poly(vinyl chloride). *European Polymer Journal*, **12**, 1457–1462 (1996).
- [18] Anderson D. F., Mekenize D. A.: Mechanism of the thermal stabilization of poly(vinyl chloride) with metal carboxylates and epoxy plasticize. *Journal of Polymer Science*, **8**, 2905–72922 (1970).
- [19] Lida T., Kawato J., Maruyama K., Goto K.: Stabilization of poly(vinyl chloride).VII. synergisms between epoxy compounds and metal soaps. *Journal of Applied Polymer Science*, **34**, 2355–2365 (1987).
- [20] Benaniba M. T., Belhaneche-Bensemra N., Gelbard G.: Stabilizing effect of epoxidized sunflower oil on the thermal degradation of poly(vinyl chloride). *Polymer Degradation and Stability*, **74**, 501–505 (2001).
- [21] Okieimen F. E.: Studies in the utilization of deoxidized vegetable oils as thermal stabilizer for poly(vinyl chloride). *Industrial Crops and Products*, **15**, 71–75 (2002).
- [22] Benaniba M. T., Belhaneche-Bensemra N., Gelbard G.: Stabilization of PVC by epoxidized sunflower oil in the presence of zinc and calcium stearates. *Polymer Degradation and Stability*, **82**, 245–249 (2003).
- [23] Rüsç M., Klaas G., Warwel S.: Complete and partial epoxidation of plant oils by lipase-catalyzed perhydrolysis. *Industrial Crops and Products*, **9**, 125–132 (1999).
- [24] Mohamed N. A., Sabaa M. W., Khalil Kh. D., Yassin A. A.: Organic thermal stabilizers for rigid poly(vinyl chloride) III. Contonal and cinnamal thiobarbituric acids. *Polymer Degradation and Stability*, **72**, 53–61 (2001).
- [25] Flory P. J.: Principles of polymer chemistry. Cornell University Press, Ithaca, (1953).
- [26] Iván B., Kelen T., Tüdös F.: Degradation and stabilization of poly(vinyl chloride). in 'Degradation and Stabilization of Polymers' (Eds.: Jellinek H. H. G., Kachi H.) Elsevier, New York, 483–714 (1989).
- [27] Tüdös F., Iván B., Kelen T., Kennedy J. P.: Degradation of virgin and modified chlorine containing polymers. in 'Developments in Polymer Degradation, Vol 6' (ed.: Grassie N.), Elsevier, London, 147–189 (1985).
- [28] Iván B., Kennedy J. P., Kelen T., Tüdös F., Nagy T. T., Turcsanyi B.: Degradation of PVCs obtained by controlled chemical dehydrochlorination. *Journal of Polymer Science: Polymer Chemistry Edition*, **21**, 2177–2188 (1983).

- [29] Iván B., Kennedy J. P., Kelen T., Tüdős F.: Cyclopentadienylation of PVC. *Polymer Bulletin*, **1**, 415–420 (1979).
- [30] Iván B., Kennedy J. P., Kelen T., Tüdős F.: Cyclopentadienylation of PVC, Characterization and thermal and thermooxidative degradation studies. *Journal of Polymer Science. Polymer Chemistry Edition*, **19**, 9–25 (1981).
- [31] Iván B., Kennedy J. P., Kelen T., Tüdős F.: Preparation, degradation, cyclopentadienylation, and grafting of PVCs containing relatively high levels of allylic chlorines. *Journal of Macromolecular Science, Part A*, **17**, 1033–1043 (1982).
- [32] Frye A. H., Horst R. W.: The mechanism of poly(vinyl chloride) stabilization by barium cadmium, and zinc carboxylates. I. Infrared studies. *Journal of Polymer Science*, **40**, 419–439 (1959).
- [33] Frye A. H., Horst R. W.: The mechanism of poly(vinyl chloride) stabilization by barium, cadmium, and zinc carboxylates. II. Radioactive studies. *Journal of Polymer Science*, **45**, 1–12 (1960).
- [34] Benaniba M. T., Belhanech-Bensemra N., Gelbard G.: Stabilizing effect of epoxidized sunflower oil on the thermal degradation of poly(vinyl chloride). *Polymer Degradation and Stability*, **74**, 501–505 (2001).
- [35] Abbas K. B., Laurence R. L.: Polyene sequence distribution in thermally degraded poly(vinyl chloride). *Journal of Polymer Science*, **13**, 1889–1899 (1975).
- [36] Beltran M., Marcilla A.: Fourier transform infrared spectroscopy applied to the study of PVC decomposition. *European Polymer Journal*, **7**, 1135–1142 (1997).
- [37] Mohamed N. A., Al-Afaeq E. I.: Aromatic 1,3,4-oxadiazoles as thermal stabilizers for rigid poly(vinyl chloride). *Polymer*, **40**, 617–627 (1999).
- [38] Shindo Y., Morukami M., Nishida T.: On the solution properties of chemically dehydrochlorinated poly(vinyl chloride). *Journal of Polymer Science, Part B: Polymer Letters*, **10**, 555–560 (1972).